Karlsruhe Institute of Technology

Politecnico di Torino

Surface Passivation Strategies of Perovskite Solar Cells

Master's Thesis of

Marco Giolitti

at the Department of Electrical Engineering and Information Technology
Light Technology Institute

Reviewer:	Tenure-Track-Prof. Dr. Ulrich Wilhelm Paetzold
Second reviewer:	Prof. Federico Bella
Advisor:	Dr. Marco Alejandro Ruiz-Preciado

10 May 2022 – 10 November 2022

Karlsruher Institute of Technology
Department of Electrical Engineering and Information Technology
Engesserstraße 13
76131 Karlsruhe

I declare that I have developed and written the enclosed thesis completely by myself, and have not used sources or means without declaration in the text.

Karlsruhe, November 10, 2022

. . . . . .

(Marco Giolitti)

Abstract

Perovskite solar cells (PSCs) have shown a remarkable improvement in efficiency over the past few years, giving high hopes for the future application of this technology in solar photovoltaic electricity production at industrial scale. Nowadays PSCs are inferior to crystalline silicon, especially in terms of efficiency and stability, thus preventing large scale market entry. A common issue of these cells involves the contact surfaces between the perovskite absorber and the charge extraction layers: High densities of superficial defects cause significant non-radiative recombination of charge carriers, thus lowering the achievable open circuit voltage. The focus of this work is the interface between the perovskite and the electron transport layer of p-i-n PSCs, modified by introducing low-dimensional perovskites through novel surface modification techniques. The analysis deals primarily with a triple-cation perovskite composition, optimized for use as top subcell in perovskite/$CuInSe_2$ tandem solar cells. Promising approaches have been compared to select the highest-performing processes before application in tandem devices. Inspired by multiple research papers, the newly developed treatments are based on solutions of phenethylammonium (PEA) salts and perovskite precursors in organic solvents. Upon selection of the most suitable halide ion composing the large cation salt, optimizations of solution concentration and molar ratios are realized. A combination of PEA chloride and methylammonium iodide produces the greatest, although incremental, improvement in power conversion efficiency. To characterize the fabricated devices, photoluminescence quantum yield, x-ray diffraction, and charge extraction analyses are carried out, giving insights into how the investigated solutions modify the perovskite interface.

Contents

Abstract i

Acknowledgements v

1. Introduction 1

2. Fundamentals 3
2.1. Theory of solar cells . . . 3
2.1.1. Photovoltaic parameters . . . 4
2.1.2. Recombination mechanisms . . . 5
2.1.3. Efficiency limit . . . 7
2.1.4. Open circuit voltage losses . . . 8
2.1.5. Charge carrier extraction . . . 9
2.2. Perovskite solar cells . . . 10
2.2.1. Perovskite crystal structure . . . 11
2.2.2. Perovskite electronic properties . . . 12
2.2.3. Low-dimensional perovskites . . . 13

3. Materials and methods 15
3.1. Materials . . . 15
3.1.1. Perovskite precursors . . . 15
3.1.2. Materials for surface treatments . . . 15
3.2. Fabrication techniques . . . 17
3.2.1. Spin coating . . . 17
3.2.2. Thermal evaporation . . . 17
3.3. Solar cell fabrication . . . 17
3.3.1. Substrate preparation and hole transport layer deposition . . . 18
3.3.2. Perovskite layer deposition . . . 18
3.3.3. Electron transport layer and back electrode evaporation . . . 18
3.3.4. Surface treatment techniques . . . 19
3.4. Methods . . . 19
3.4.1. Photovoltaic characterization . . . 19
3.4.2. External quantum efficiency . . . 21
3.4.3. Energy bandgap determination . . . 22
3.4.4. Photoluminescence quantum yield . . . 22
3.4.5. Charge extraction with linearly increasing voltage . . . 23
3.4.6. X-ray diffraction . . . 27

4. Results and discussion **29**
4.1. Photovoltaic performance of surface treated cells 29
4.1.1. Surface treatment with phenethylammonium salts 29
4.1.2. Dual surface treatment with organic salts and perovskite precursors 32
4.1.3. Dual surface treatment with phenethylammonium salts and trimethylphenylammonium tribromide 39
4.1.4. Application of dual strategies to double cation perovskites 41
4.2. Photoluminescence quantum yield results 45
4.3. Charge carrier extraction 47
4.4. X-ray diffraction 50

5. Conclusion **53**

Bibliography **61**

A. Appendix **69**
A.1. Phenethylammonium salt concentrations 69
A.2. Dual treatment concentration dependence 70
A.3. Stability measurements 71
A.4. Charge carrier extraction 73

Acknowledgements

First of all, I would like to thank Dr. Marco A. Ruiz-Preciado for the great supervision and support during the research. I could not have had better coaching in this vast and exciting scientific field.

I would like to express my gratitude also to T.T. Prof. Dr. Ulrich W. Paetzold for the terrific opportunity to work in his research group and for the insightful feedback I received in every meeting. I really appreciated the incitement and the terrific mentoring.

For taking the time to measure the photoluminescence quantum yield of my samples, I am very grateful to Dr. Yang Li and Dr. Paul Fassl.

I would like to extend my thanks to Thomas Feeney and Roja Singh for the help in the lab and for conducting x-ray diffraction and long term stability measurements.

I must say a big thank-you to Ahmed Farag, Ronja Pappenberger, Alexander Diercks, Isabel Allegro, Julie Roger, Julian Petry, and the entire lab group as well, since they provided an incredibly helpful and stimulating work environment. It really meant a lot to me during the months spent working at the Light Technology Institute.

I am also very thankful for all the encouragement I got from my family during my stay here in Karlsruhe: home never felt far away.

Lastly, my gratefulness goes to all the amazing friends I had a chance to meet during my Erasmus program; exploring fascinating and diverse cultures made this experience absolutely unforgettable. I collected a great number of wonderful experiences during this adventure in Germany and I must admit it was all because of them.

1. Introduction

In the past few decades, the planet has witnessed a dramatic uptick in carbon dioxide atmospheric level, which is causing a rapid increase in the average temperature [1]. In turn, rapid heating is causing widespread damage to numerous ecosystems, while making wider portions of land unfit for human civilization [2]. Global warming is the direct result of carbon dioxide and other greenhouse gases, according to the vast majority of the scientific community, as well as the Intergovernmental Panel on Climate Change [3, 4]. Electric power plants are one of the main emitters of CO_2, implying that the world, and especially developed countries, need to find alternative and renewable energy sources to comply with the Paris agreement [5]. Electricity and heat production, employed for either industrial production or building heating, play a leading role in total CO_2 emissions, accounting for 38% of the 36.3 Gt of CO_2 released per annum [6]. Additionally, electricity demand is projected to rise by 2.4 to 3.5% yearly until 2030, putting more pressure on the energy supply system [5, 7]. Novel electricity production methods must be developed in a relatively short time, if the direst consequences of climate change are to be avoided.

Solar energy, and, in particular, the photovoltaic (PV) energy conversion, is growing faster than other renewable technologies and consequently it is among the major candidates to lead the energy transition [7]. PV panels, coupled with proper energy storage solutions, are expected to replace fossil fuels in many civil and industrial applications, contributing to the electrification of our society [8, 9]. Power generation from the PV sector is currently soaring sharply with a 20% year over year growth, though it sits at only 4% of global electricity production [10].

Currently the industry of PV panels is dominated by the crystalline silicon (c-Si) technology, produced with the Czochralski method and accounting for over 90% of market share [11]. This process has enabled remarkable power conversion efficiencies (PCEs), 26.7% at the cell level and 24.4% at the module level [12], but it is reaching the theoretical limit, standing at around 29% [13]. Other technologies have been developing on the side, such as cadmium telluride, gallium arsenide, copper indium gallium selenide (CIGS) and organic solar cells. In the recent past, research has uncovered perovskite solar cells (PSCs), displaying quick progress in PCE [14] and thus driving even more funding in the field. Perovskites are considered a promising research sector in PV electricity production, offering a combination of desirable electronic features and cheap precursor materials [15]. Present research is focusing on the biggest problems holding PSCs from market entry, namely inferior stability and performance not quite reaching the c-Si standard [12, 16].

PSCs have the potential to overtake the c-Si sector firstly in niche applications, owing to their peculiar properties, before entering the global large scale market. Additionally, their production processes, free of high temperature and expensive procedures, are highly suitable for massive manufacturing, a fundamental feature to quickly fight climate change [17]. Economy of scale could drive down the specific cost of production, further promoting

PV electricity in place of fossil fuels. Nonetheless, for industrial deployment the levelized cost of electricity (LCOE) of PSCs must first drop below the c-Si price, possibly with a combination of stability and performance improvements. Advancements in PCE, exceeding the benchmark represented by c-Si, would reduce area-related costs in perovskite PV systems, thus making the economic calculation more favorable by lowering LCOE and payback time [18].

Such efficiency gains can be achieved through pairing of multiple cells in multi-junction solar cells, a technology already in use for III/V semiconductors solar cells. The most elementary case is a system involving two subcells, creating a tandem solar cell (TSC). Pairing of two cells enables a greater exploitation of solar irradiation, attained by optimized selective absorption of each subcell [19]. The focus of this work is a triple-cation PSC in inverted, p-i-n, configuration, based on a hybrid organic-inorganic perovskite.

The analysis centers around the single junction PSC, although this cell has been developed for use in perovskite/$CuInSe_2$ (CIS) tandem devices in two terminal architecture, i.e. series connection between the two subcells. The main problem under investigation is the voltage loss caused by the interfaces between the perovskite absorber and the charge transport layers, due to fast charge carrier recombination. In particular, most of the voltage deficit originates at the contact surface with the electron transport layer, since the opposite junction with [2-(9H-carbazol-9-yl)ethyl]phosphonic acid (2PACz) is nearly loss-free [20, 21, 22]. This issue, often present in PSCs, restricts the power output by decreasing the photogenerated voltage significantly below the theoretical maximum. Inspired by recent literature, multiple approaches to engineer this surface are studied, selecting the best-performing processes before a future application in TSC fabrication. The treatments are based on solutions of large organic cations and perovskite precursors in organic solvents, directly applied on the perovskite surface. Stability of treated devices is also investigated in view of future real-world applications. Such solution-based methods are named passivation strategies or treatments, since the general view is that large cations can occupy superficial defects of bulk perovskite and thus limit recombination speed [23, 24, 25, 26, 27, 28, 29], although direct evidence of defect passivation was not uncovered in this study.

This thesis includes a general summary on solar cell functioning and theory in Chapter 2, with particular focus on perovskite properties and PSCs architecture. Recombination loss mechanisms are described in detail to provide a framework for the conducted experiments. In Chapter 3 characterization methods and employed measurement tools are described, giving a quick explanation of their fundamental principles to interpret the collected data. The selected techniques for PSCs analysis probe efficiency, power output stability, charge extraction efficiency, chemical composition, radiative and non-radiative recombination pathways. Subsequently, results and their interpretations are presented in Chapter 4, discussing the observed changes upon surface modifications. Since a few treatments demonstrated marginal improvements, the discussion moves to possible applications of this study in future works. Conclusions regarding the outcomes and a general outlook of the research direction are contained in Chapter 5.

2. Fundamentals

To provide some background, this chapter collects a general overview of both the perovskite and the wider PV research fields. Essential theoretical concepts on the functioning principle of PV solar cells are introduced, explaining the physical processes at work behind light absorption and the PV effect. Material properties and structural architecture of PSCs are presented, laying the groundwork before description of the conducted analysis.

2.1. Theory of solar cells

The PV effect describes the production of electric current and voltage following light irradiation of a semiconductor. Absorbed photons can create electron-hole pairs, which need to be extracted before recombination to produce a photogenerated current. Electrons require a minimum energy to be excited from the valence to the conduction band of the semiconductor, i.e. jumping to a higher energy orbital. This condition must be always fulfilled to enable successful light absorption, thus limiting the maximum efficiency. To efficiently generate electricity, electrons and holes must be separated and directed to the respective electrodes before recombination events take place. Conventional solar cells based on c-Si rely on a built-in voltage, created by doping the silicon wafer, to extract charge carrier pairs once generated. PSCs do not require doping to separate charge carriers due to long charge carrier diffusion lengths, hence are classified as intrinsic semiconductors.

The distribution of energy states, an elemental material characteristic, is therefore of highest importance for the light absorber selection. The region in the energy diagram between valence and conduction bands, empty of energy levels available to electrons, is named bandgap, thus leading to the concept of bandgap energy, a material property usually expressed in electronvolt (eV). The energy levels that act as edges of the bandgap are indicated as valence band maximum (VBM), the lower boundary, and conduction band minimum (CBM), the upper one. Under sunlight illumination some photons, carrying an energy lower than the bandgap energy, do not contribute to the PV effect, since they are unable to excite an electron. This phenomenon is named transmission and is ubiquitous in solar cells, since the solar spectrum can be closely approximated with a black body emission at around 5778 K. Therefore, a maximum useful wavelength can be calculated through Planck's relation $E_{ph} = h\nu$, above which additional light does not excite charge carrier pairs. Another implication of the bandgap energy is thermalization, the unavoidable dissipation of photon energy that exceeds the bandgap. An excited electron is often brought up to a level higher than the CBM, before moving down the energy diagram until the band edge. This process lowers its potential energy, which is dissipated as thermal vibrations of the crystal lattice, also named phonons. Semiconductors with wider bandgaps encounter minimize thermalization losses, though increasing transmission, and vice versa.

Semiconductors can be further classified into direct and indirect, depending on the momentum needed to excite an electron to the conduction band. In materials with a direct bandgap charge carriers can be excited without momentum contribution, provided by phonons in a crystalline lattice. Conversely, indirect absorbers necessitate momentum for excitation, consequently lowering the absorption of incoming light with sufficient energy.

2.1.1. Photovoltaic parameters

To compare multiple solar cells an array of parameters has been developed, summarizing the most important cell characteristics. The simplest measurement of a PV solar cell is the current-voltage curve, often abbreviated *I-V* curve (*J-V* when referring to current density). Electric potential is applied to the cell in a proper range to simulate different loading conditions. The obtained data carry basic information about the solar cell, quantifying its capability to produce electric power when illuminated. An example of I-V curve is displayed in Fig. 2.1a.

The curve's intersections with the axes provide the operation points at limit conditions, open circuit and short circuit respectively. At open circuit, null current flowing out, the cell produces its maximum voltage (V_{OC}), whereas at short circuit the output contacts are directly connected and the current is highest (I_{SC}). To avoid the area dependence, the short circuit current is usually divided by the active surface, leading to the short circuit current density (J_{SC}). To evaluate how well the cell can exploit these two characteristics to produce power, another important value is defined, the fill factor (FF):

$$FF = \frac{I_{MPP} \cdot V_{MPP}}{I_{SC} \cdot V_{OC}} \tag{2.1}$$

Here the MPP subscript stands for the maximum power point, identified with a star in Fig. 2.1a. Referring to the same picture the FF expresses the ratio between the areas of green and blue squares.

The FF can be easily included in the formula for the power conversion efficiency (PCE), defined as the produced electric power divided by the incident irradiation power (P_i):

$$PCE = \frac{I_{MPP} \cdot V_{MPP}}{P_i} = \frac{FF \cdot I_{SC} \cdot V_{OC}}{P_i} \tag{2.2}$$

The electric behavior of a solar cell can be closely approximated with a simple diode model if operated in normal conditions, i.e. in a moderate voltage range. The power generation is schematized as an ideal current generator, producing a signal equivalent to the photogenerated current (I_{ph}). This current is equal to the short circuit current when considering an ideal solar cell and it is a fairly accurate hypothesis for real solar cells as well, since recombination is minimal at null voltage. A sketch of this model is represented in Fig. 2.1b.

In the electric circuit are also included two electric resistances, which represent various intrinsic loss mechanisms. Namely, the series resistance (R_S) models the bulk resistance of the cell and the electric contacts resistivity, whereas the shunt resistance (R_{SH}) corresponds to the leakage current caused by recombination mechanisms, explained with better detail

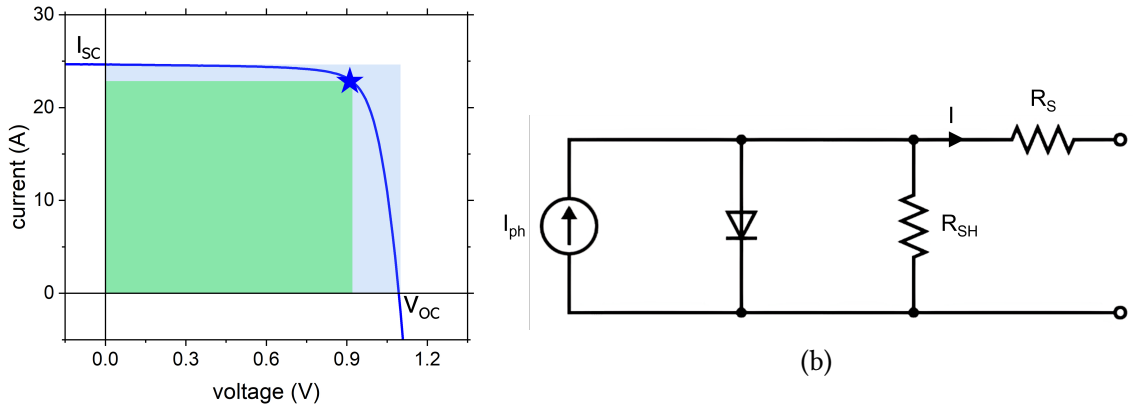

Figure 2.1.: In (a) an example of current-voltage curve is reproduced, with a star marking the maximum power point. (b) Single-diode circuit model of a solar cell, where R_S and R_SH indicate series and shunt resistances, respectively.

in Section 2.1.2. These resistances strongly influence the FF: in particular an ideal cell has negligible R_S while presenting an extremely high R_{SH} to avoid current and voltage losses. Moreover, these two values can be estimated from the I-V curve applying a linear approximation at the axes intersections, using Ohm's law $V = R \cdot I$. Series and shunt resistances indicate the slopes at open circuit and short circuit conditions, respectively.

Based on the described model, it is possible to derive an expression for the current-voltage characteristic starting from Kirchhoff's current law, relating the photogenerated current I_{ph} with current (I) and voltage (V) supplied to the load. The formula states as follows:

$$I = I_{ph} - I_0 \left[\exp\left(\frac{q}{n_{id} k_B T} (V - IR_S) \right) - 1 \right] - \frac{V - IR_S}{R_{SH}} \tag{2.3}$$

Where I_0 is the diode saturation current, also named dark current, q is the elementary charge, n_{id} is the ideality factor, and k_B is the Boltzmann constant. A more detailed description of this model is provided by Ref. [30], whereas a thorough explanation of n_{id} and its interpretation in the field of PSCs are included in Ref. [31].

For an ideal solar cell in short-circuit conditions the equation simplifies to $I = I_{ph}$, supporting the previous claim. On the other hand, applying the same expression to the same ideal cell in open circuit leads to this relation when solving for the voltage:

$$V_{OC} = \frac{k_B T}{q} \ln\left(\frac{I_{ph}}{I_0} + 1 \right) \tag{2.4}$$

Hence, a lower saturation current is beneficial for power conversion, since it is correlated with an increased open circuit voltage.

2.1.2. Recombination mechanisms

The term recombination refers to phenomena that involve electrons moving from the excited state back to the valence band, thus losing potential energy and returning to a

stable condition. Recombination mechanisms are detrimental to PV performance, lowering extracted short circuit current and open circuit voltage, hence constituting extremely undesirable losses in solar cells. They can take place for multiple reasons and can be divided into four categories:

- Radiative recombination is the opposite of light absorption and involves the release of photons with energy corresponding to the bandgap energy. It is unavoidable in semiconductors since it is imposed by Planck's spectral emission law and it is related to variations in charge carrier concentrations compared to thermal equilibrium.
- Shockley-Read-Hall (SRH) recombination is a defect-driven mechanism, caused by vacancies and other crystallographic irregularities that promote electrons dropping to the valence band. Since defects introduce trap states inside the bandgap, electrons can split the bandgap energy step into two portions, enhancing recombination speed. This effect is greater for thicker absorber layers because they involve longer charge carriers traveling paths to reach the electrodes, increasing the possibility of encountering a trap state.
- Auger recombination refers to the annihilation of two opposite charge carriers, transferring the potential energy to a third one, that later dissipates excess energy through phonon emission. It is greatly affected by charge carrier concentrations, hence heavily limiting charge extraction at strong light intensities.
- Surface recombination is a special case of the SRH mechanism, involving interfaces as recombination centers due to the greater presence of defects such as dangling bonds and irregular lattice structures.

These recombination pathways, acting at the same time in the bulk and on the surface of the absorber, determine changes in charge carrier populations, thus influencing their extraction and ultimately the produced power. A key parameter in this study is the charge carrier density (n_c), a concept applicable to both electrons and holes. For any level of n_c greater than zero, a recombination rate (R_c) sets in and influences the equilibrium carrier density in the absorber bulk. This balance is dictated by the continuity equation, reproduced here in differential form, stating that charge must be conserved in a defined control volume:

$$\frac{dn_c}{dt} = \frac{1}{q}\nabla \cdot \mathbf{J} - R_c n_c + G_c n_c \tag{2.5}$$

Where $\mathbf{J}$ is the current density through the borders of the control volume and G_c is the generation rate. The recombination rate can be modeled by splitting the contributions based on the dependence from the charge carrier density, obtaining linear, second, and third order components, as explicated by this expression:

$$R_c = k_1 + k_2 n_c + k_3 n_c^2 \tag{2.6}$$

With k_1,k_2, and k_3 being recombination constants. The recombination mechanisms listed before are accounted for by these parameters, in particular: SRH defect capture of charge carriers is a linear, or monomolecular, effect; radiative recombination is a second order process, comprising an electron and a hole that cancel out; and Auger recombination

is a third order phenomenon, since interactions between three carriers take place. As a side note, surface recombination strongly influence the local value of n_c, introducing spacial gradients in charge carrier density. This phenomenon is especially relevant in the case of defect-rich interfaces or poor energy band alignment between the absorber and the charge transport layers. Furthermore, it is important to remember that surface recombination scales with the minority charge carrier concentration, hence modifying the previous equations.

2.1.3. Efficiency limit

In real solar cells all of the above-mentioned recombination mechanisms are present, limiting the attainable PCE by reducing photogenerated current and voltage. To model the device behavior numerous schemes have been proposed, among which the most well-know is certainly the Shockley-Queisser limit. The two authors published it in 1961 to calculate the maximum achievable PCE for an ideal single junction solar cell [32]. A few key assumptions simplify the mathematical endeavor, including: an ideal absorber, meaning perfect absorption for photon energies above the bandgap; perfect extraction of charge carriers; no optical losses, such as reflection and parasitic absorption; and null non-radiative losses. Consequently, SRH, Auger, and surface recombinations are neglected, thus leaving solely unavoidable radiative losses, imposed by basic thermodynamics of black body radiation. Under these hypotheses each bandgap is associated with the ultimate efficiency, summarized in Fig. 2.2a. It becomes clear that an intermediate bandgap, more precisely 1.34 eV, can minimize losses, delivering optimal energy conversion under the standard AM1.5 spectrum illumination.

Losses can be visualized by plotting the solar spectrum and the spectral use of an ideal solar cell in function of wavelength, shown in Fig. 2.2b for a 1.34 eV bandgap solar cell. The areas below the solar irradiance while above the spectral use curves amount to transparency and thermalization losses. Applying the same calculation to tandem solar cells (TSCs) maximum efficiencies for different bandgap pairs can be calculated, with the optimal PCE of 42.3% achieved with 1.9 and 1.0 eV top and bottom bandgaps, respectively [33]. The available energy of a TSC combining 1.59 and 1.03 eV bandgaps, the final application of the PSC under study, is plotted in Fig. 2.2c.

Shockley and Queisser ignored any non-radiative loss by assuming an ideal black body absorber and emitter, thus applying Planck's law of spectral emission. Such a cell would present the minimum possible current density loss due to radiative emission, expressed by the following equation:

$$J_{0,rad} = q \int_{E_g}^{+\infty} \Phi_{bb}(E) dE \tag{2.7}$$

Where E_g stands for the energy gap and $\Phi_{bb}(E)$ is the black body spectral emission function, approximating the Fermi-Dirac statistics with a Boltzmann distribution:

$$\Phi_{bb}(E) = \frac{2\pi}{h^3 c^2} \frac{E^2}{\exp\left[E/(k_B T)\right] - 1} \tag{2.8}$$

The speed of light in vacuum and Planck constant are indicated with the symbols c and h, respectively.

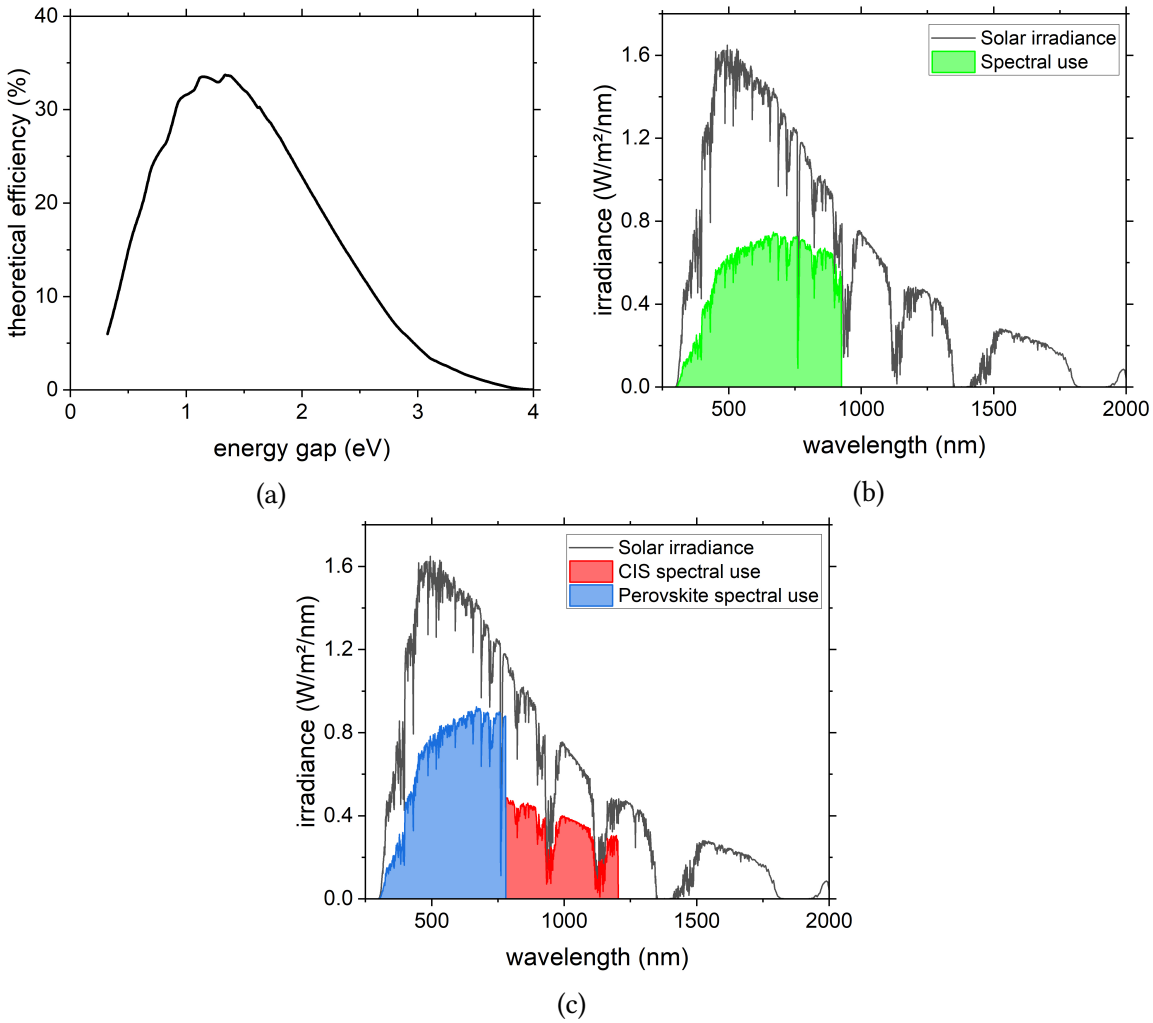

Figure 2.2.: (a) Shockley-Queisser limit efficiency in function of bandgap energy. Spectral uses for single-junction cell with a 1.34 eV bandgap, in (b), and tandem solar cell composed of a 1.03 eV $CuInSe_2$ (CIS) bottom subcell and a 1.59 eV perovskite top subcell, in (c). Spectral uses and Shockley-Queisser limit were calculated with data from the National Renewable Energy Laboratory and through an open-source Python code [34, 35].

2.1.4. Open circuit voltage losses

When analyzing voltage losses in solar cells an important parameter to evaluate is the photoluminescence quantum yield (PLQY), defined as the ratio between radiative emitted photon flux (Φ_{em}) and absorbed flux (Φ_{abs}). According to the recombination model introduced earlier, in open circuit conditions the PLQY can also be expressed as the fraction of radiative (J_{rad}) to total recombination current ($J_{rad} + J_{non-rad}$):

$$PLQY = \frac{\Phi_{em}}{\Phi_{abs}} = \frac{J_{rad}}{J_{rad} + J_{non-rad}} \tag{2.9}$$

The PLQY is an important measurement to quantify the impact of recombination on solar cell performance, since lower recombination rates directly translate into higher PLQY values. Moreover, it can provide insightful information on the open circuit voltage losses taking place inside the solar cell. To see this relation the radiative current density must be replaced with the diode equation, as explained in Refs. [36, 37]:

$$J_{rad} = J_{0,rad}\left[\exp\left(\frac{qV}{k_BT}\right) - 1\right] \approx J_{0,rad}\exp\left(\frac{qV}{k_BT}\right) \tag{2.10}$$

Valid also for PSCs, as reported by Tvingstedt et al. [38]. Upon combining Equations 2.9 and 2.10 for open circuit conditions and solving for the voltage, the final expression is as follows:

$$V_{OC,imp} = \frac{k_BT}{q}\ln\left(\frac{J_{rad} + J_{non-rad}}{J_{0,rad}}\right) + \frac{k_BT}{q}\ln\left(PLQY\right) \tag{2.11}$$

The resulting voltage, indicated as implied open circuit voltage ($V_{OC,imp}$), describes the maximum achievable voltage of the studied device, either complete or unfinished solar cell.

Since by definition $PLQY \leq 1$, the first term on the right side can be considered as the upper limit of the V_{OC}, named radiative open circuit voltage ($V_{OC,rad}$), and it describes the ideal condition, i.e. only radiative recombination takes place. The second term on the right side of the equation is effectively the non-radiative recombination voltage loss, mostly due to the SRH mechanism for PSCs under normal cell operation.

$$V_{OC,imp} = V_{OC,rad} + \frac{k_BT}{q}\ln\left(PLQY\right) \tag{2.12}$$

At this point it is clear why considering only radiative recombination, as done for the Shockley-Queisser limit, is not a good approximation of real solar cells. This reasoning is also supported by experimental results, revealing a substantial discrepancy between the open circuit voltage and the quasi-Fermi level splitting, a quantity related to $V_{OC,rad}$ [39].

From this result it can be concluded that the higher the PLQY the lower the non-radiative defect-assisted recombination rate, resulting in a higher V_{OC} and hence a more efficient solar cell. These mathematical expressions will be used to quantify non-radiative SHR recombination and to evaluate V_{OC} improvements of multiple treatment groups, reported in Section 4.2. Such procedures reduce the surface defect density, thus hindering the SRH recombination pathway and enhancing the V_{OC}.

2.1.5. Charge carrier extraction

As part of the characterization section, extraction efficiency of charge carriers in PSCs is studied, since it is significantly impacted by the developed surface strategies. Successful charge extraction refers to the number of separated electron-hole pairs that can reach the respective electrodes before recombination, contributing to the produced power. Charge separation is carried out thanks to the built-in voltage, induced with doping in c-Si solar cells or created by the heterojunctions at the contact surfaces with charge transport layers in PSCs. Energy barriers at interfaces, high density of defect states, numerous

grain boundaries, and low conductive layers are all possible causes of poorer extraction efficiency, leading to inferior FF and J_{SC}. In a classic silicon solar cell, additional grain boundaries, present in multi-crystalline and amorphous silicon, strongly limit charge carrier diffusion lengths, reducing the charges that can reach the contacts. Moreover, a large defect density induces a smaller shunt resistance and a greater saturation current, hence hampering the cell voltage in all loading conditions, according to Eq. 2.3.

The studied surface modification methods form a low dimensional perovskite (LDP) layer on top of the absorber, decreasing the surface defect density with the aim of limiting SRH recombination speed. However, such LDP layers introduce an additional resistance, due to its limited electric conductivity, and thus hamper charge carrier mobility, as described in Section 4.3.

2.2. Perovskite solar cells

First reported in 2009 in dye-sensitized solar cells as visible light sensitizers [40], perovskites have become increasingly popular in the PV research field, thanks to a combination of desirable material properties and inexpensive production methods. PSCs have now widely surpassed the efficiencies of dye-sensitized solar cells and are expected to become a major player in the future PV market, due to the excellent performances achieved recently [12].

PSCs inherited the structure from dye-sensitized solar cells, but have since then developed distinct architectures owing to the different opto-electronic properties. Perovskite single-junction cells today usually employ: glass as a superstrate, a transparent conductive oxide (TCO) as front, sun-facing, electrode, the perovskite absorber sandwiched between two charge transport layers (CTLs), and a back metallic electrode. The CTLs comprise an electron transport layer (ETL) and a hole transport layer (HTL) to extract the corresponding photogenerated charge carriers from the absorber. The ETL (HTL) is an n-type (p-type) semiconductor promoting electron (hole) extraction by proper energy band alignment. Namely, a narrow difference between the VBM of perovskite and HTL facilitates hole extraction by avoiding charge accumulation or an energy barrier at the interface. In a similar manner, little mismatch between the CBM of perovskite and ETL is beneficial.

PSCs can be classified, based on the deposition order of the layers, in regular or inverted architectures. The regular configuration involves the perovskite deposition on top of the ETL, abbreviated n-i-p referencing to the electric behavior of the various layers (the absorber has nearly no doping, thus is described as intrinsic). The CTLs can be ordered in opposite succession, producing the inverted, or p-i-n, architecture, with the HTL sitting below the absorber. The PSC studied in this thesis, because of numerous reasons concerning the bottom CIS subcell composing the TSC, falls under the p-i-n category. Firstly, high temperature processes for n-i-p PSCs would damage the bottom cell and secondly the $CuInSe_2$ cell polarity imposes the inverted configuration for two terminal TSC architecture. More information on TSCs and their development can be found in numerous review papers [19, 41, 42].

Inverted PSCs make use of inorganic materials as HTL, for example NiO_x, or organic compounds such as: poly[bis(4-phenyl)(2,4,6-trime-thylphenyl)amine] (PTAA), poly(3,4-ethenedioxythiophene):poly(styrenesulfonate) (PEDOT-PSS), (2-3,6-bis[bis(4-methoxy

phenyl)amino]-9H-carbazol-9-ylethyl)phosphonic acid (V1036), and [2-(9H-carbazol-9-yl)ethyl]phosphonic acid (2PACz). ETLs instead are almost exclusively organic, with widespread use of fullerenes and their derivatives as [6,6]-phenyl-C61-butyric acid methyl ester (PCBM) and buckminsterfullerene (C_{60}).

2.2.1. Perovskite crystal structure

PSCs owe their recent success to excellent intrinsic properties of organic-inorganic, or hybrid, perovskites and their lattice structure. The chemical formula is ABX_3, in which A, B, and X consist of a monovalent cation [Cs, methylammonium (MA, CH_3NH_3), or formamidinium (FA, $H_2N{-}CH{=}NH_2$)], a bivalent cation (Pb or Sn), and a halogen (I, Br, or Cl), respectively. For PV applications the cubic phase, also referred to as α-phase, offers the best combination of properties, but other crystal structures are possible. In this configuration the cation B sits at the cell's center surrounded by an octahedron of halogen ions inserted in the middle of the cube's faces, whereas the cation A occupies the corners. A schematics of this lattice structure is presented in Fig. 2.3.

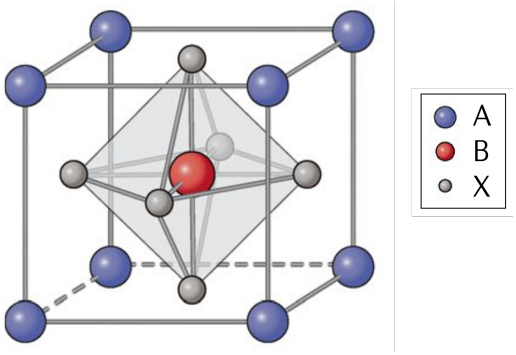

Figure 2.3.: Schematic representation of the unit cell of the cubic perovskite structure, indicated with the formula ABX_3. Adopted from [43].

As a rule of thumb, the ability to form a stable ABX_3 perovskite phase can be empirically predicted through the Goldschmidt's tolerance factor t_G, defined as:

$$t_G = \frac{R_A + R_X}{\sqrt{2}(R_B + R_X)} \tag{2.13}$$

Here R_A, R_B, and R_X represent the atomic radii of the perovskite elemental components [44]. When this factor assumes values close to unity (~0.81−1.1) the perovskite phase is supposedly stable, whereas a non-perovskite phase is formed otherwise. To satisfy this condition the cation A must be considerably larger than the cation B, which explains the frequent use of bulky organic cations such as MA and FA. The presence of Pb, a well-known toxic metal, is currently a weak point since it constitutes a hefty hazard to humans and the environment in case of failure [45].

Mixed organic-inorganic compositions offer great advantages is terms of properties optimization, but at the same time hinder the long-term stability of these devices. Organic compounds can react with other materials present in the solar cell, such as CTLs or the

metal electrode, modifying their physical and chemical characteristics. Moreover, organic molecules deteriorate easily with oxygen, water, or high temperatures, quickly degrading the PV performance. Material properties can be adjusted through many techniques to best fit the studied application, including stoichiometric changes in the precursor solution [46, 47, 48], exposure to organic vapors [49], surface and bulk passivation [24, 50, 51, 52, 53, 54]. A prime example of optimization is the bandgap tuning: the energy gap between valence and conduction band can be smoothly augmented either by adding greater percentages of Br in place of I [55], or by replacing MA with Cs [48].

Another challenge of hybrid perovskites are phase transformations. It has been known for a long time that these structures can undergo multiple crystallographic changes by varying their temperature [56], thus requiring careful composition engineering to widen the stable temperature range [46, 47]. For example, mixing FA and MA cations was shown to halt the formation of the unwanted δ-phase of $FAPbI_3$ perovskite at room temperature [57]. For further information on early development and theoretical background of PSCs see Ref. [58, 59, 60].

2.2.2. Perovskite electronic properties

The cubic crystallographic structure enables especially favorable electronic properties for PV applications. Perovskites display strong absorption in the visible part of the light spectrum, caused by the direct bandgap, constituting a great advantage over c-Si. Consequently, PSCs usually employ a perovskite absorber layer thickness between 400 and 1000 nm, making them more than 100 times thinner than conventional c-Si wafers [61]. They also offer long charge carrier diffusion lengths and low exciton binding energy, two prerequisites for efficient charge extraction [62]. Furthermore, PSCs are weakly affected by crystallographic defects, hence not requiring a single crystal structure to produce high-performing solar cells [63]. Multiple explanations for this behavior have been proposed, but a general consensus has not been achieved yet [64]. Defect tolerance enables numerous deposition options, ranging from solvent-based processes to physical evaporation [17], all based on low-temperature procedures.

Unfortunately, PSCs often present hysteretic behavior during PV testing, producing different results based on the voltage scan direction and hence casting shadows over the long term stability of these devices. This characteristic has been attributed to ion movement inside the perovskite bulk, possibly forming an electric charge barrier at one of the CTL interfaces, although other explanations have not been fully ruled out [63, 65]. This phenomenon can have a significant impact on J-V curves, reducing multiple PV parameters and thus requiring more extensive testing, such as maximum power point tracking, to individuate the best performing solar cells. Hysteresis has been observed on different levels within this work while measuring fabricated PSCs, often complicating result interpretation.

Another common issue associated with the interfaces between the perovskite absorber and the CTLs is the enhanced surface recombination. Such contact areas present high defect density because of the interruption in the material lattice, resulting in trap states that favor non-radiative recombination, i.e. SRH recombination. As demonstrated by Al-Ashouri et al. [22], utilizing 2PACz as HTL in p-i-n PSCs produces a nearly loss-less

interface, fundamentally eliminating the problem on that side. Conversely, the ETL contact area substantially hinders the V_{OC}, as clearly put in evidence by PLQY and time-resolved microwave conductivity measurements [21, 39]. For this reason much research is currently ongoing to engineer the perovskite surface before the ETL deposition, either by interposing an additional layer or by modifying the absorber exterior. This work revolves around the modification of this interface through the formation of low dimensional perovskites on top of the regular absorber, with the intent of reducing the high density of surface defects. For this reason, a brief summary of physical and electronic properties of this new perovskite category will be introduced next.

2.2.3. Low-dimensional perovskites

The indication low-dimensional perovskites (LDPs) identifies perovskite structures with a small number of lattice planes, interrupted by single layers of bulky organic cations. Large organic molecules, such as phenethylammonium (PEA) cannot fit inside the octahedral perovskite cell and must therefore interrupt the perovskite lattice order. The general formula is $R_2A_{n-1}B_nX_{3n+1}$, where R is a bulky organic cation and n indicates the number of perovskite unit cells between two subsequent organic sheets. This structural arrangement, also defined as 2D perovskite given the limited extension in one spatial direction, is analogous to the Ruddlesden-Popper perovskites, discovered more than sixty years ago [66].

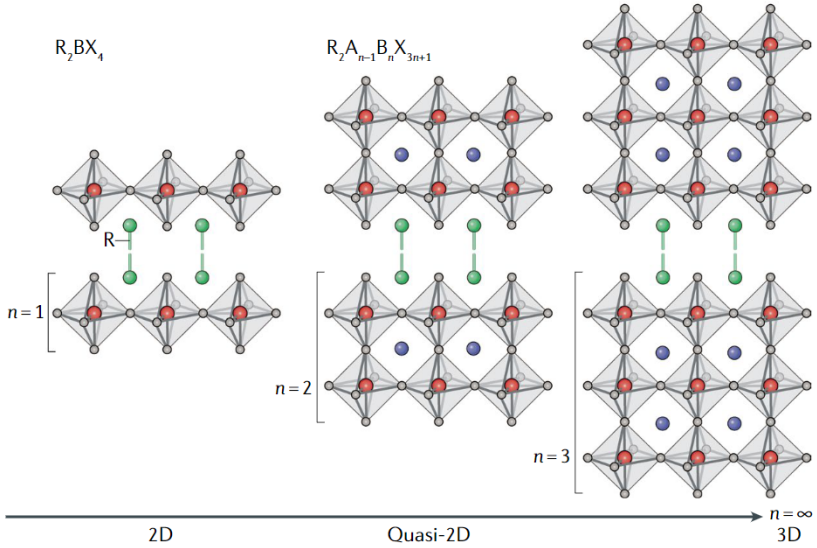

Figure 2.4.: Schematic representation of 2D and 3D perovskites ranging from a perovskite thickness of 1 to infinity. Adopted from [43].

The parameter n, related to the amount of organic spacers, strongly influences the physical properties of the material. For instance, a decrease in perovskite thickness n leads to an increase in exciton binding energy and to a widening bandgap, making LDPs with $n \leq 2$ unsuitable for the absorber role in solar cells [67]. For n tending to infinity the normal, or 3D, perovskite structure is regained, as displayed in Fig. 2.4. Replacing the

organic 2D ligand, either PEA or other organic molecules, can bear dramatically varied chemical features by altering the plane stacking in the 2D lattice, vastly extending the range of applications for LDPs.

The properties of LDPs, similarly to regular 3D perovskites, can be tailored upon compositional engineering, enabling fine tuning of the optoelectronic behavior [68]. Nevertheless, LDPs present numerous different properties when compared with the 3D reference cell. First of all, LDPs properties are not isotropic: for example electric conductivity is strongly reduced by the presence of organic layers, which hinder electron transport in the perpendicular direction. Thus, controlling the alignment of the 2D/3D interface is extremely important for efficient charge extraction, requiring careful optimization [69]. Furthermore, hydrophobic organic cations, for instance fluorinated chemicals, enhance water resistance of LDPs, making them an interesting option to enhance PSC stability [68, 43, 70, 71]. 2D and 3D structures can be integrated to optimize both bulk and surface features, exploiting the advantages of both crystal phases to produce highly stable and efficient multi-dimensional PSCs.

3. Materials and methods

In this chapter information on the adopted PSC structure is summarized, including details about the fabrication process. The employed characterization methods are presented subsequently, with brief explanation of the functioning principle of each instrument. Upon evaluating the PV performance of fabricated PSCs, multiple characterization techniques are employed to investigate the variations introduced by the surface modification treatments, including: photoluminescence quantum yield (PLQY), charge extraction with linearly increasing voltage (CELIV), and x-ray diffraction (XRD).

3.1. Materials

3.1.1. Perovskite precursors

The experiments presented in this thesis, for reasons explained in Chapter 4, involve two different perovskite compositions, namely a triple-cation mixture [$Cs_{0.05}MA_{0.1}FA_{0.85}Pb(I_{0.9}Br_{0.1})_3$], abbreviated CsMAFA, and a double-cation one ($Cs_{0.12}FA_{0.88}PbI_3$), shortened CsFA. Both perovskites possess a 1.59 eV bandgap, suitable for pairing with a ~1.0 eV bandgap CIS cell in TSCs. Employed precursors include PbI_2, $PbBr_2$, CsI, and FAI for the CsMAFA stoichiometry. Conversely, the simpler CsFA comsposition is prepared starting from PbI_2, FAI, and CsCl. Both perovskites contain excess PbI_2, amounting to 3% and 10% for CsMAFA and CsFA, respectively.

The two perovskites are employed in an inverted architecture, thus requiring lower production temperatures in comparison to conventional n-i-p PSCs. Indium-doped tin oxide (ITO) forms the front, sun-facing, contact, enabling hole extraction, whereas a silver cathode transfers electrons out of the device. Devices were fabricated according to a glass/ITO/2PACz/perovskite/fullerene(C_{60})/bathocuproine(BCP)/Ag structure, where 2PACz and C_{60} act as CTLs. The cell stack has been reproduced in Fig. 3.1, together with a schematics of the energy band alignments inside the PSC.

3.1.2. Materials for surface treatments

Surface modification of PSCs has been explored by many research groups in the recent past, producing a convincing body of evidence that these treatments can be very successful in diminishing SRH and surface recombination in PSCs. Noticeable examples of superficial treatments utilize ammonium salts [24, 51, 52, 72, 73, 74], fluorine-containing materials [39, 75, 53], and other organic compounds [23, 76, 77, 78]. Generally, these strategies can be divided into two groups: surface passivation, involving a solution treatment of the perovskite surface, and bulk passivation, based on additives inserted in the perovskite

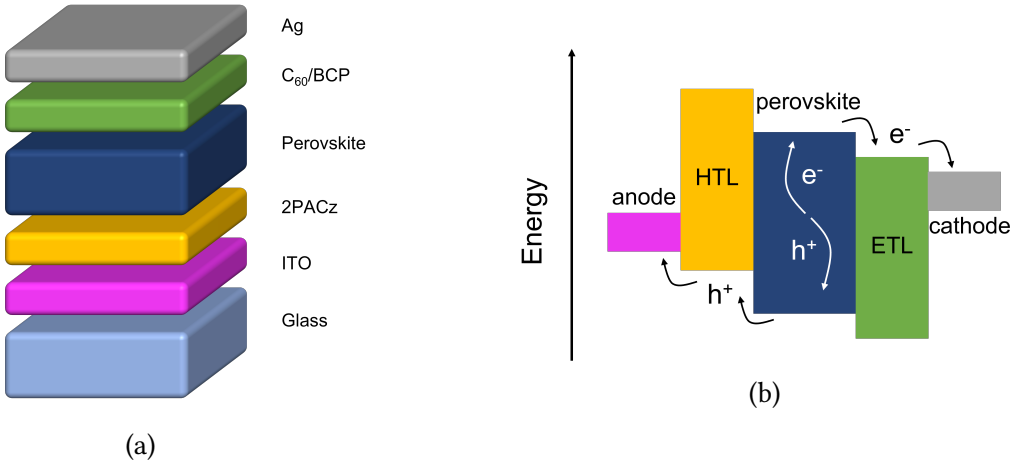

Figure 3.1.: The complete cell stack is represented in (a), including: indium-doped tin oxide (ITO) as front contact, [2-(9H-carbazol-9-yl)ethyl]phosphonic acid (2PACz) and C_{60} as charge transport layers, bathocuproine (BCP) as buffer layer, and silver as back contact. The energy band alignment is schematized in (b) highlighting the successful extraction paths of electrons (e^-) and holes (h^+) after photogeneration. HTL and ETL stand for hole and electron transport layers.

solution. From now on the focus will be on superficial modification of p-i-n PSCs, since bulk additives were not within the scope of this work.

A well-known surface treatment for inverted PSCs is represented by lithium fluoride (LiF): inserting a 1 nm-thick layer before the ETL deposition enhances FF and V_{OC} [79, 20]. Unfortunately, devices with LiF suffer from severe long-term degradation, making it unsuitable for industrial application [75, 79, 80]. Recently Liu et al. have experimented with magnesium fluoride and other fluorides as alternatives, obtaining similar improvements but retaining performance stability [53].

Large cation treatments, on the other hand, actively alter the perovskite surface by partially dissolving the absorber layer and forming a LDP on top of it. Generally, organic salts are diluted in iso-propanol (IPA) and subsequently spin coated on the perovskite absorber, with a brief annealing step completing the process. Phenethylammonium (PEA) based salts are an established, though not unique, surface modification option for PSCs [74]. This approach possesses also the additional potential of enhanced stability, since LDPs are well-known for superior water and thermal resistance [70, 71].

In this work the focus is on compounds formed by PEA with various halide ions, namely PEA chloride (PEACl), PEA iodide (PEAI), and PEA bromide (PEABr). Afterwards, techniques employing monofluorinated PEA salts are studied as part of a replication attempt. These chemicals contain a fluorine atom bound to the benzene ring of PEA, in particular in position 3, and are thus abbreviated to 3F-PEACl, 3F-PEAI, and 3F-PEABr, respectively. More advanced strategies are developed by combining PEA salts and perovskite precursors, namely methylammonium iodide (MAI), formamidinium iodide (FAI), and trimethylphenylammonium tribromide ($TPABr_3$).

3.2. Fabrication techniques

This section encloses all the experimental details related to the fabrication of PSCs analyzed in this study. The fundamental deposition techniques, namely spin coating and thermal evaporation, are introduced. Subsequently the processing is described in a step-by-step manner.

3.2.1. Spin coating

Among the solution-based processes to fabricate PSCs, spin coating is certainly the most common procedure, owing to facile implementation and good crystallization. The precursor solution is dripped on the substrate, which is later spun thanks to a rotating holder, called chuck. Dynamic spin coating, indicating solution deployment during the rotation, was adopted for some surface modification methods. During rotation some extra solvent is dropped on top of the forming film to help crystallization. Solvents ratios in the precursor solution, solvent casting speed and timing, rotating speed, and solution concentration are all factors influencing the obtained film. Most commonly PSCs are later annealed to evaporate all the remaining solvents. For this study the 2PACz and the perovskite absorber were deposited through spin coating.

Record-performing PSCs in numerous categories are produced with this method, although its application is limited to the laboratory scale. Film unevenness and solution waste increase with the substrate size, precluding large scale use of spin coating.

3.2.2. Thermal evaporation

Another widely used technique to produce PSCs is thermal evaporation. With this method the target material is placed on a resistor and then heated through Joule effect, producing a slow evaporation of the compound. The process is carried out inside a vacuum chamber (10^{-6} mbar) to minimize deflection of the vapor stream by air molecules. The evaporation rate can be measured by a piezoelectric sensor placed in the gas flow, which modifies its vibrating frequency due to the mass change when electrically stimulated. The sample holder is also rotating to ensure uniform layer deposition.

Numerous layers in the PSC stack, including the perovskite absorber and the CTLs, can be deposited with this procedure. PSCs fabricated for this thesis include evaporated ETL and metallic back contact.

3.3. Solar cell fabrication

The PSC fabrication process will be described in this section, detailing step-by-step the various proceedings. The sequence of actions to build PSCs, with the exception of glass cutting and cleaning, was always carried out in one day to prevent possible over-night degradation. The fabrication process is unchanged for CsMAFA and CsFA compositions unless otherwise stated.

3.3.1. Substrate preparation and hole transport layer deposition

The production process starts with a glass substrate, cut in 16 mm x 16 mm squares. The glass, purchased from *Luminescence Technology*, already presents a sputtered 120 nm-thick patterned ITO layer (15 Ω/sq) on top, acting as front contact. The pattern scheme, pictured in Fig. 3.2a, presents stripes to enable later access to this contact. The substrates are ultrasonically washed with acetone and IPA in this order for 15 minutes each. After the first bath samples are washed with additional IPA to remove the remaining acetone. To remove the remaining impurities O_2 plasma cleaning for three minutes is performed, immediately followed by the HTL deposition. To deposit the HTL a 1 mM solution of 2PACz in ethanol, previously placed in ultrasonic bath for 15 minutes, is statically spin coated (70 µl) on the sample in a nitrogen-filled glovebox. The substrate is then rotated at 3000 rpm for a 30 s time period, before being annealed at 100°C for 10 minutes to evaporate the residual solvent.

3.3.2. Perovskite layer deposition

The CsMAFA perovskite precursor solution is prepared by mixing PbI_2 with dimethyl-formamide (DMF) and dimethyl-sulfoxide (DMSO) in a 4:1 volumetric ratio for a total of 1 ml, preceding heating at 100°C for a few minutes to enable fast dissolution. Upon cool down to room temperature the solution is added to the other precursors (MABr, $PbBr_2$, and FAI) and shaken until complete dissolution, followed by the addition of the CsI solution in DMSO (1.5 M). The perovskite absorber is subsequently statically spin coated, 70 µl for each substrate, using a two-step program. First 1000 rpm rotation for 10 s, followed by 30 s at 5000 rpm, setting a constant acceleration of 2000 rpm/s. The solvent casting, utilizing 150 µl of ethyl-acetate, was performed with a manual pipette 15 s before the end of the second step.

For the CsFA composition the PbI_2 solution is prepared in the same manner, but later addition includes only FAI and CsCl. The identical spin coating program is used, though solvent casting is executed with an electronic pipette 12 s ahead of the substrate stop.

Samples are later annealed on a hot plate at 100°C for one hour or 150°C for 30 minutes for CsMAFA and CsFA, respectively. After cool down to room temperature the treatment solution is applied, with the details explained in section 3.3.4.

3.3.3. Electron transport layer and back electrode evaporation

The cell stack progresses with the ETL deposition, 20 nm of fullerene (C_{60}) thermally evaporated under high vacuum (10^{-6} mbar) in a physical vapor deposition system from *Angstrom Engineering*. A 5 nm layer of BCP is also deposited to form a better ohmic contact with the metal and limit interfacial recombination [81]. Afterwards the edges of the substrates are swiped with gamma-butyrolactone to remove the perovskite absorber and the CTLs, exposing the front electrode. The 100 nm-thick silver back contact, thermally evaporated in a *BellJar* system with a rate of ~1 Å/s, completes the device.

The multiple fabrication steps are visually summarized in Fig. 3.2, displaying the substrate architecture with its four active areas measuring 10.5 mm^2 each.

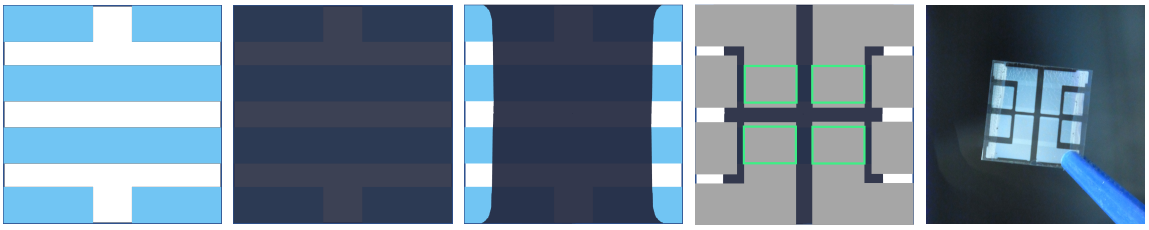

(a) (b) (c) (d) (e)

Figure 3.2.: Solar cell fabrication process steps: starting with glass and indium-doped tin oxide substrate (a); followed by hole transport layer spin coating, perovskite spin coating, and electron transport layer evaporation (b); with subsequent swiping of the edges (c); and finishing with the evaporated metal contact (d). (e) A photo of the complete device.

3.3.4. Surface treatment techniques

Many surface treatment approaches have been developed to reduce SRH recombination at the perovskite/ETL interface of inverted PSCs. Specifically, solutions of large cation salts and perovskite precursors have been analyzed, with the aim of producing LDPs on top of the 3D absorber. Solutions are prepared by dissolving the above mentioned compounds in either pure IPA or a mixture of IPA and DMF, as reported in other articles [25, 26]. The second choice is adopted for dual strategies, involving the combination of a PEA salt and a perovskite forming chemical.

The deposition procedure involves the either static or dynamic spin coating of 150 µl of solution on the formed 3D perovskite, followed by a 4000 rpm rotation for 30 s, accelerating at 4000 rpm/s. In the static procedure the spin coating program is started immediately after the solution dropping, whereas dynamic deployment of the solution is performed 5 s after the rotation start. A dynamic deposition is adopted unless otherwise stated. The annealing is performed at 100°C for 5 minutes, as already tested by multiple groups [24, 25, 26].

3.4. Methods

3.4.1. Photovoltaic characterization

Photovoltaic characteristics are measured according to the commonly accepted standard test conditions, which impose: air mass index (AM) of 1.5, radiation intensity of 1000 W/m^2, and cell temperature of 25°C. More information on the test conditions can be found on the National Renewable Energy Laboratory website [35]. The current-voltage characteristic curve is measured for each active area, extracting the main PV parameters, namely PCE, FF, V_{OC}, and J_{SC}. The voltage is swept in the two directions within the range -0.2/1.2 V, with 10 mV increments, to quantify hysteretic behavior of tested PSCs. Normally the reverse scan results are reproduced in this work.

For the characterization of fabricated PSCs, a class AAA solar simulator Oriel Sol3A by the company *Newport* and a Sinus 70 from *WAVELABS*, based on light emitting diodes,

are utilized. The tested cell is placed inside a holder, with eight gold pins that act as electric contacts. Results from both simulators are corrected for intensity using data from a KG5 c-Si reference cell, placed under illumination right before the first measurement. Additionally, short circuit current densities and PCEs are adjusted with a mismatch factor, accounting for the differences between the AM1.5 and the actual solar simulator spectral intensities, making the results from the two instrument largely comparable. The three mentioned spectral intensities are plotted in function of light wavelength in Fig. 3.3a.

During testing small tolerances in the dimensions of the active area were discovered to cause fluctuations in the short circuit current, thus influencing the PCE. To solve this issue, next PSCs were measured with a 7.84 mm^2 mask, eliminating this problem but simultaneously reducing the V_{OC} by a small amount. Some literature is also present on support of this compromise [82, 83]. However, the presence of the control group is nearly complete, unequivocally underlining real PV performance gains.

Hysteresis was also found to meaningfully influence J-V curve measurements in some cases, affecting especially the FF of fabricated PSCs. For this reason reverse and forward scan data are included for those experiments highlighting significant hysteretic behavior. The mismatch between the two scan directions is quantified with an hysteresis index (HI), defined as the PCE difference divided by the reverse PCE:

$$HI = \frac{PCE_{rev} - PCE_{for}}{PCE_{rev}} \tag{3.1}$$

An example of J-V curves presenting hysteresis has been reproduced in Fig. 3.3b.

Additionally, light soaking effect, i.e. change in PV parameters following extended light illumination, was observed in many treatment groups, distorting collected values. In particular, performance improved upon long light exposure for the CsFA perovskite and degraded for treated CsMAFA solar cells before stabilization. This influence was detected even when PSCs were left in the dark for several minutes following illumination. Since the lamps of the solar simulators shine on the entire substrate, measurements were performed after a 1 minute long soaking period in open circuit conditions, in order to measure each active area in a fair setting. The PCE obtained in this manner turned out to be an imprecise approximation of true efficiency in real working conditions for some treated groups, as explained in Chapter 4.

In order to quickly probe the power output stability of fabricated PSCs, maximum power point tracking (MPPT) tests are performed with the same solar simulators described above, for an period of 300 s. The tracking software employs a perturb-and-observe algorithm, slightly modifying the applied voltage every few seconds and measuring the power to individuate the maximum. After a few treatment groups demonstrated promising stability during this time period, more in-depth analysis was undertaken.

More extensive MPPT tests are undertaken using a *WAVELABS* LS-2 solar simulator (with the spectrum present in Appendix A.3), measuring PCE under 1 sun illumination for 100 hours and inside a 25°C nitrogen atmosphere. These conditions are selected according to the ISOS-L-1 standard, a specific protocol designed specifically for organic PV cells [84]. The aim is to isolate intrinsic degradation mechanisms without influence of external factors such as humidity, oxygen, and elevated temperature. Such mechanisms consist of

light-assisted decomposition reactions of the perovskite layer, a well-known phenomenon of PSCs. Samples were not encapsulated prior to this test.

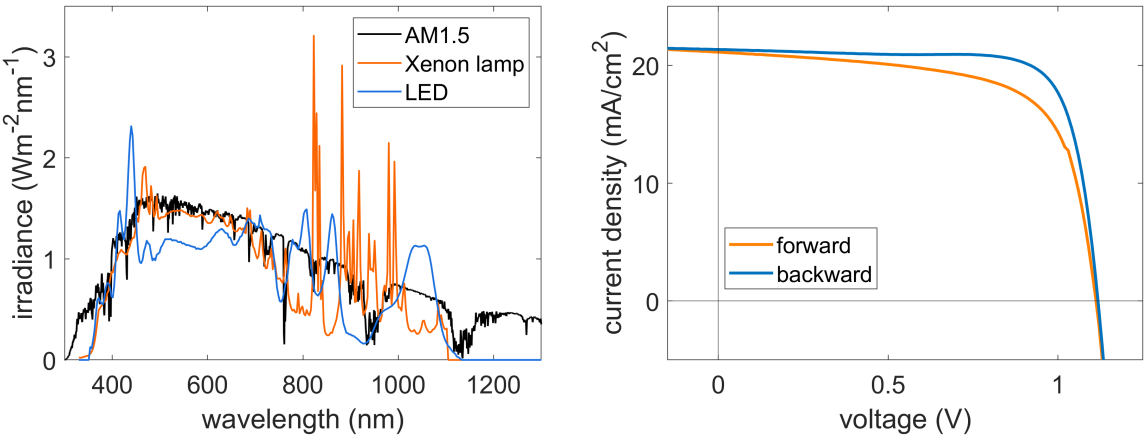

(a) (b)

Figure 3.3.: (a) Spectral irradiance of the Oriel Sol3A (Xenon lamp) and the Sinus 70 (LED) solar simulators compared to the AM1.5 reference signal. (b) Exemplary current-voltage scan of a solar cell displaying significant hysteresis between forward and reverse scan directions.

3.4.2. External quantum efficiency

To gauge how efficiently photons are converted into extracted charge carrier pairs, external quantum efficiency (EQE) of PSCs is evaluated. The EQE is defined as the ratio between the number of collected carriers, namely electrons and holes, and the amount of incident photons. In other terms, when dealing with instant quantities per unit of area, the EQE can be expressed as the current density (J) divided by the incident photon flux per unitary area (Φ_{ph}) times the elementary charge (q):

$$EQE(E) = \frac{J(E)}{q \cdot \Phi_{ph}(E)} \tag{3.2}$$

Both J and Φ_{ph} are functions of either photon energy (E) or wavelength (λ), making the EQE a highly useful tool to investigate how easily absorption and charge collection take place inside the solar cell.

To adhere to the international standards the spectral photon flux must correspond to solar radiation with a 1.5 air mass index. For this thesis a PVE300 photovoltaic QE setup from *Bentham*, placed in a nitrogen filled glovebox, was used, in combination with a c-Si calibration cell. The scanned wavelength range extends from 300 to 852 nm with a 4 nm step size.

Many parameters can be extracted from the EQE data, including the integrated short circuit current density, according to the next equation:

$$J_{SC} = q \int EQE(E)\Phi_{ph}(E)dE \tag{3.3}$$

Treated PSCs exhibited an EQE profile closely resembling the control devices, although shifted downwards by a few percentage points over the entire wavelength range, pointing to less efficient charge carrier extraction. Reference samples demonstrated consistently integrated J_{SC} of around 21.7 mA/cm^2, whereas treated PSCs displayed variable deficits, ranging from 0.1 to almost 2 mA/cm^2.

3.4.3. Energy bandgap determination

EQE measurements are a useful tool, among many others, to calculate the absorber energy bandgap of solar cells. Different estimation methods, as noted in Ref. [85], provide a wide distribution of resulting bandgap energies, leading to significant difficulties in comparison of literature results. Since the obtained bandgap is then adopted in Eq. 2.7 for the calculation of the ideal radiative current density, the choice of the approach significantly impacts the quantification of radiative and non-radiative voltage losses.

The adopted technique, also suggested by Krückemeier et al. [85], is simple and requires only the EQE function. It works by individuating the inflection point of the EQE curve in the absorption edge, i.e. the region of minimum absorbed photon energy. This criterion, compared to other calculation methods, provides a good estimate of the bandgap energy, especially when comparing semiconductors having differently steep absorption edges. The change of concavity in the EQE spectrum is located by extracting the second derivative with a finite difference method. Fig. 3.4a provides a visual representation of the described process.

3.4.4. Photoluminescence quantum yield

Photoluminescence quantum yield (PLQY) analysis, as already mentioned in section 2.1.4, is a powerful method to discern voltage losses due to non-radiative recombination happening in different regions inside the device. Maximum achievable open circuit voltage, named implied open circuit voltage ($V_{OC,imp}$), of different configurations can be computed using Equation 2.11. It must be noted that for these calculations a non-ideal semiconductor is considered, thus substituting the radiative lost current density with this expression:

$$J_{0,rad} = q \int EQE(E)\Phi_{bb}(E)dE \tag{3.4}$$

Applying the theoretical exponential fitting for the EQE in the low energy region, as explained in Ref. [85]. This choice, based on the Urbach tail theory, improves the accuracy of the calculation by reducing the effect of signal noise coming from the measurement. The final result is plotted in Fig. 3.4b together with the normalized photon flux.

Moreover, the sum $J_{rad} + J_{non-rad}$ is replaced with the short circuit current density, calculated by integrating the EQE data as introduced in Section 3.4.2. The final expression for the implied open circuit voltage is then the following:

$$V_{OC,imp} = \frac{k_B T}{q} \ln\left(\frac{J_{SC}}{J_{0,rad}}\right) + \frac{k_B T}{q} \ln\left(PLQY\right) \tag{3.5}$$

The first term on the right side, as noted earlier, defines the radiative limit for the studied semiconductor and is uniquely defined by the EQE spectral response:

$$V_{OC,rad} = \frac{k_B T}{q} \ln\left(\frac{J_{SC}}{J_{0,rad}}\right) \tag{3.6}$$

PLQY characterization is carried out for complete solar cells or incomplete devices, also named half stacks, fabricated following the procedures detailed in Section 3.3. The partial production process is stopped at either the perovskite or the C_{60} deposition step with the only difference being uniform, instead of patterned, ITO for easier measurement. Samples with and without C_{60} have been studied to highlight the voltage loss caused by its interface with the absorber. Since the HTL/perovskite interface has been shown to cause negligible losses [22], the calculated $V_{OC,imp}$ is assumed to be similar for perovskite deposited on 2PACz or inert substrate.

The experiments were carried out according to de Mello et al. [86], by shining a laser with a 15° angle onto the substrate, after placement inside an integrating sphere. The offset angle is to avoid erroneous detection of the reflected light. To probe the impacts of light soaking the PLQY was evaluated immediately following illumination start and also one minute later.

To compare the $V_{OC,imp}$ with measured open circuit voltages, a simple formula was applied to take into account the voltage loss introduced by the shadow mask, when employed in current-voltage measurements. The correction, proposed in Ref. [87], is based on the fact that recombination takes place in all the absorber volume, while free charge carrier generation only inside the illuminated area.

$$\Delta V_{OC} = \frac{n_{id} k_B T}{q} \ln\left(\frac{A}{A_{mask}}\right) \tag{3.7}$$

With A and A_{mask} indicating solar cell active area and mask aperture area, respectively.

For the determination of the ideality factor (n_{id}) an intensity dependence measurement of the PLQY was carried out. Shining light with different intensities, it is possible to fit the calculated $V_{OC,imp}$ with the present logarithmic relation, as indicated in Ref. [31]:

$$V_{OC,imp}(I) \propto \frac{k_B T}{q} \ln\left(\frac{I}{I_0}\right)^{n_{id}} \tag{3.8}$$

With I and I_0 indicating variable and reference illumination intensities.

3.4.5. Charge extraction with linearly increasing voltage

First introduced by Juška et al. in 2000 [88], the charge extraction with linearly increasing voltage (CELIV) method has gained popularity in the PV community. The procedure consists in applying a linear voltage ramp to the solar cell under investigation, measuring the consequent current flow until the new equilibrium sets in after the end of the ramp. The current profile provides information on the charge extraction and recombination happening inside the solar cell, enabling calculation of numerous electric parameters.

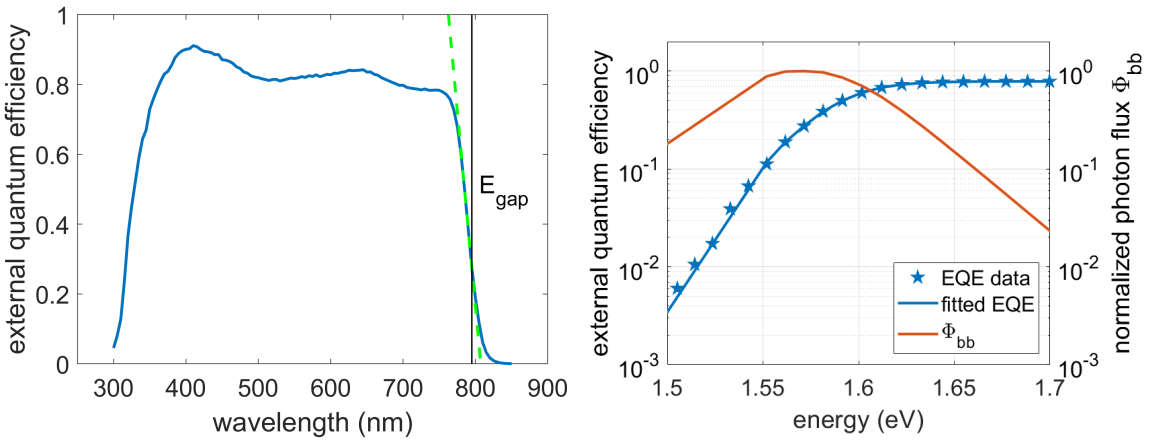

Figure 3.4.: (a) External quantum efficiency as a function of light wavelength, in blue, plotted with the addition of the tangent line at the inflection point, in green. (b) External quantum efficiency data (blue stars, fitted with the exponential Urbach tail trend. The product of ideal black-body photon flux, calculated with Eq. 2.8 and fitted external quantum efficiency is also represented for reference and normalized with the maximum value.

Multiple versions of this technique have been developed, which stem from modifying other conditions such as ramp speed, starting and final voltages, and illumination.

In this work photo-CELIV and dark-CELIV have been selected, since they provide complementary data for the analysis of PSC electronic properties. Photo-CELIV includes sample illumination shortly preceding the applied voltage, in contrast to dark-CELIV which does not. Such illumination provides excess charge pairs, producing a peak in the drawn current, which is not present in dark-CELIV. The ramp starting points are open circuit and short circuit conditions for photo- and dark-CELIV respectively, not to modify initial charge carrier populations. Delay times (t_{delay}) for photo-CELIV are spaced in a logarithmic fashion between 1 and 30 µs, trailing a 100 µs light pulse of intensity equal to 69 mW/cm^2. The voltage time derivative is set at -0.04 V/µs, whereas the final potentials are -0.4 and -0.2 V for illuminated and dark procedures. The voltage, illumination, and current trends have been schematized in Fig. 3.5. The equipment utilized for this measurement is the PAIOS system, manufactured by the company *Fluxim*.

Under dark-CELIV conditions the solar cell response can be modeled with a resistance-capacitance (RC) circuit, with the series resistance (R_S) and the capacitance (C) placed in series. The capacitive behavior is due to charge carrier gradients inside the perovskite absorber, produced by the equilibrium between drift and diffusion mechanisms. Starting from fundamental equations R_S and C can be expressed in the following manner, as explained in Ref. [89]:

$$R_S = \frac{dV/dt}{(dI/dt)_{t=0}} \tag{3.9}$$

$$C = \frac{I(t=0)}{dV/dt} \tag{3.10}$$

Next the modelled circuit current can be computed, either making use of the widely known transient equation or by directly deriving the measured voltage:

$$I_{RC}(t) = I_0 \exp\left(-\frac{t}{R_S C}\right) = -C\frac{dV}{dt} \tag{3.11}$$

With I_0 and $R_S C$ being the initial current and the time constant. In this work the second approach was applied since it was already implemented in the PAIOS proprietary software provided by *Fluxim*. Once this transient current profile is known, photo-CELIV data can be corrected by subtracting this contribution, as displayed in Fig. 3.6b.

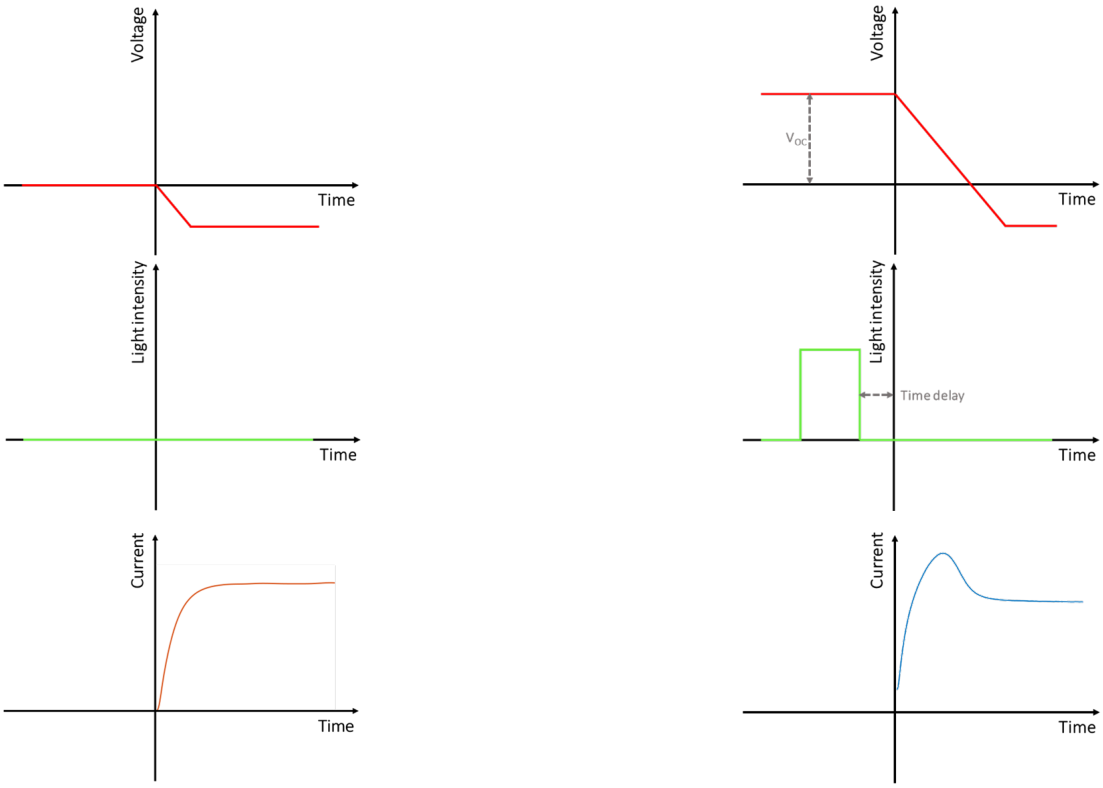

(a) (b)

Figure 3.5.: Charge extraction with linearly increasing voltage (CELIV) characterization. Schematics for applied voltage, illumination, and extracted current for dark- (a) and photo-CELIV (b).

Photo-CELIV measurements, placing the studied cell under illumination, can provide additional information on PSC recombination and charge extraction properties. Increasing the time delay gives charge carrier pairs more time to recombine, producing a lower peak in the extracted current evolution, as displayed in Fig. 3.6a. Furthermore, mobility of majority charge carriers (μ) can be computed with the subsequent equation, introduced by Juška et al. [90]:

$$\mu = \frac{2d^2}{3\frac{dV}{dt}t_{max}^2} \cdot \frac{1}{1 + 0.36\frac{\Delta I}{I(t=0)}} \tag{3.12}$$

Where d and t_{max} indicate absorber thickness and time of current peak, respectively. The second factor has been inserted to fit the results to numerical calculations and it is valid for $\Delta I \leq 10I(t = 0)$. Even though the obtained value should be independent of the delay time, large variation can be observed when plotting μ against t_{delay}, shown in Fig. 3.6c, as noted in Ref. [91]. Higher mobility numbers, reducing the chances for recombination, are a sign of improved charge extraction.

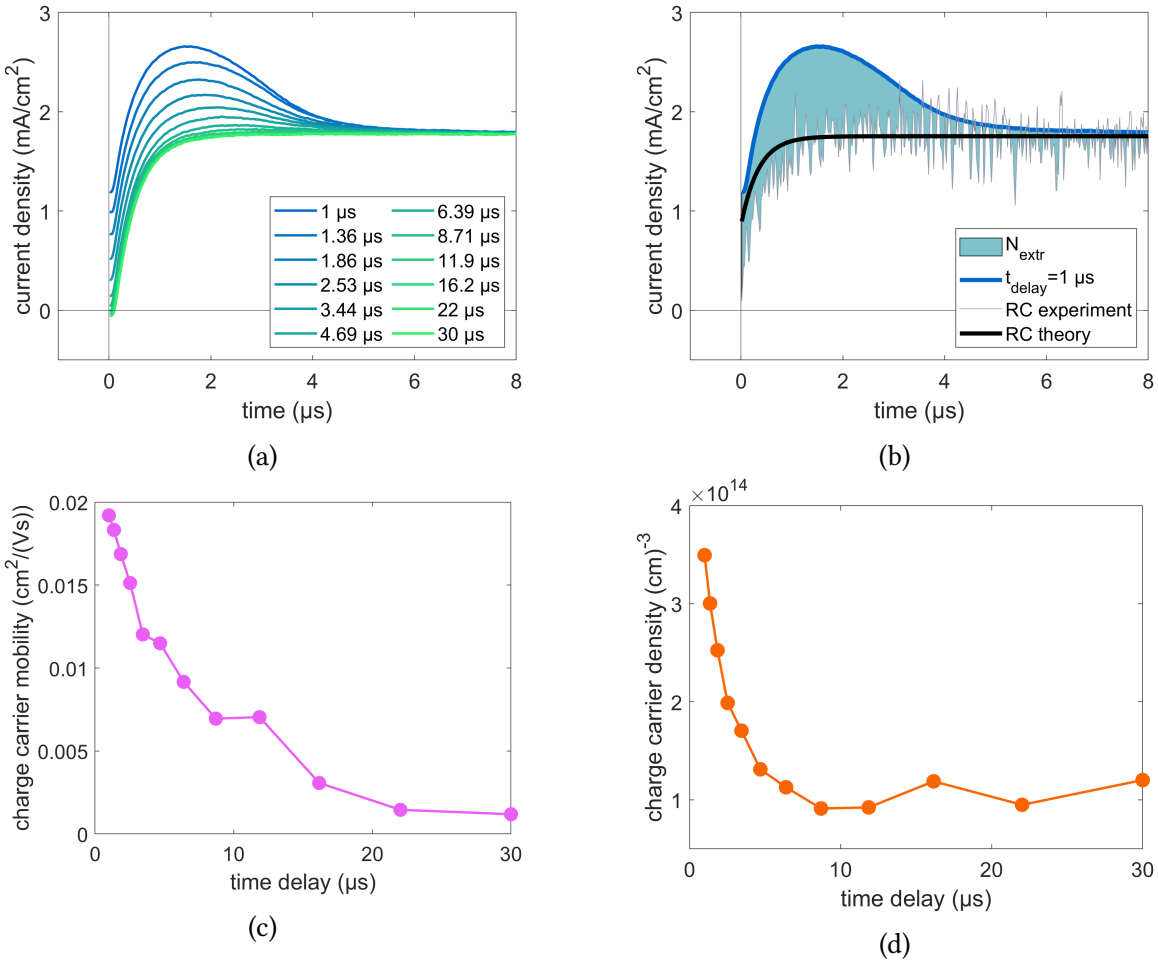

Figure 3.6.: Photo- charge extraction with linearly increasing voltage (CELIV) results. (a) Current density profiles for different time delays between 1 and 30 μs. (b) Current density profiles of: raw data with 1 μs time delay (in blue), experimental resistive-capacitive (RC) response (in gray), and theoretical RC curve (in black). The extracted charge carrier density is determined by the light blue area between the curves. (c) Majority charge carrier mobility as a function of time delay. (d) Extracted charge carrier density as a function of time delay.

Total extracted carrier density (N_{extr}) can also be calculated, integrating the photo-CELIV current evolution after removing the RC effect between ramp start at $t = 0$ and

final equilibrium at $t = t_{end}$, applying this formula:

$$N_{extr} = \frac{1}{qAd} \int_0^{t_{end}} (I - I_{RC}) dt \tag{3.13}$$

With Ad indicating the absorber volume. Tweaking the time delay between illumination and ramp start impacts the current peak, thus highlighting the lost charge carriers due to recombination during this time period. Extracted carriers can be plotted against time delay for multiple PSCs to identify the ones with reduced recombination, as realized in Fig. 3.6d. Comparing normalized results with the same delay time, less pronounced N_{extr} declines for increasing t_{delay} are representative of slower recombination, namely in the form of SRH mechanism for what concerns this work.

It is important to notice that the time constant ($R_S C$) must be small compared to t_{max}, otherwise mobility and extracted carrier results are severely affected by imprecision. Nonetheless, calculated mobility and extracted charge carrier density results can only provide an order of magnitude and must not be interpreted as precise data.

As a small addition, current-voltage curves are measured in dark conditions to provide an evaluation of the dark, also named saturation, current (I_0). According to Eq. 2.4, the lower I_0 the greater the open circuit voltage, leading to enhanced PCE. An example of dark $\mathcal{J}$-V curve is represented in Fig. 3.7, plotted, as most commonly, with a logarithmic vertical axis.

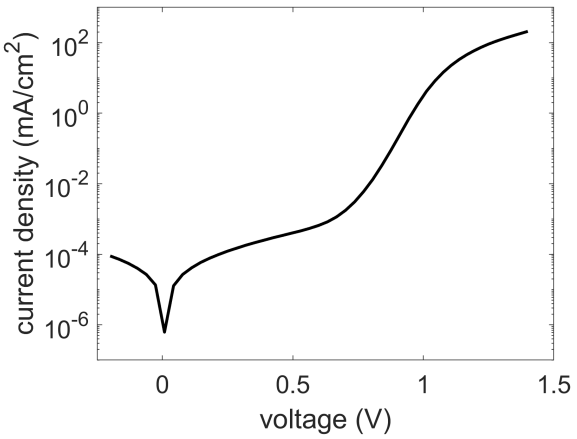

Figure 3.7.: Example of current density curve in function of applied voltage in dark conditions.

3.4.6. X-ray diffraction

As part of additional characterization of the analyzed interface, x-ray diffraction (XRD) measurements are carried out for the most studied treatments. This technique consists in shining x-rays with a variable angle on a crystalline sample and then analyzing the contribution scattered by the atomic electron clouds. Waves scattered by atoms in subsequent crystal planes interfere constructively at specific incident angles, providing information on plane spacing and thus also lattice structure, as schematized in Fig. 3.8a. The interference

phenomenon is regulated by Bragg's law, relating the light wavelength (λ) with the crystal plane distance (d):

$$n\lambda = 2d \sin(\theta) \tag{3.14}$$

Where n is an integer indicating the additional traveled distance, expressed in number of wavelengths.

Many data sheets are present in the literature reporting peak angles of various chemical substances, enabling facile identification of known compounds. Regarding PSCs, a very common peak is present at $\approx 12.9°$ for PbI_2, whereas the perovskite peak is usually detected at $\approx 14°$, depending on the stoichiometry. Superficial LDPs, on the other hand, produce modest peaks at small incident angles due to their limited thickness, and are not easily detectable at normal concentrations. Hence, solution concentrations are increased by a factor of 10 to observe the new crystalline phases in the XRD spectra. Notably, peaks are present also for multiples of the diffraction angles, as a result of x-rays scattered by two non-adjacent crystal planes. An instance of XRD pattern has been reproduced in Fig. 3.8b with indication of the usual diffraction peaks of materials in PSCs, namely: PbI_2 at 12.8°, ITO at 31.8°, multiple perovskite lattice directions at 14.2°, 20.1°, and 24.6°.

Sample preparation was done following the procedures indicated in Section 3.2, halting the process after the spin coating of the treatment solutions. The XRD experiments presented in this thesis were performed using a D2 Phaser setup by *Bruker* with Cu-K_α radiation.

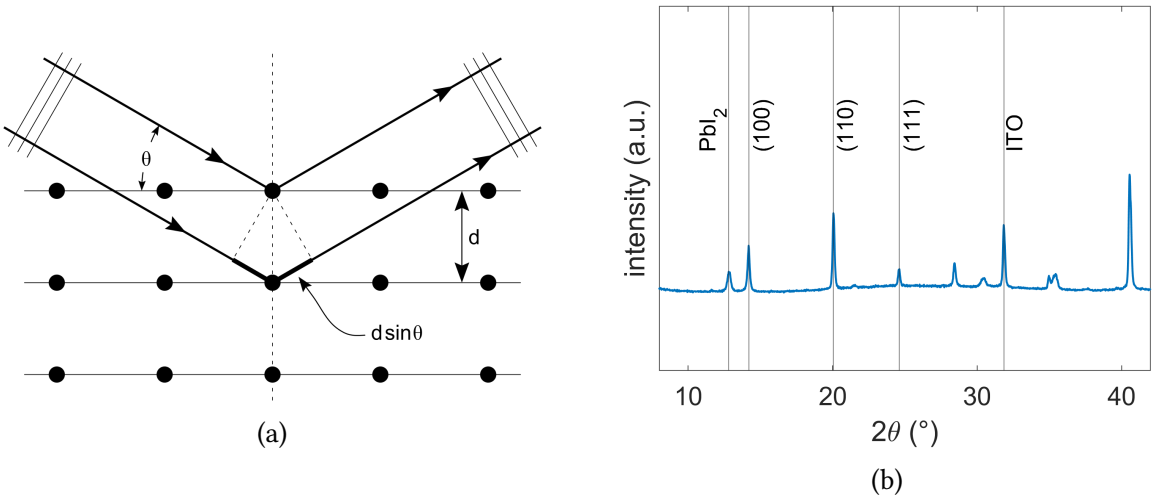

(a) (b)

Figure 3.8.: (a) X-ray diffraction schematics, adopted from [92]. (b) Example of an x-ray diffraction pattern with indication of the most common peaks for metal-halide perovskites.

4. Results and discussion

The objective of this thesis, as already anticipated in previous chapters, is to develop a surface treatment to minimize the voltage losses occurring at the perovskite/C_{60} interface of CsMAFA PSCs. The investigation started from a literature review of the most promising methods developed in the past few years to achieve this goal. All tested procedures are based on organic salts composed by a large cation, phenethylammonium (PEA), and a halogen, namely Cl, Br, or I. More complex, or dual, surface modification options were studied next, introducing also a perovskite precursor, either MAI, FAI, or $TPABr_3$.

Surface strategies were tested with two different perovskite compositions to study the influence of the absorber bulk stoichiometry. Most experiments were carried out with a $Cs_{0.05}MA_{0.1}FA_{0.85}Pb(I_{0.9}Br_{0.1})_3$ mixture, denominated CsMAFA, whereas the rest with a double-cation one ($Cs_{0.12}FA_{0.88}PbI_3$), shortened CsFA, as described in Section 3.1.1. All treatments turned out to be slightly more effective with the double-cation perovskite, although the underlying reason could not be isolated. Furthermore, an additional solution based on $TPABr_3$ was studied more in-depth in terms of power output stability.

Afterwards, in Sections 4.2 and 4.3, further characterization of the fabricated devices is presented, attempting to explain the resulting voltage increases. Photoluminescence quantum yield (PLQY), charge extraction, and carrier mobility measurements have been performed with this aim. X-ray diffraction (XRD) spectra are present to provide supplementary information on the additional phases in treated surfaces.

4.1. Photovoltaic performance of surface treated cells

Numerous scientific studies report surface passivation of inverted PSCs upon use of bulky organic cations, forming a superficial 2D perovskite layer on top of the 3D absorber [24, 25, 51, 52, 73]. Common observed changes include enhanced V_{OC}, PCE, and stability of the treated devices, mostly ascribed to the newly-formed LDP layer on top of the 3D bulk. The article by Gharibzadeh et al. [24], which analyzed the CsFA composition introduced earlier, was selected as research starting point before switching to the CsMAFA perovskite.

4.1.1. Surface treatment with phenethylammonium salts

The study of surface engineering methods was initiated with replication of a published result, providing a solid starting point for the subsequent analysis. The selected treatment, reported in Ref. [24], is part of a quickly growing research field and constitutes a model approach that has been proven to work in multiple articles. The process is based on a 10 mM PEACl solution in IPA, applied according to Section 3.3.4. The statistical data, plotted in Fig. 4.1, have been obtained after one minute of light soaking time to allow

performance stabilization of treated and reference devices, a behavior explained in better detail in Sections 4.1.2 and 4.1.4. The modified PSCs exhibited the expected changes, namely an increase in V_{OC} of roughly 40 mV compared to the control group, demonstrating the effectiveness of the approach. Meanwhile FF and J_{SC} were not affected, resulting in a PCE gain of almost $1\%_{abs}$.

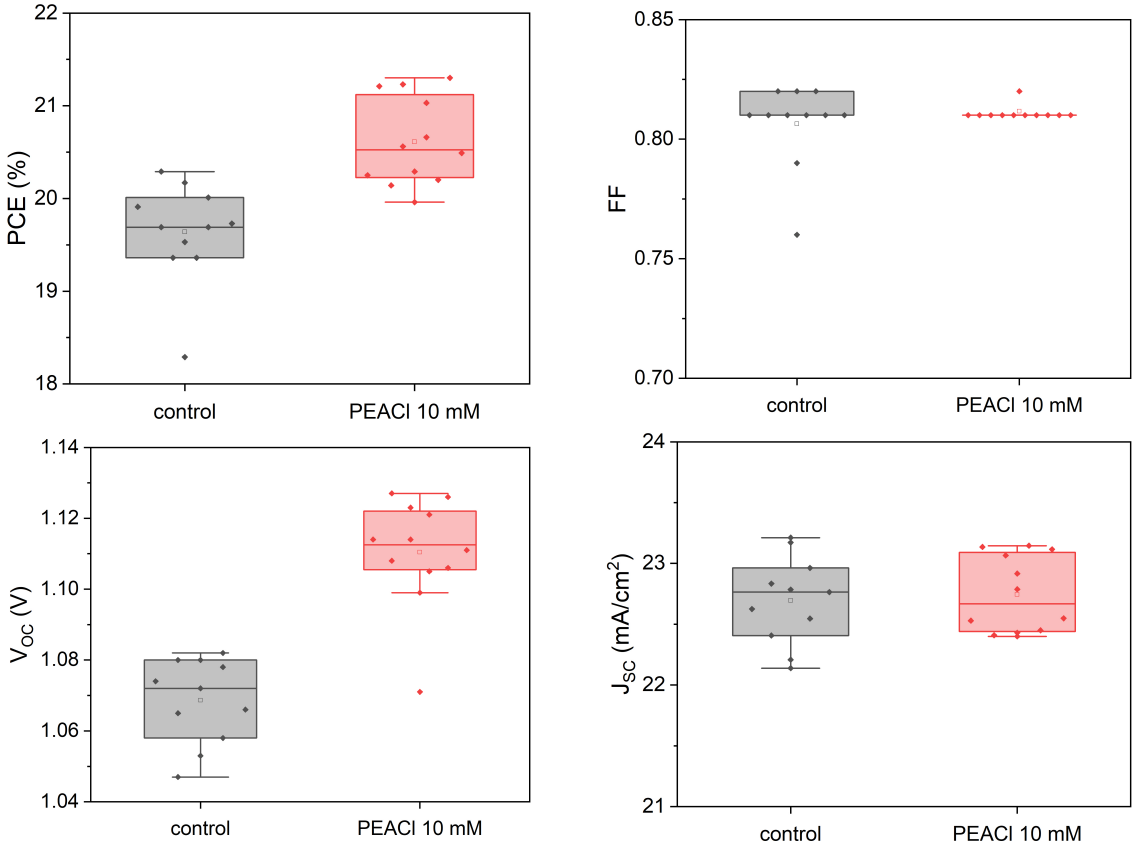

Figure 4.1.: Photovoltaic parameters of CsFA PSCs treated with a 10 mM PEACl solution against control. The abbreviations stand for power conversion efficiency (PCE), fill factor (FF), open-circuit voltage (V_{OC}), and short-circuit current density (J_{SC}).

This positive outcome led to the application of similar treatments to the CsMAFA perovskite, seeking an analogous PCE boost. The analysis included a scan of similar large cation salts, namely PEABr and PEAI. These procedures were named simple strategies, to distinguish them from dual techniques described in later sections. Solutions with 5 mM and 10 mM concentrations in IPA were prepared for the three compounds, since previous data, reported in Appendix A.1, demonstrated excessive PCE declines with 15 mM, mainly caused by reduced J_{SC}. The results, displayed in Fig. 4.2, highlighted how these treatments reduce the J_{SC} while boosting the V_{OC}, in contrast to the outcome of the CsFA perovskite. Higher concentrations, producing greater V_{OC} increases and similar current drops, were deemed superior, with the exception of PEAI. In the latter case the 5 mM group displayed equal V_{OC} gain, roughly 40 mV, but higher J_{SC}, making it preferable for later optimization.

In contrast to CsFA, the CsMAFA perovskite showed a slight degradation in *FF* for all treatments, that combined with the lower current resulted in inferior PCE in comparison to the reference group.

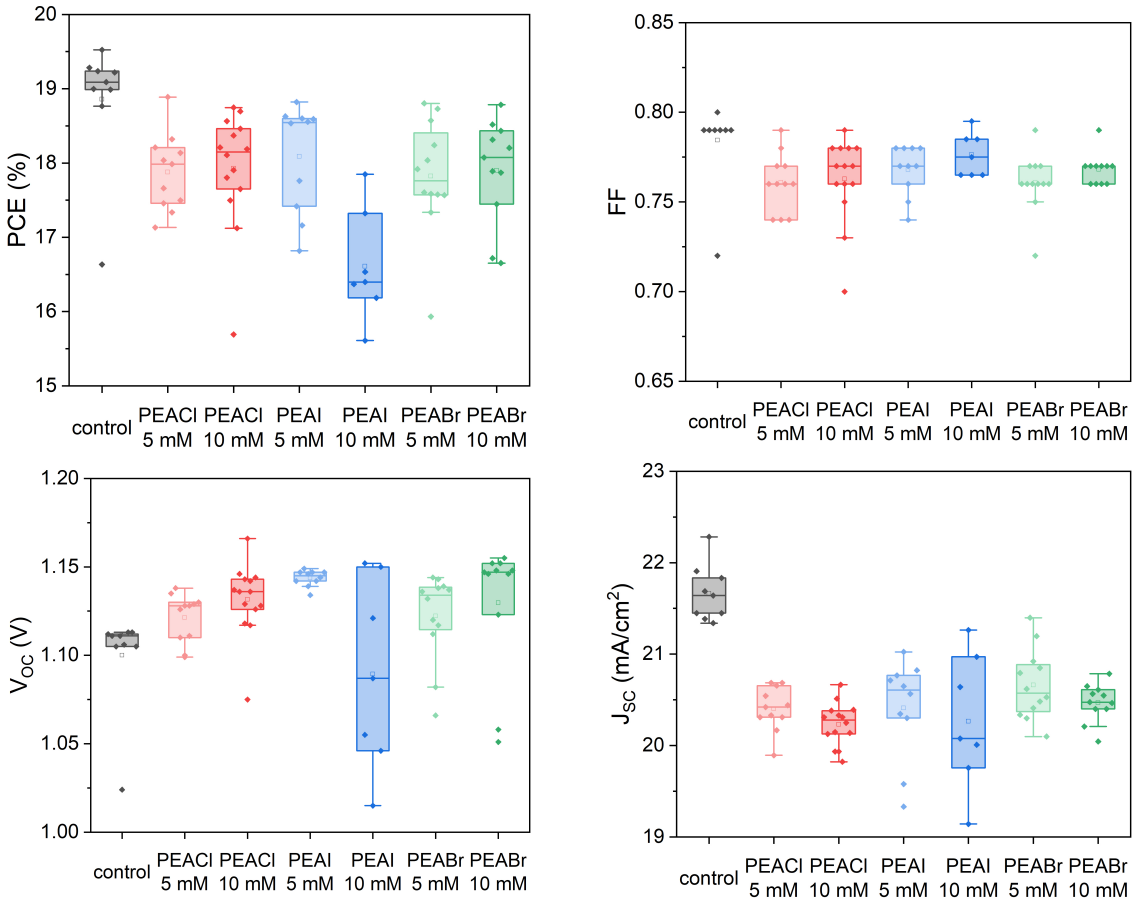

Figure 4.2.: Photovoltaic parameters of PSCs treated with different phenethylammonium salt concentrations. The abbreviations stand for power conversion efficiency (PCE), fill factor (FF), open-circuit voltage (V_{OC}), and short-circuit current density (J_{SC}).

The short circuit currents evaluated in this case were slightly lower than in subsequent data for some treatment groups, however, no single cause of the reduction could be isolated. To support the previous result, J_{SC} measurements obtained from the EQE integration were reported in Fig. 4.3 and displayed an identical trend, confirming the reduction upon surface engineering. Integrated J_{SC} is considered more reliable, firstly because it is independent of the active area extension, and secondly it does not suffer from spectral mismatch. In summary, surface modifications marginally impaired short circuit current at all wavelengths, with greater impacts for more concentrated solutions, pointing to inferior charge extraction, analyzed in more detail in Section 4.3.

To test whether PEACl treatments work differently with CsMAFA compared to CsFA bulk composition, other parameters were modified, selecting the 10 mM PEACl treatment as a test group. Initially the static spin coating of the solution was tested, following what

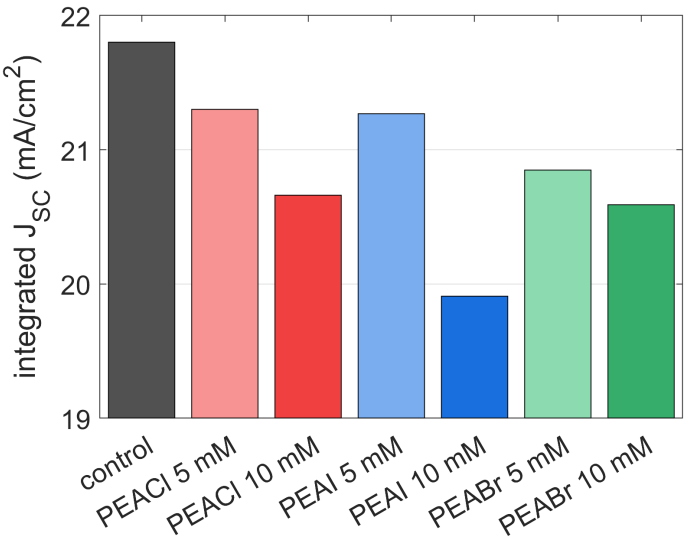

Figure 4.3.: Integrated short circuit current density (J_{SC}) of CsMAFA PSCs treated with PEA salts containing different halides in concentrations of 5 and 10 mM.

reported in other literature articles [25]. Minor differences in PV parameters were recorded between the two groups, leading to the conservation of the dynamic approach for later investigations. Afterwards, the 5 minutes annealing time was compared to not-annealed samples, demonstrating that the procedure was beneficial since it caused an increase in V_{OC} of 10 to 20 mV. Data from these experiments are plotted in Fig. 4.4. This result is in contrast with other literature dealing with n-i-p PSCs, which found that the annealing step was not beneficial to PV performance [50]. Other annealing parameters, such as temperature and timing, were not studied more in detail.

The above-mentioned results, supporting previous choices of strategy parameters, led to the hypothesis that the dissimilar behavior of the surface modification methods was caused by the different perovskite composition, since MA and Br are absent from the CsFA mixture. The assumption prompted further literature review, to find out whether other research groups had already observed similar effects. A recent study had reported substantial PCE increases, employing a new set of materials with a perovskite bulk composition that closely resembled the triple-cation CsMAFA combination [25]. As presented in the next subsection, the same treatment concepts were applied to the CsMAFA perovskite to probe the validity of such procedures.

4.1.2. Dual surface treatment with organic salts and perovskite precursors

In 2019 a novel passivation strategy has been proposed by Zhou et al. [26], involving the addition of MAI to the large cation solution. Additionally, a small amount of DMF was added to partially dissolve the underlying 3D perovskite, with the intent of obtaining a more uniform and thicker LDP layer.

In a later article, Chen et al. continued the investigation by applying the MAI addition concept, named quasi-2D treatment, to regular as well as fluorinated PEACl salts, following DMF content optimization [25]. The latter compounds include a fluorine atom attached to

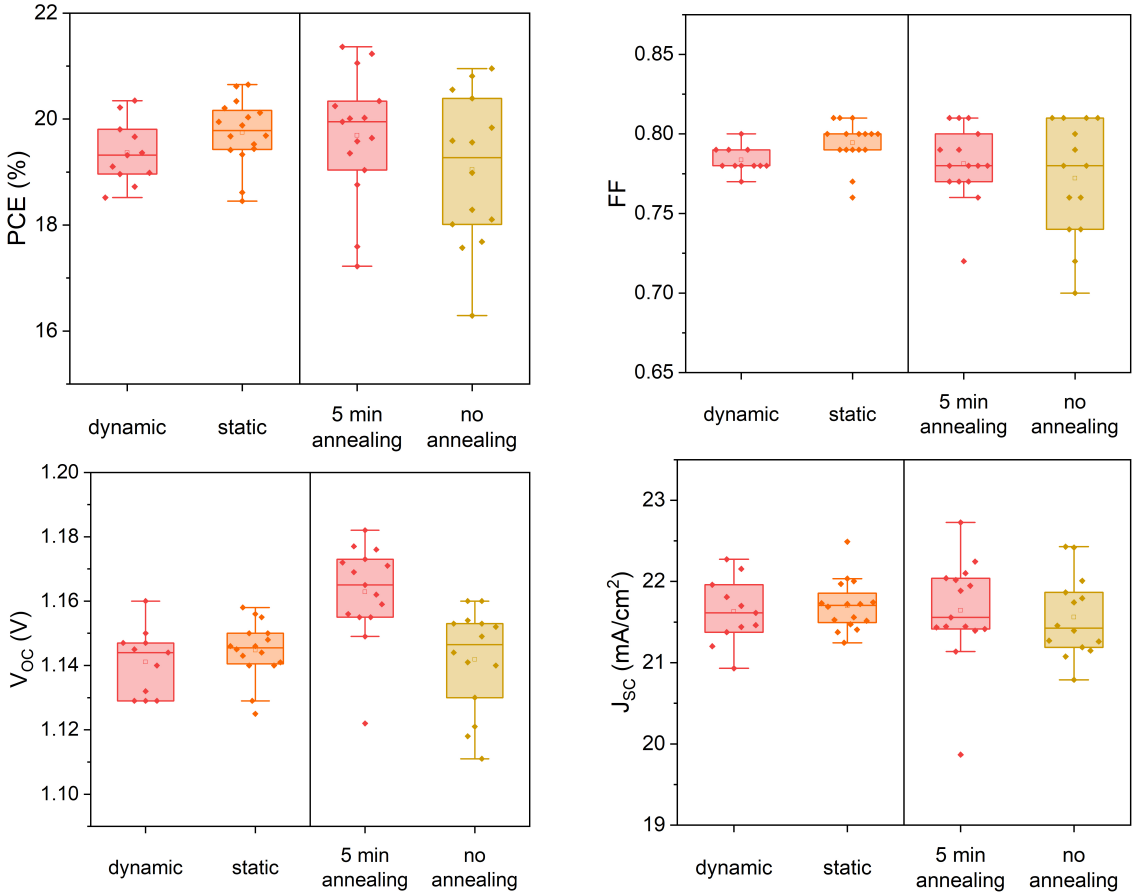

Figure 4.4.: Photovoltaic parameters of CsMAFA PSCs treated with PEACl solutions modifying spin coating deposition method, static vs dynamic, and annealing time, 5 vs 0 minutes. The abbreviations stand for power conversion efficiency (PCE), fill factor (FF), open-circuit voltage (V_{OC}), and short-circuit current density (J_{SC}).

the benzene ring of PEA, causing small but decisive changes in chemical bonds arrangement. First introduced in 2D PSCs, these materials showed starkly different crystal structure and PV performance due to peculiar packing of the bulky organic cations in $n = 1$ 2D perovskites [93]. These features are fully determined by the position of the fluorine atom in the benzene ring, emphasizing the fundamental importance of atomic bonds and formation energies in perovskite crystallization. In the results reported by Chen et al. the fluorinated PEACl salts, in particular 3F-PEACl, exhibited substantially greater performance than control and even superior to the PEACl treatment. The observed enhancements were attributed to $n \geq 3$ LDPs, introduced by the addition of MAI. Replication with the CsMAFA perovskite was attempted to investigate the impact of these strategies on a slightly different absorber stoichiometry.

The analysis was initiated from the approach combining PEACl and MAI, adopting a 2:1 molar ratio of PEACl to MAI, following the experimental procedures by Chen et al. [25]. Moreover, the PEACl concentration was set to 6.7 mM, corresponding to two thirds

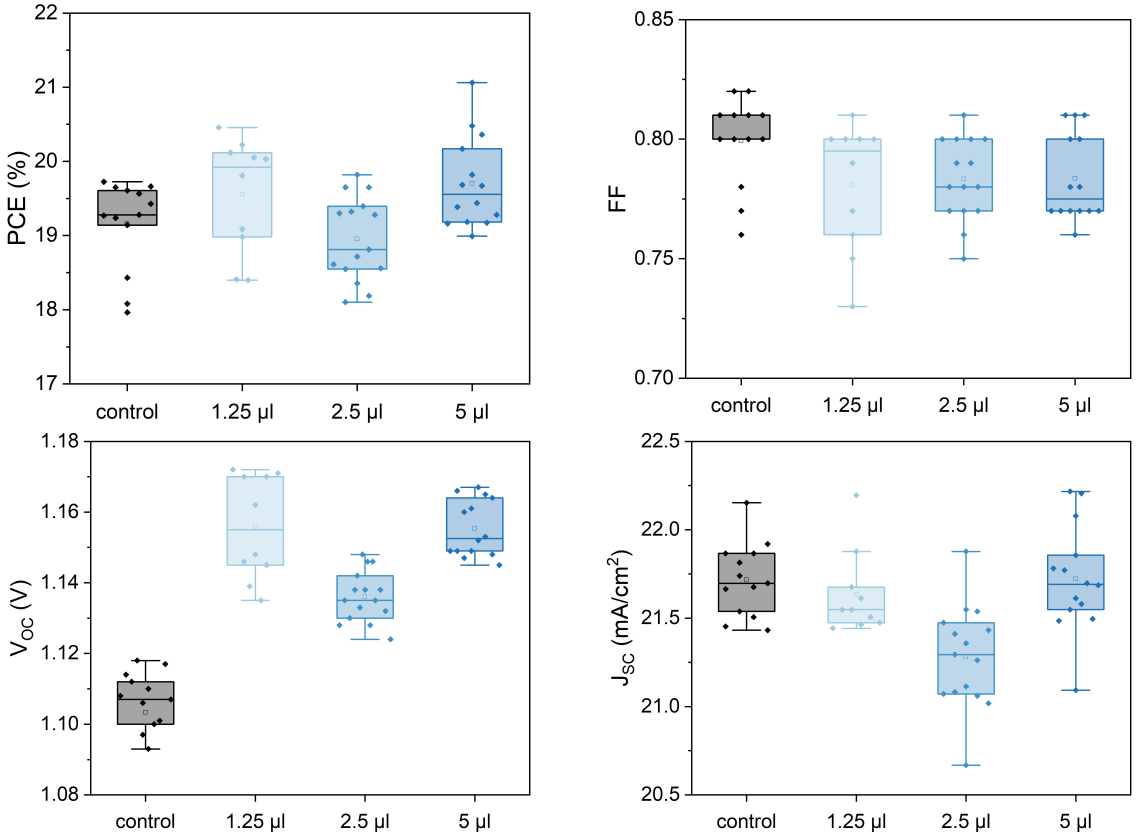

Figure 4.5.: Photovoltaic parameters of CsMAFA PSCs treated with PEACl and MAI in a 2:1 molar ratio comparing different DMF contents. The abbreviations stand for power conversion efficiency (PCE), fill factor (FF), open-circuit voltage (V_{OC}), and short-circuit current density (J_{SC}).

of the simple PEACl treatment content presented in the precedent section. The effect of DMF was firstly studied for optimization, revealing that a small addition of 1.25 µl per ml of IPA was sufficient to enable enhanced PCE, supposedly by partial dissolution of the absorber and MAI incorporation into the lattice. This concentration was tested against 2.5 and 5 µl, revealing quite similar effects on PV parameters, with the outcome displayed in Fig. 4.5. Importantly, the dual strategies did not reduce significantly the J_{SC}, consequently boosting PCE above the control group. The V_{OC} improvements of 40 to 50 mV, instead, match the single PEACl treatment, proving the potential of this approach in producing superior PCE. The lowest amount was adopted for all subsequent experiments involving dual procedures.

As a second step the PEACl to MAI ratio was tackled, comparing molar proportions of 4:1, 2:1, and 1:1. The 2D ligand content was kept constant at 6.7 mM, while the MAI amount was altered. These quasi-2D treatments were compared against the previous 10 mM PEACl solution, as detailed in Fig. 4.6. The four groups exhibit very similar FF and V_{OC}, standing at 0.78 and 1.14 V respectively, whereas the current determined the PCE trend, with the 2:1 film being the best performing. This outcome, in agreement with what is detailed in the work by Chen et al. [25], confirms the greater capacity of the dual treatment

in enhancing PCE. Moreover, dual methods attenuated the hysteretic behavior of treated devices, lowering the mean hysteresis index from 2.88% to 2.05% for the 2:1 molar ratio.

The 2:1 molar fraction was deemed the overall best combination and thus employed for subsequent dual strategies.

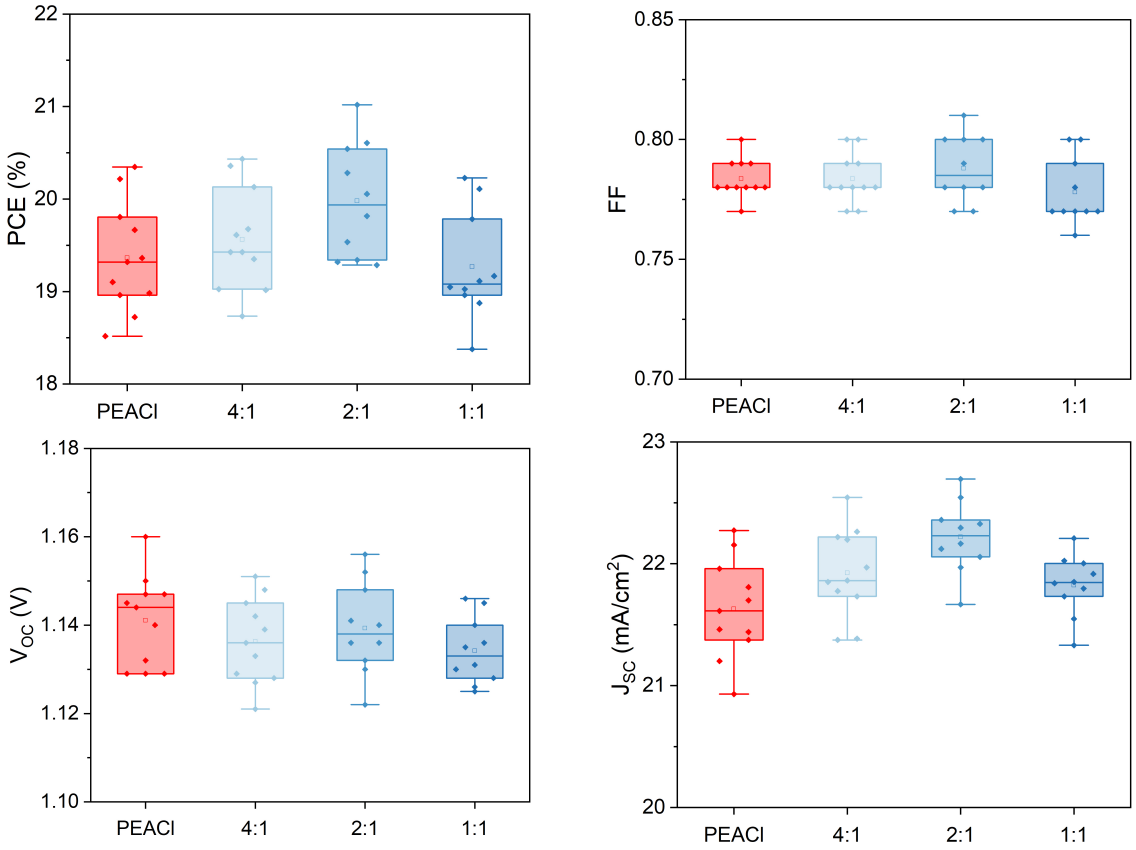

Figure 4.6.: Photovoltaic parameters of CsMAFA PSCs treated with PEACl and MAI in molar ratios of 4:1, 2:1, and 1:1. The abbreviations stand for power conversion efficiency (PCE), fill factor (FF), open-circuit voltage (V_{OC}), and short-circuit current density (J_{SC}).

Subsequently, a second scan of PEA salts was undertaken with the aim of isolating the different effect of combined strategies when compared against single treatments, since the combination of PEACl and MAI (6.7 and 3.3 mM respectively) demonstrated the greatest potential so far. PEACl, PEABr, and PEAI, the latter in a lower concentration of 3.3 mM, were tested against each other when coupled with MAI, always in a 2:1 molar ratio. Additionally, in a second PEACl group, MAI was replaced with FAI, in equal molar content, to test whether the effects on the multiple PV parameters are unique to the perovskite precursor or not.

At this stage the light soaking effect was individuated as cause of result manipulation during the measurement phase. PSCs based on the CsMAFA composition were previously assumed to be unaffected by this issue since the control devices always behaved very consistently across multiple J-V scans. The statistical data, plotted in Fig. 4.7, demonstrate

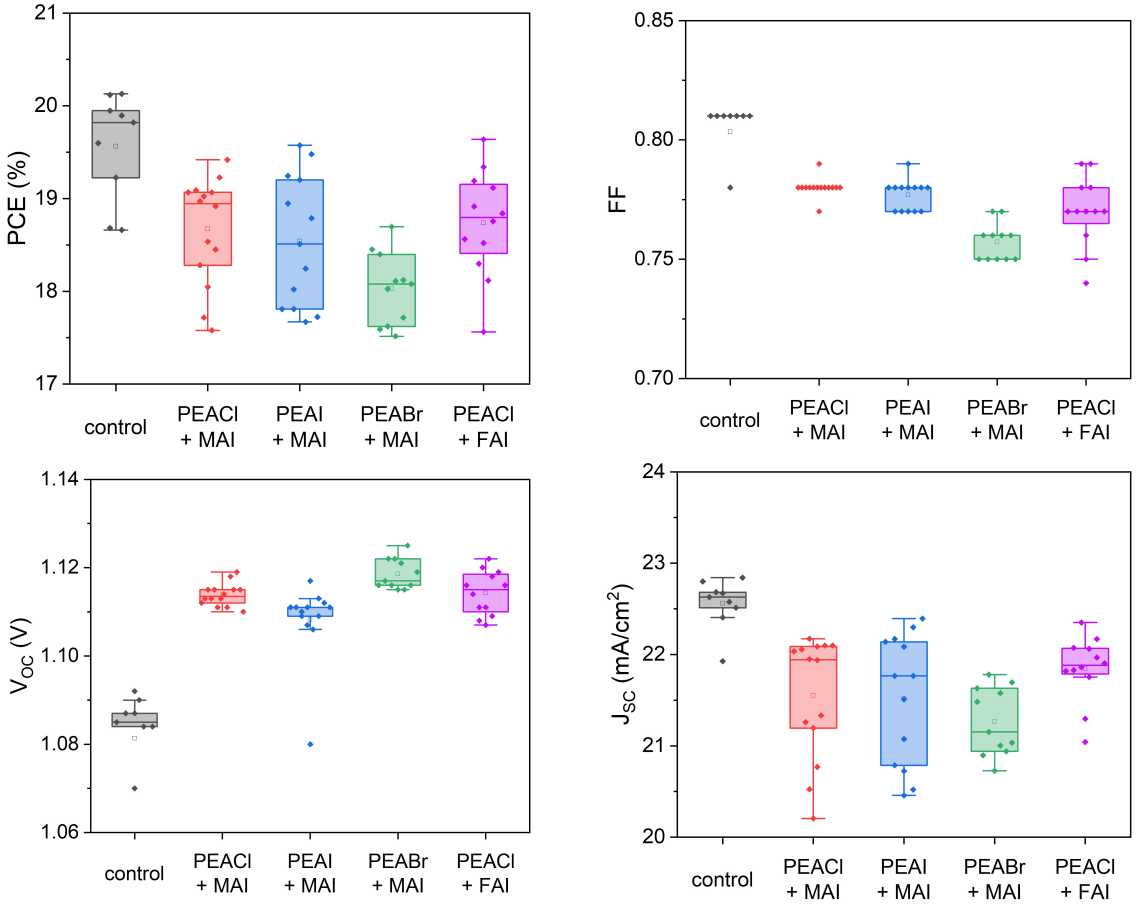

Figure 4.7.: Photovoltaic parameters of CsMAFA PSCs treated with PEACl, PEAI, and PEABr in combination with methylammonium iodide (MAI) or formamidinium iodide (FAI) in 2:1 molar ratio. Data obtained using a shadow mask and after one minute of light soaking time. The abbreviations stand for power conversion efficiency (PCE), fill factor (FF), open-circuit voltage (V_{OC}), and short-circuit current density (J_{SC}).

how light soaking for 1 minute, introduced to equalize the testing conditions, entirely nullified the PCE gain over the reference group previously observed. In particular, FF and J_{SC} were substantially lower when compared to not light soaked measurements, portraying the treatment strategies as ineffective in boosting PCE. On the other hand, V_{OC} was not impacted at all by the light soaking time, although it was lowered by the presence of the shadow mask on top of the sample during measurement. This precaution was adopted for the present and subsequent series of tests to restrict the illuminated area, avoiding uncertainties in the active area extension.

The technique containing PEABr remained the most effective at enhancing V_{OC}, though the FF and J_{SC} reductions were significant. Conversely, PEAI could achieve approximately the same V_{OC} gain, even though half of the regular concentration was used (3.3 mM vs 6.7 mM). No significant PCE difference could be detected among PSCs treated with either PEAI or PEACl, confirming the precedent results. Concerning the perovskite precursors, the

effects on PV parameters proved to be identical when using MAI or FAI in the treatment solution, potentially expanding application to MA-free perovskite stoichiometries.

MPPT tracking tests were carried out for champion devices out of each group to determine the real performance of treated PSCs. The results, presented in Fig. 4.8, contradicted the last J-V scans and corroborated previous observations indicating the overall efficiency gain due to surface modification. In fact, performing the measurements immediately after illumination start it was possible to obtain again superior PCE, restating the superiority of dual methods in boosting PCE, mostly because of higher J_{SC}. In particular, the PEACl+MAI approach proved to be the best one, despite not being the most effective in enhancing V_{OC}.

With these numbers it was concluded that: measuring the current-voltage characteristic minimizing time under illumination provides the best estimation of real device performance during MPPT. However, changing the measurement setup was not an option due to logistics constraints, therefore later PSCs were also measured after one minute of light soaking, not to bias the results based on the device position on the substrate. MPPT measurements were also performed for next fabricated devices, since the objective was to reach actual PCE gains and not trivial performance improvements in fast J-V scans.

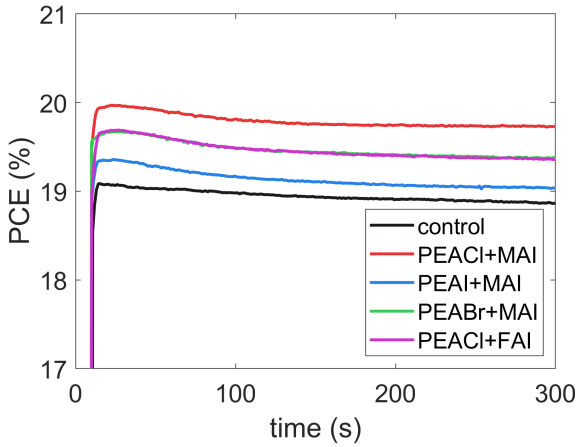

Figure 4.8.: Maximum power point tracking test of CsMAFA PSCs treated with PEACl, PEAI, and PEABr combined with either methylammonium iodide (MAI) or formamidinium iodide (FAI) in 2:1 molar ratio. Data obtained using a shadow mask. The abbreviation PCE stands for power conversion efficiency.

In conclusion, the same dual approach was applied to different fluorinated PEA salts, as presented in Ref. [25], keeping molar quantities and ratios unchanged, i.e. 6.7 and 3.3 mM for 2D ligand and MAI respectively. Concentrations were left unaltered from the previous experiment to highlight the differences induced by the extra fluorine atom, thus a diminished 3F-PEAI content (3.3 mM) was utilized.

The new results, reported in Fig. 4.9, displayed slightly lower V_{OC} gains than non-fluorinated PEA salts, around 30 mV in this case. However, FF and J_{SC} were reduced in comparison to the previous outcome, consequently determining PCEs meaningfully inferior to the reference. The 3F-PEABr treatment reached again the greatest V_{OC}, as reported for regular dual strategies, although it was also the worst performing in terms of J_{SC} and FF, substantially impairing the PCE. On the other hand, the 3F-PEAI solution

demonstrated a slightly lower voltage improvement, presumably because of the diminished salt concentration.

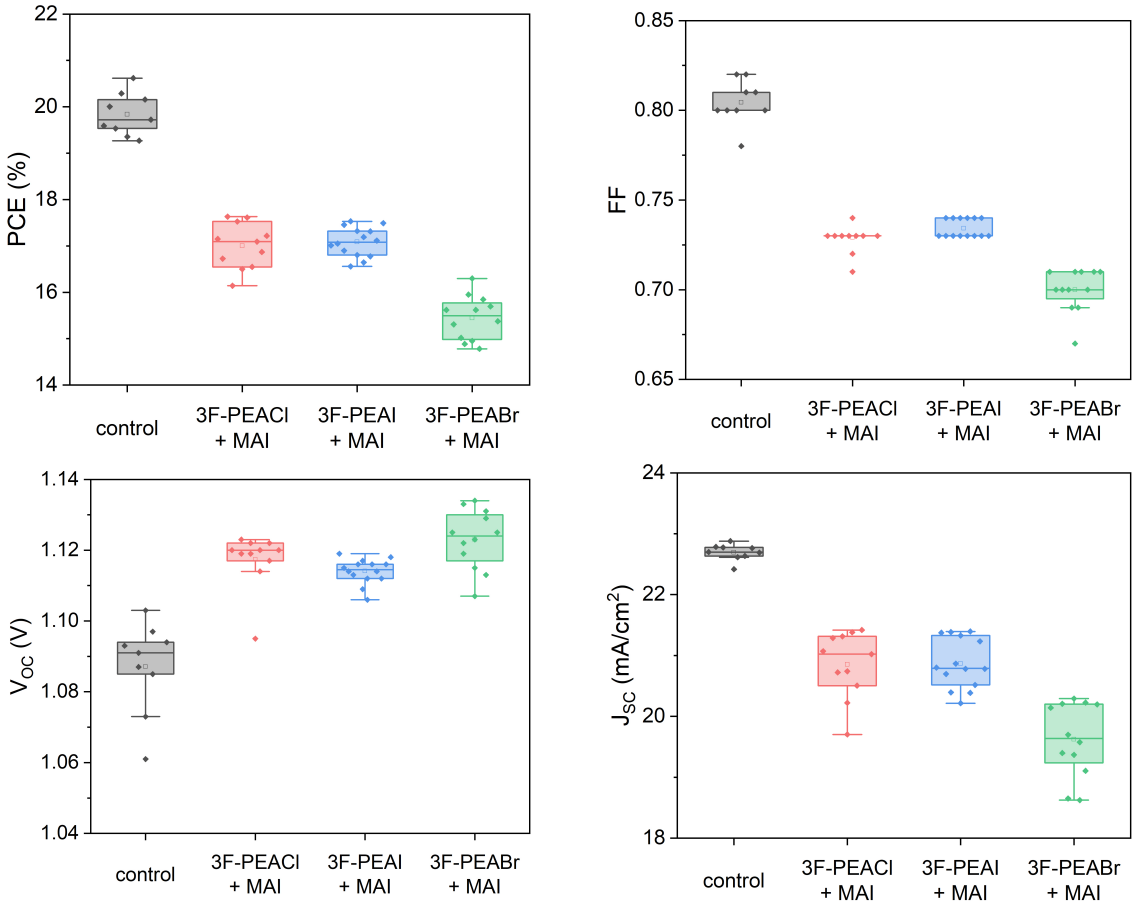

Figure 4.9.: Photovoltaic parameters of CsMAFA PSCs treated with fluorinated PEA salts in combination with methylammonium iodide (MAI) in 2:1 molar ratio. Data obtained using a shadow mask and after one minute of light soaking time. The abbreviations stand for power conversion efficiency (PCE), fill factor (FF), open-circuit voltage (V_{OC}), and short-circuit current density (J_{SC}).

For the reasons mentioned earlier, MPPT data are reported in Fig. 4.10 to effectively evaluate PV performance induced by surface modification. Once again, treated devices demonstrated higher PCE in real working conditions as compared to J-V scans performed after stabilization in illuminated open circuit conditions, exposing the consistency of this effect. In particular, fluorinated salts containing chlorine and iodine were confirmed as the best suited for application with the CsMAFA perovskite composition, with the 3F-PEAI demonstrating the highest PCE, although not by a significant margin. Fluorinated PEABr, in turn, manifested efficiencies inferior to the control group, essentially caused by reduced current density, as noted above in the PV characterization. Notably, all treatments proved superior PCE stability over the tested time period, with 3F-PEABr presenting the best example of this feature that could be caused by the hydrophobic properties of fluorinated chemical compounds.

Looking at these data, fluorinated PEA compounds exhibited inferior performance when compared to non-fluorinated salts, in view of greater FF and J_{SC} drops when applied to the CsMAFA perovskite composition. The decreased PV performance could be attributed to the different stacking of the perovskite layers in the 2D structure, caused by the extra fluorine atom as proved by Hu and coworkers [93]. Nonetheless, further characterization to support this claim was not undertaken because of time constraints.

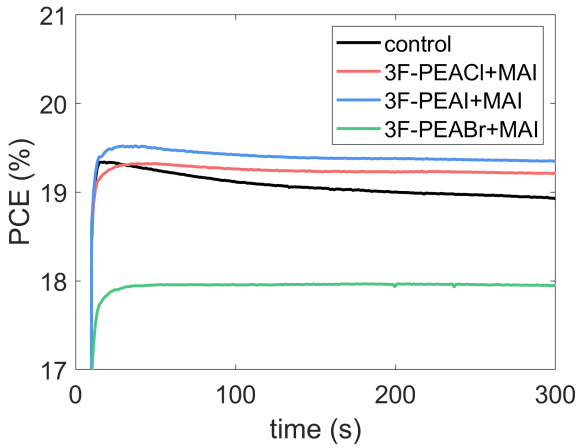

Figure 4.10.: Maximum power point tracking test of CsMAFA PSCs treated with fluorinated PEACl, PEAI, and PEABr combined with methylammonium iodide (MAI) in 2:1 molar ratio. Data obtained using a shadow mask. The abbreviation PCE stands for power conversion efficiency.

As last optimization step, the concentration of dual strategies, holding constant the 2:1 molar ratio between PEA salt and perovskite precursor, was tackled. Since the deficit in J_{SC} could be attenuated with the addition of MAI, it was speculated that the optimal 2D ligand amount in combined treatments was higher than in procedures employing only the PEA salt. The pair of PEACl and MAI was singled out as representative group for this study. The selected concentrations amount to 70, 100, 150, and 200% of the original values, standing at 6.7 and 3.3 mM for PEACl and MAI respectively. The expected trends, namely rising V_{OC}, dropping J_{SC}, and softly declining FF moving to higher concentrations could be clearly observed in the data reported in the Appendix A.2. Quantities above the starting point demonstrated mediocre efficiencies, whereas no clear difference was detected between 70% and 100% values, thus this route was investigated no further.

4.1.3. Dual surface treatment with phenethylammonium salts and trimethylphenylammonium tribromide

After the successful substitution of MAI with FAI in the dual surface modification approach, other compounds were considered as perovskite precursor replacement. The remaining perovskite forming chemicals used in the CsMAFA bulk composition, namely PbI_2, $PbBr_2$, and CsI, were ruled out since they do not dissolve meaningfully in IPA. Eventually, a newly presented material, trimethylphenylammonium tribromide ($TPABr_3$), was chosen to examine the role of the perovskite forming compound in dual treatments. $TPABr_3$

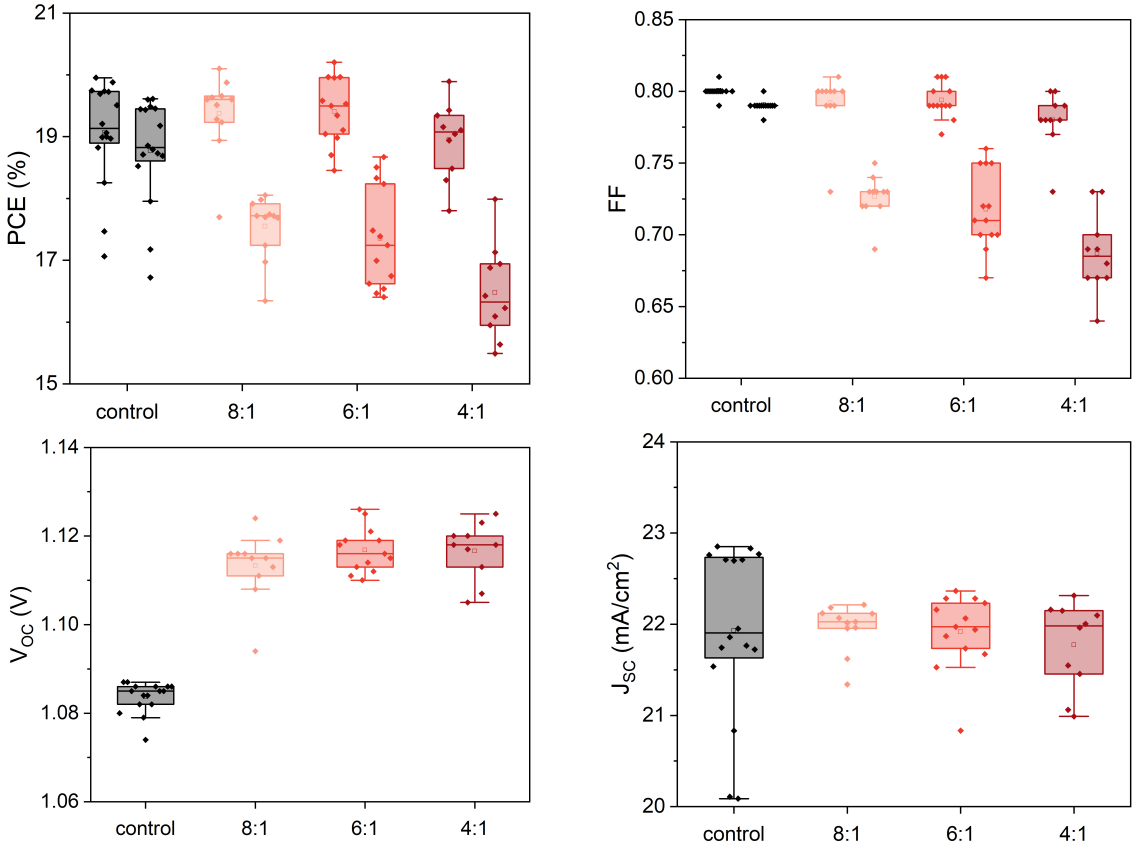

Figure 4.11.: Photovoltaic parameters of CsMAFA PSCs treated with PEACl and $TPABr_3$ in 8:1, 6:1, and 4:1 molar ratios. Data obtained using a shadow mask and after one minute of light soaking time. The abbreviations stand for power conversion efficiency (PCE), fill factor (FF), open-circuit voltage (V_{OC}), and short-circuit current density (J_{SC})

was recently reported to substantially decrease the V_{OC} deficit of wide bandgap PSCs, when used as bulk additive in combination with PEACl and other compounds [54]. The above-mentioned effect was attributed to reduced iodine interstitial defect density, caused by the presence of bromine in the absorber composition.

The newly developed surface modification approach was built on top of previous investigation by selecting the same PEACl concentration, namely 6.7 mM. Seeking to maximize V_{OC} improvements, $TPABr_3$ quantity was optimized first. Molar ratios of 8:1, 6:1, and 4:1 of PEACl to $TPABr_3$ were selected for this analysis.

The obtained results, shown in Fig. 4.11, put in evidence a clear V_{OC} boost of 30 mV for all treatment groups. Additional $TPABr_3$ provided only a minor increase, in contrast to what expected, questioning the real functioning mechanism of this chemical in presence of defects. Conversely, PCE and FF data displayed a great impact caused by the presence of $TPABr_3$, especially visible when comparing opposite scan directions. The higher the $TPABr_3$ concentration the greater the hysteresis observed, primarily characterized by a drop in FF. The mean hysteresis index soared from 1.55% of the control group to 9.4%

and 13.1% of the PSCs treated with the 8:1 and 4:1 solutions, respectively. Values for V_{OC} and J_{SC} in forward scan have not been reproduced since the hysteresis influence was not significant.

MPPT measurements were carried out as usual for the reasons already exposed in precedence. The outcome, provided in Fig. 4.12a, proved that stabilized PCEs of the treated devices lie in close proximity of the reverse scan efficiencies, thus not exceeding reference group values. Importantly, power output stability was positively correlated with $TPABr_3$ amounts, with the 4:1 ratio displaying remarkably flat PCE curves. This finding prompted more extensive tests to probe long term stability of these devices.

PCE was tracked for a duration of 100 hours to analyze performance degradation under light. Normalized time evolutions of champion devices, plotted in Fig. 4.12b, uncovered a drastically different behavior, highlighting the unstable nature of treated samples, although $TPABr_3$ content was again correlated with slower PCE decay. Conversely, the reference group demonstrated superb stability, retaining in full the initial efficiency. Statistical data regarding the long-term stability test are included in Appendix A.3 and corroborate the reached conclusion.

Such outcome evidenced the new and largely unknown properties of multi-dimensional PSCs, especially when based on the CsMAFA stoichiometry, calling for more extensive and rigorous testing.

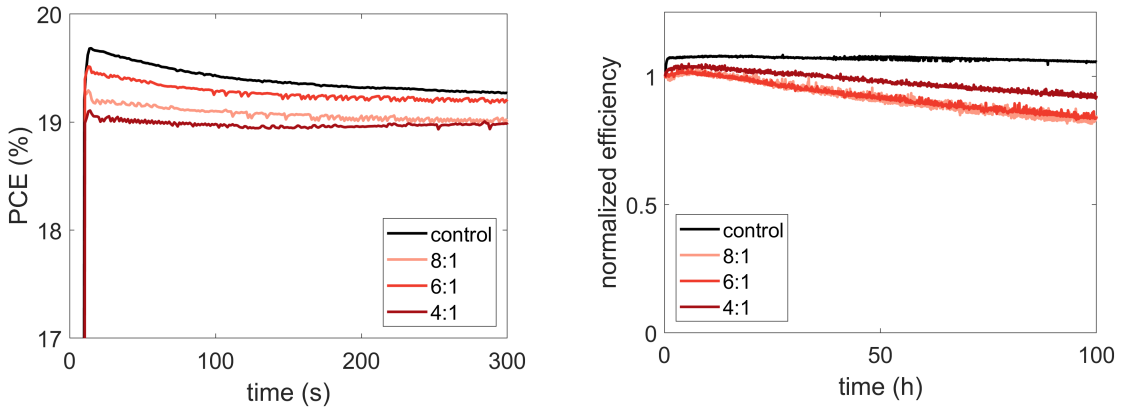

Figure 4.12.: Maximum power point tracking tests of CsMAFA PSCs treated with PEACl and $TPABr_3$ in 8:1, 6:1, and 4:1 molar ratios, recorded for a time period of 300 s (a) and 100 hours (b). Data obtained using a shadow mask. The abbreviation PCE stands for power conversion efficiency.

4.1.4. Application of dual strategies to double cation perovskites

Overall, the previous Section 4.1.2 demonstrated that dual treatments are more effective in enhancing PCE than single PEA salt solutions, at least when applied to the CsMAFA stoichiometry. This result motivated further application of the same approaches to the simpler CsFA perovskite, as an attempt to surpass the already good improvement obtained with the 10 mM PEACl solution. Among all the presented procedures, surface modification

procedures based on non-fluorinated PEACl paired with MAI or FAI were analyzed first and stacked against the precedent PEACl group. Since previous experiments indicated similar optimal concentrations between the two compositions, equal optimized molar quantities and ratios were employed, i.e. 6.7 mM for PEACl and 3.3 mM for MAI or FAI.

A statistical representation of the usual PV parameters is presented in Fig. 4.13, obtained after the usual light soaking time. As introduced earlier, PV performance was significantly increased upon waiting in light soaking conditions for control and treated devices, producing gains in PCE of up to $3\%_{abs}$. When comparing the different approaches no important differences could be isolated, leading to the conclusion that the studied strategies are substantially equivalent. All treatment groups could increase V_{OC} by 40 mV without any decline in FF and J_{SC}, resulting in close to $1\%_{abs}$ enhancements of PCE. The single PEACl treatment provided a greater, even if slightly, PCE boost. Notably, MAI and FAI turned out to work identically, although CsFA bulk composition does not contain the MA cation.

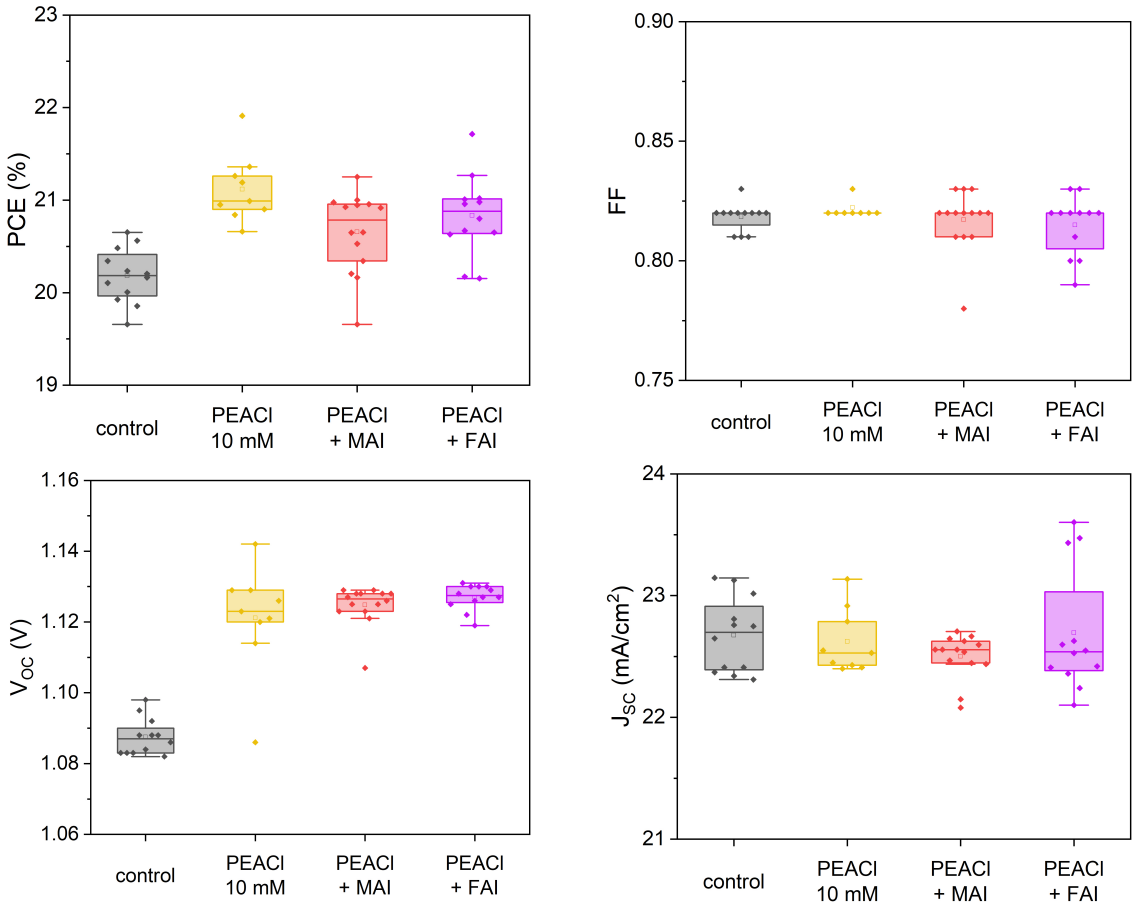

Figure 4.13.: Photovoltaic parameters of CsFA PSCs treated with single and dual strategies based either solely on PEACl, or PEACl in combination with methylammonium iodide (MAI) or formamidinium iodide (FAI). Data obtained after one minute of light soaking time. The abbreviations stand for power conversion efficiency (PCE), fill factor (FF), open-circuit voltage (V_{OC}), and short-circuit current density (J_{SC}).

The precedent outcome was also supported by MPPT measurements displayed in Fig. 4.14, carried out to confirm the PCE improvements. In contrast to what observed previously with the CsMAFA perovskite, J-V scans of treated CsFA PSCs in light soaking conditions proved to be more predictive of real MPPT performance. All devices performed below expectations, an effect that could be due to limited shelf stability, since the samples were stored for three weeks in a nitrogen atmosphere before MPPT testing. MPPT was also performed for a few champion devices right after device fabrication, revealing excellent correlation between MPPT and J-V scan results. The details are included in Appendix A.3.

Overall, treated PSCs demonstrated greater stability and about $1\%_{abs}$ higher PCE compared to the control, indicating that the beneficial effects of surface modification are long lasting. The three approaches proved to be equally effective, with no clear difference in any PV parameter, indicating the higher efficacy of treatments with the CsFA stoichiometry. Such outcome could be attributed to the absence of Br in the bulk composition, since the results from Chen et al. were also obtained with a single-halogen perovskite [25].

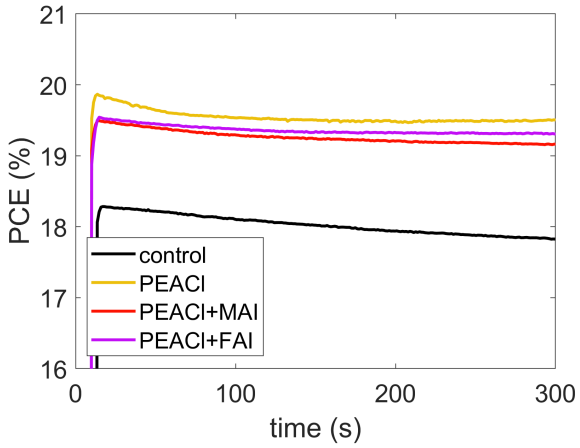

Figure 4.14.: Maximum power point tracking test of CsFA PSCs treated with single, 10 mM PEACl, and dual strategies, PEACl coupled with methylammonium iodide (MAI) or formamidinium iodide (FAI). Data obtained using a shadow mask. The abbreviation PCE stands for power conversion efficiency.

Subsequently, fluorinated compounds, namely 3F-PEACl and 3F-PEAI, were applied to the CsFA stoichiometry to test whether they have different impacts on a simpler bulk composition. Fluorinated PEABr was not tested, since the regular PEABr was previously found to be ineffective with the CsMAFA perovskite and also with the CsFA composition [24]. MAI was selected as additive since it demonstrated to work perfectly well with the CsFA perovskite. Dual strategies proved to be slightly less effective when compared with precedent results, as displayed in Fig. 4.15. Namely, slight reductions in FF and J_{SC} hampered PCE, producing only a small efficiency boost. Nonetheless, treated PSCs displayed very good performances, achieving FF of 80% and J_{SC} exceeding 22 mA/cm^2. The treatment containing 3F-PEAI enhanced V_{OC} only by 30 mV, perhaps due to the decreased 2D ligand concentration (3.3 mM), contributing to the lower than expected performance.

MPPT measurements were regularly performed to substantiate the recorded J-V scans and are plotted in Fig. 4.16. Once again, JV curves of CsFA PSCs confirmed the high

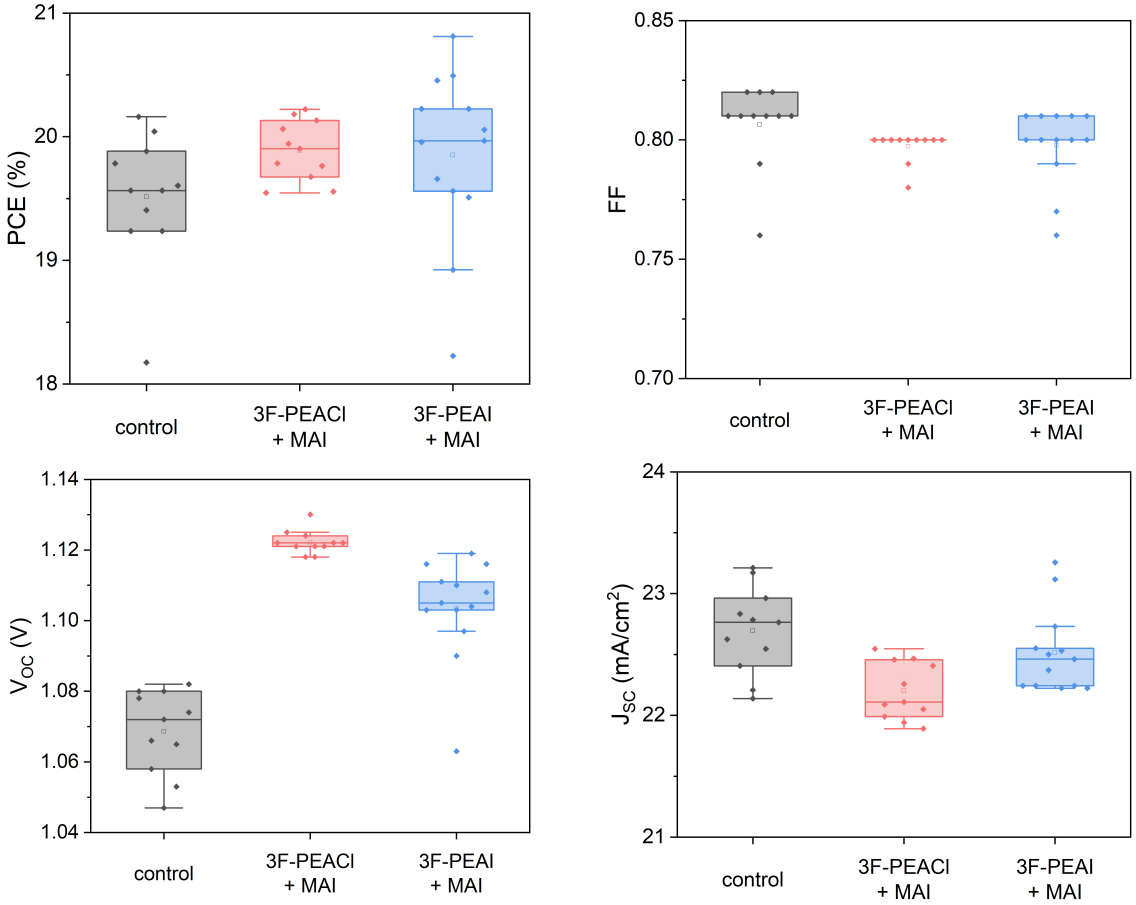

Figure 4.15.: Photovoltaic parameters of CsFA PSCs treated with dual strategies based on 3F-PEACl and 3F-PEAI coupled with methylammonium iodide (MAI). Data obtained after one minute of light soaking time. The abbreviations stand for power conversion efficiency (PCE), fill factor (FF), open-circuit voltage (V_{OC}), and short-circuit current density (J_{SC})

predictability of MPPT efficiency, restating the more stable behavior of treated devices based on this stoichiometry. PCE time evolutions display a wider efficiency gain for the treated PSCs, roughly $2\%_{abs}$, although this effect might be due to control device degradation prior to MPPT tests, performed three weeks after device fabrication.

In conclusion, dual methods proved to be effective in increasing PCE of double-cation CsFA PSCs, even though they did not appear to be superior to single PEA salt treatments. Further boosts in FF and J_{SC} above the reference values were not achieved, thus limiting the improvements to the V_{OC}. Fluorinated salts were proved suboptimal also with the CsFA composition, although MPPT stability could be greater than in PSCs treated with regular PEA compounds. Overall, surface modification approaches confirmed their greater efficacy when applied to the CsFA stoichiometry; however, the cause of this behavior was not identified.

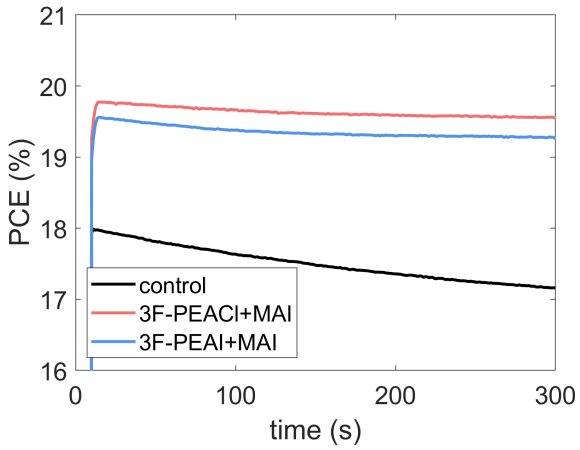

Figure 4.16.: Maximum power point tracking test of CsFA PSCs treated with dual strategies employing 3F-PEACl and 3F-PEAI coupled with methylammonium iodide (MAI). Data obtained using a shadow mask. The abbreviation PCE stands for power conversion efficiency.

4.2. Photoluminescence quantum yield results

Upon completing the analysis of the presented surface strategies, further investigation was undertaken to probe the origin of the enhanced open circuit voltage. Photoluminescence quantum yield (PLQY), as already introduced in Section 2.1.4, provides great insights into the voltage loss caused by non-radiative recombination taking place at the perovskite/C_{60} interface. Therefore, PLQY was measured for the dual treatment groups including non-fluorinated PEA salts to highlight the voltage improvements dependence on the halide ion. The previous molar concentrations were employed, namely 6.7 and 3.3 mM for 2D ligand and MAI respectively, with the exception of PEAI, for which half of the mentioned amount was included. The 2:1 molar ratio was always respected.

Results of dual strategies, including values under normal and light soaking conditions, are shown in Fig. 4.17 including samples with and without ETL. All three groups demonstrated close to 40 mV $V_{OC,imp}$ increases when the ETL is present, confirming the sought achievements. The PEABr group, as previously observed, proved to be the best compound to boost voltage, although this came with a J_{SC} loss. For stacks lacking the C_{60} layer the improvements were more modest, reaching around 30 mV also for PEAI, in spite of the lower concentration. Additionally, after waiting for one minute of light soaking the same devices displayed an interesting, though marginal, behavior. ETL-free stacks improved their $V_{OC,imp}$, whereas when including the transport layer the values were slightly reduced. No clear cause of this small changes has been identified.

This result largely confirms precedent characterization, supporting the superior V_{OC} values noticed in J-V scans. To clarify, this set of data was obtained with a different instrument setup, explaining why the $V_{OC,imp}$ of all groups including the ETL was inferior to the complete device V_{OC}, measured with the solar simulators. More in detail, the laser intensity was not adjusted to match the same charge carrier density as under 1 sun illumination, skewing all results downwards.

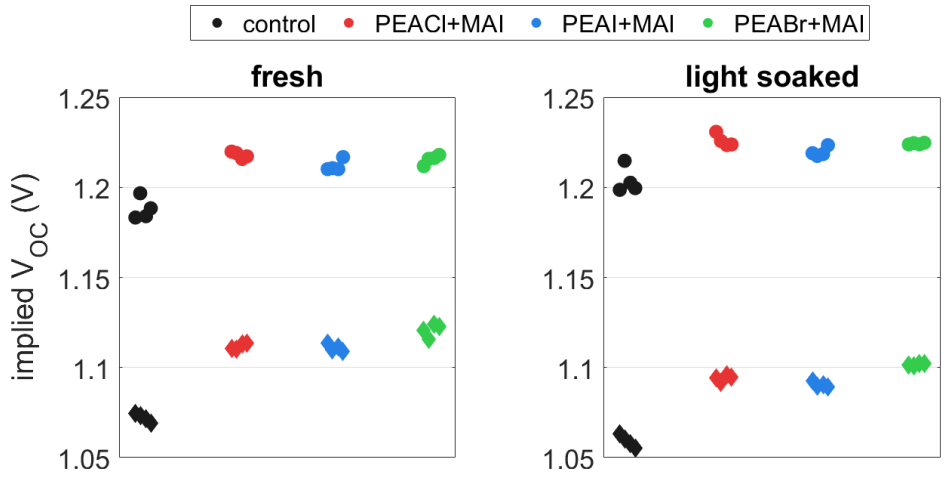

Figure 4.17.: Statistics of implied open circuit voltage for control and treated CsMAFA devices with (diamonds) and without (circles) electron transport layer. Dual surface modification strategies, employing PEACl, PEAI, and PEABr, were analyzed. Light soaking measurements have been performed after one minute of illumination.

Subsequently, simple and dual treatment approaches based on PEACl have been compared to better comprehend the role of additives, i.e. perovskite precursors, in superficial SRH recombination reduction. The selected groups included, other than the simple 10 mM PEACl treatment, dual strategies combining PEACl with one amongst MAI, FAI, and $TPABr_3$. All molar concentrations and ratios were left unchanged from the previous sections. Fig. 4.18 depicts the calculated implied voltage, indicated as $V_{OC,imp,C60}$ because of the presence of the ETL, in relation to the radiative limit defined by Eq. 3.6, named $V_{OC,rad}$. To be noted, these values were obtained from a different batch of fabricated PSCs and with a different measurement setup, explaining the discrepancies in $V_{OC,imp}$ of control and treated devices in comparison to Fig. 4.17.

As detected in precedence, the analyzed surface modification techniques enhanced the $V_{OC,imp,C60}$ by around 40 mV, in accordance with the measured current-voltage curves. The simple PEACl treatment was the most effective in increasing implied voltage, although its reduction under light soaking conditions was also the greatest. Conversely, dual strategies, aside from the PEACl+FAI mixture, demonstrated more stable gains, in agreement with the less pronounced hysteretic behavior in J-V scans. As noted before, the perovskite precursor in dual treatments did not play a significant role in boosting $V_{OC,imp,C60}$, demonstrating scarce selectivity of these treatments. This finding, in combination with the successful application of PEACl and MAI to the CsFA perovskite, points to the possibility of widespread employment of such procedures, extending the research to other stoichiometries.

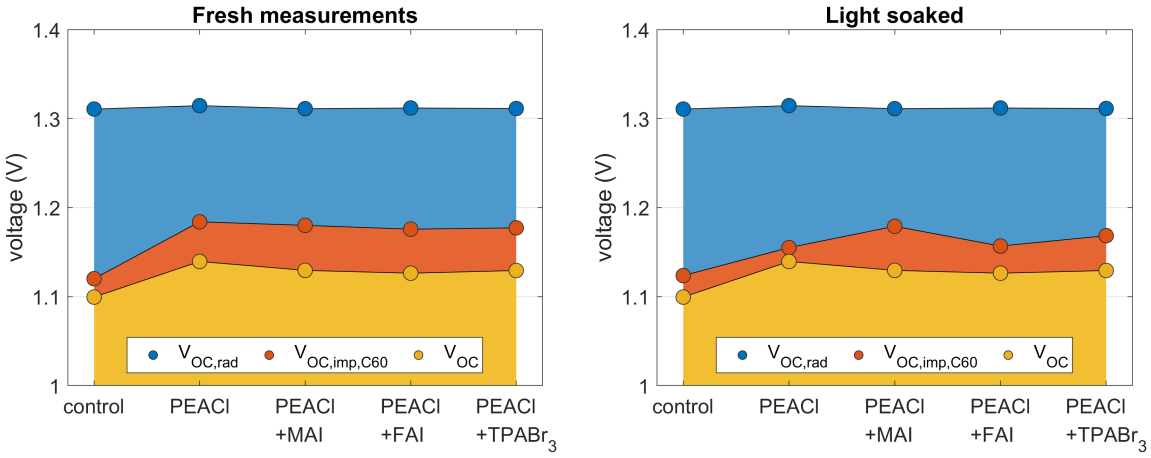

(a) (b)

Figure 4.18.: Implied open circuit voltages for single and dual treatment strategies based on PEACl compared to the CsMAFA reference. Best implied voltages are reported for samples with and without electron transport layer. The same samples have been measured without (a) and with one minute of light soaking (b).

4.3. Charge carrier extraction

The second technique employed to evaluate charge carrier recombination in PSCs is the CELIV method, described in Section 3.4.5. Dark- and photo-CELIV transient current evolution data have been combined to calculate charge carrier mobility (μ) and extracted charge carrier density (N_{extr}), important values evaluating extraction efficiency of photogenerated electron-hole pairs in PSCs. Such characterization was carried out for the most important newly developed strategies, with the aim of analyzing the effect of surface treatments on the extraction parameters.

To provide a clear comparison amongst various molar ratios for dual methods, solutions containing PEACl and MAI were selected for this study, adopting once again proportions of 4:1, 2:1, and 1:1. Such treatments were evaluated against the reference group, nicely revealing the surface modification effects. Fig. 4.19a, representing the extracted carriers in function of the photo-CELIV delay time, shows meaningfully higher values for treated samples, especially for 2:1 and 1:1 ratios, due to slower recombination rates. However, the sought improvements in SRH recombination reduction came at the cost of charge carrier mobility, highlighted in Fig. 4.19b. In this respect, the control devices presented a faster rise in photo-CELIV current transients, consequently having an earlier curve peak, which translated into higher mobility, according to Eq. 3.12. Hindered charge carrier mobility, probably due to the poorly conductive LDP layer in the treated PSCs, could also explain the slightly lower FF observed in precedence.

Moreover, dark current density of reference and treated samples were plotted in Fig. 4.19c, further supporting the claim of enhanced open circuit voltage. All strategies were successful in lowering saturation current, a sign of greater V_{OC}.

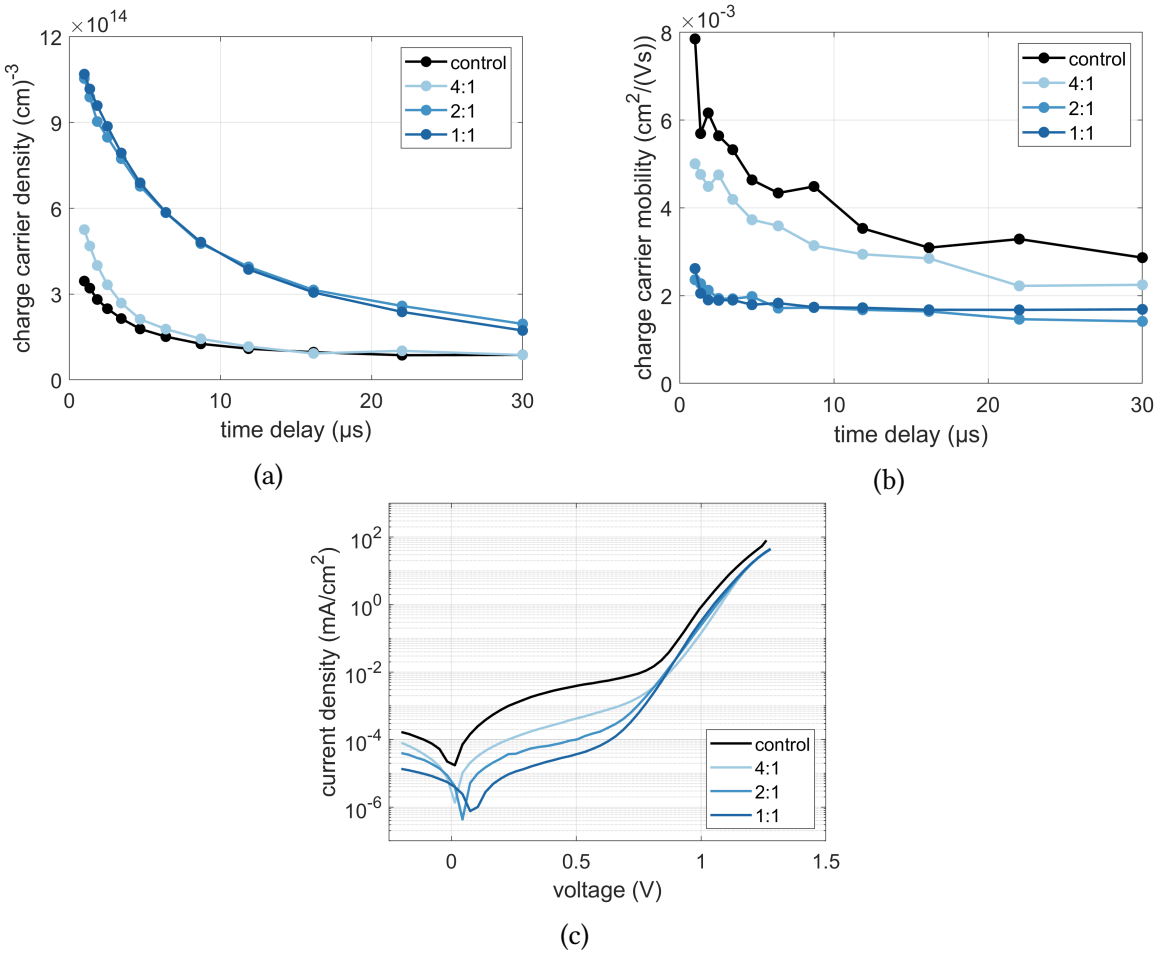

Figure 4.19.: Results extracted from photo- charge extraction with linearly increasing voltage (CELIV) for CsMAFA PSCs treated with PEACl+MAI solutions in 4:1, 2:1, and 1:1 ratios against control. (a) Extracted charge carrier density as a function of time delay. (b) Majority charge carrier mobility as a function of time delay. (c) Dark current-voltage curve.

The same effects, namely increased extracted carrier density and diminished mobility, were also noticed for the single PEACl treatment method, with the supporting data included in Appendix A.4. Charge extraction, due to the presence of PEACl, was substantially the same, although the greater PEA salt content provided even larger N_{extr}, whereas mobility was reduced by a greater extend compared to other treatment groups.

Subsequently, the same analysis was conducted on dual methods combining PEACl and $TPABr_3$, in order to evidence the differences induced by a different perovskite precursor. Molar proportions of 8:1, 6:1, and 4:1 were selected as previously. Extracted parameters, plotted in Fig. 4.20, demonstrated slightly different treatment effects due to the presence of $TPABr_3$. Extracted charge carrier density was improved by a factor of 3, similarly to what obtained for PEACl and MAI methods, whereas mobility was also enhanced by surface modification with $TPABr_3$, indicating the remarkably different properties of this compound in comparison to MAI. Both set of values were independent from the employed molar

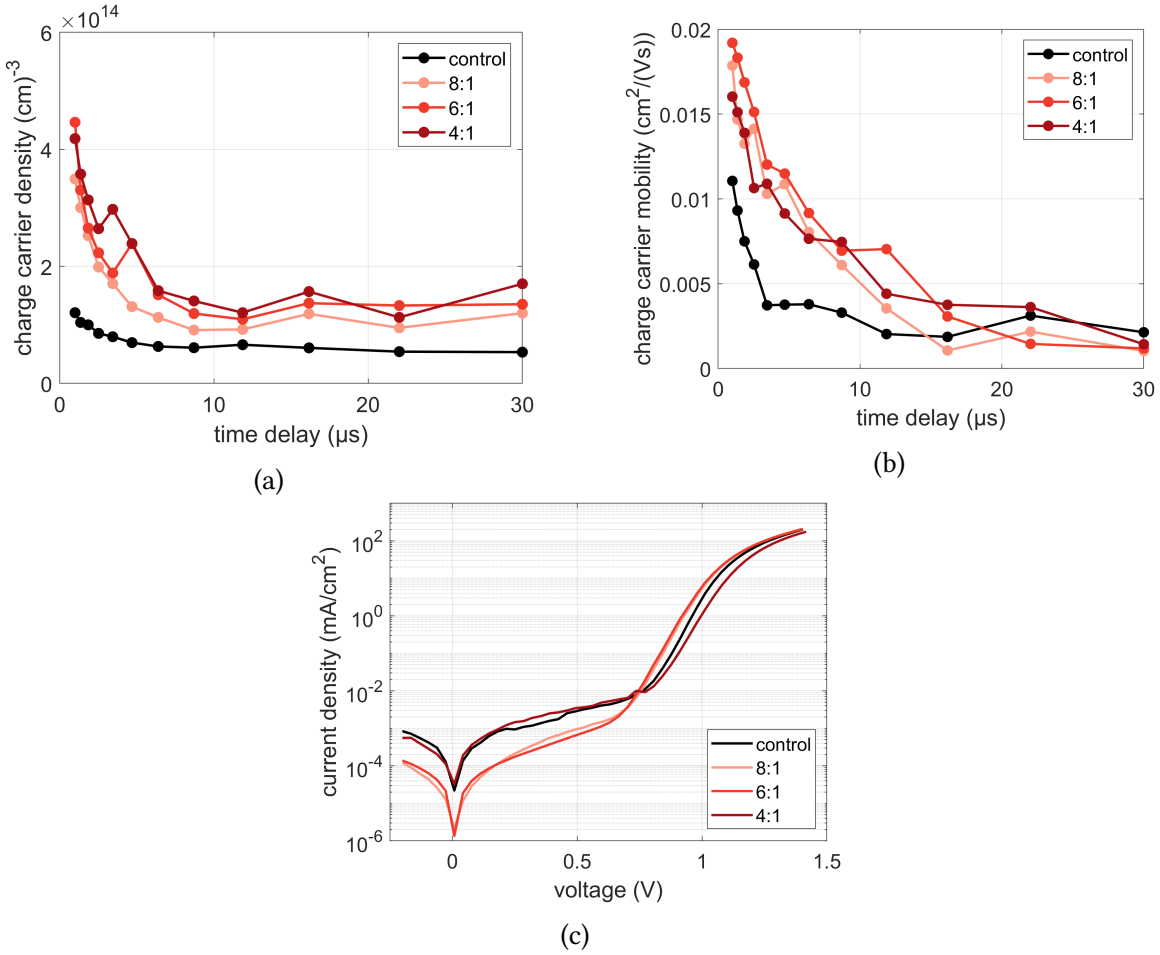

Figure 4.20.: Results extracted from photo- charge extraction with linearly increasing voltage (CELIV) for CsMAFA PSCs treated with PEACl+$TPABr_3$ solutions in 4:1, 2:1, and 1:1 ratios against control. (a) Extracted charge carrier density as a function of time delay. (b) Majority charge carrier mobility as a function of time delay. (c) Dark current-voltage curve.

ratio, suggesting that maybe a relatively small amount of $TPABr_3$ would be sufficient to enhance carrier mobility.

In addition, saturation current densities of PSCs treated with 8:1 and 6:1 solutions were significantly lower that reference values, pointing once again to the higher V_{OC} induced by superficial defect passivation.

In conclusion, $TPABr_3$ content was associated with increasing hysteretic behavior in current-voltage scans, though instability in MPPT measurements was associated with lower $TPABr_3$ content. Other unstable behaviors were not observed in the remaining PV parameters. Combinations of PEACl and $TPABr_3$, both being bulky organic compounds that do not fit inside the perovskite lattice, improved charge extraction of PSCs, stressing the largely unknown properties of these chemicals and their impacts on perovskite crystallization.

4.4. X-ray diffraction

As an addition to the results already presented, XRD characterization was implemented to prove the presence of LDPs in treated devices. Following what indicated in Section 3.4.6, concentrated solutions were prepared to allow easier detection of LDP peaks in the low incidence angle region. The illustrate the different LDPs introduced by the treatments analyzed in this work, one surface modification technique out of each major section was isolated. Namely, the 10 mM PEACl solution was taken as representative for the single treatments, whereas the selected dual method included PEACl coupled with MAI in 2:1 molar proportions.

The measured XRD spectra of control and above mentioned groups have been plotted in Fig. 4.21, with indication of the most interesting detected peaks. Following what reported in Ref. [26], LDP peaks were identified at various angles, all multiples of 5.3°, caused by $(00l)(l = 2m)$ 2D perovskite planes on the absorber surface treated with PEACl. In comparison the dual strategy did not form a similar structure, since none of the mentioned peaks could be detected, pointing to the substantially different 2D lattice. Another modest peak at 8.7° was observed for the PEACl+MAI group, possibly analogous to what observed at 8.2° in Ref. [25] and attributed to $n = 2$ LDPs. Lastly, the PEACl pattern presented a peak at 9.6° that could not be identified.

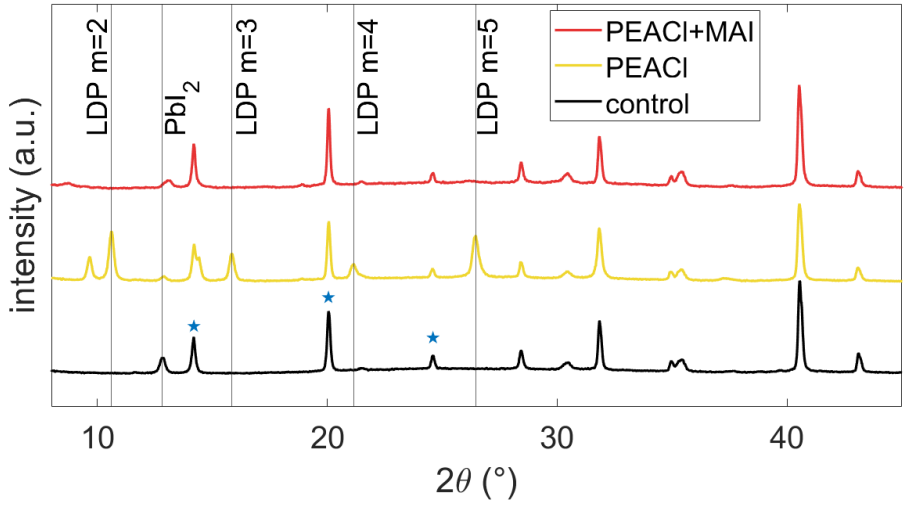

Figure 4.21.: X-ray diffraction pattern of reference CsMAFA films and CsMAFA samples treated with either the single solution based on PEACl, or the dual treatment combining PEACl and methylammonium iodide (MAI) (2:1 molar ratio). The concentrations were increased by a factor of 10 to enable clear identification of the diffraction peaks. Low dimensional perovskite (LDP) peaks, corresponding to $(00l)(l = 2m)$ planes, have been labeled for easier reading. The characteristic 3D perovskite peaks have been indicated with blue stars.

Surface engineering, especially the single method, significantly reduced the PbI_2 maximum intensity, suggesting integration of its excess into the LDP structure. Furthermore,

no shift in the perovskite peaks, present at angles of 14.2°, 20.1°, and 24.6°, was detected, indicating no modification of the original 3D lattice.

Overall, the single treatment demonstrated the greatest impacts in terms of LDP formation, whereas the dual strategy modified more subtly the perovskite surface, possibly forming thicker LDP as claimed in Ref. [25]. A greater share of $n = 1$ LDPs, due to the lower conductivity, is also in accordance with the lower J_{SC} of PSCs modified with single approaches.

5. Conclusion

In summary, this thesis analyses open circuit voltage losses caused by defect-assisted recombination at the perovskite/C_{60} interface of inverted PSCs. The investigation is conducted on single junction PSCs with the aim of future application of the best performing strategies in two-terminal tandem solar cells, fabricated by combining the PSC under focus with a $CuInSe_2$ bottom subcell, as detailed by Ruiz-Preciado et al. [94].

The newly developed surface modification methods are inspired by recent literature articles, attributing the efficacy of interface treatments based on large cations to successful defect passivation. Surface engineering is enacted by applying solutions of organic solvents, IPA and DMF, and PEA salts, pure or paired with perovskite precursors. Such solutions are spin coated on the formed perovskite absorber prior to the electron transport layer evaporation, producing a thin superficial 2D perovskite layer, capable of reducing Shockley-Read-Hall recombination rates. The effects of PEA salts composed by different halide ions, namely PEACl, PEAI, and PEABr, are studied by comparing PV parameters of PSCs treated with pure PEA salts dissolved in IPA. Molar concentration of 10 mM of either PEACl or PEABr is deemed optimal for single treatments, whereas PEAI performs best at 5 mM. Employing these amounts, open circuit voltage (V_{OC}) of CsMAFA PSCs can be enhanced by 30 to 40 mV, although fill factor (FF) and especially short circuit current density (J_{SC}) are decreased, resulting in overall inferior power conversion efficiency (PCE). This analysis evidences the greater V_{OC} boost provided by techniques based on PEABr, when adopting equal molar amounts; however this comes with significant drops in FF and J_{SC}, making it less suitable overall. The influences of annealing time and spin coating procedure are also investigated, though the effects on PV performance are rather small, halting further research.

Subsequently, the study moves on to treatment solutions prepared by combining a PEA salt with a perovskite precursor, in particular methylammonium iodide (MAI) or formamidinium iodide (FAI). These more complex, indicated as dual, strategies include a small addition of DMF to partially dissolve the absorber surface, with the goal of integrating its external layer in the 2D perovskite crystallization. First DMF content is studied, leading to the determination of 800:1 v/v as the most effective proportion between IPA and DMF. Afterwards, optimal molar ratio of 2:1 mol/mol between PEACl and MAI is identified, demonstrating V_{OC} increases similar to precedent strategies but reduced J_{SC} losses, confirming the greater potential of such approach. Different halogens are tested again in this framework, displaying a more complex behavior during the current-voltage scans. Measurements without light soaking period are predictive of real performance in maximum power point tracking (MPPT) tests, whereas waiting under illumination upon stabilization provides PCEs inferior to the reference. MPPT reveals how such surface modification techniques are effective in boosting PCE, with minor stability degradation up to 300 s. PSCs treated with a combination of PEACl and MAI demonstrate the greatest PCE

gain, exceeding the reference champion device by close to $1\%_{abs}$. Additionally, replacing MAI with FAI proves to be equivalent in current-voltage scans.

Afterwards, fluorinated PEA compounds, modified by the addition of a fluorine atom on the benzene ring, are tested in dual methods with molar concentrations equal to the non-fluorinated salts. Treated PSCs exhibit PCE gains not reaching $0.5\%_{abs}$, although stability in MPPT is enhanced. For this reason, fluorinated PEA salts are deemed not especially suitable for the CsMAFA perovskite composition.

Dual methods, replacing MAI with trimethylphenylammonium tribromide ($TPABr_3$), are also analyzed, though treated PSCs exhibit no improvements in PCE and increased hysteresis.

To investigate the influence of the absorber stoichiometry on the impacts of surface modification, optimized dual treatments are applied to a simpler double-cation perovskite, CsFA. Single and dual approaches are deemed largely equal, since they are similarly able to increase V_{OC} without any FF or J_{SC} deficits. In contrast to what observed with the CsMAFA composition, current-voltage sweeps under light soaking conditions are highly predictive of MPPT performance, both evidencing up to $1\%_{abs}$ advancements in PCE and increased output stability, the latter especially for fluorinated compounds.

Photoluminescence quantum yield tests are performed for a few treated CsMAFA PSCs, putting in evidence the roughly 40 mV voltage gain due to reduced recombination at the perovskite/C_{60} contact surface, confirming the sought achievements. Additionally, dual treatments exhibit minor performance degradation under light soaking conditions, supporting previous indications of superior efficacy. Charge extraction measurements, on the other hand, prove decreased charge carrier mobility in CsMAFA PSCs treated with PEACl and MAI, possibly caused by the poorly conductive 2D perovskite layer. The corresponding single strategy, removing MAI from the solution, demonstrates even lower carrier mobility, pointing to a minor low-dimensional perovskite (LDP) thickness n. Techniques employing PEACl plus $TPABr_3$, instead, have positive impacts on mobility and extracted charge carriers by limiting defect-assisted surface recombination. X-ray diffraction patterns suggest more extensive surface modification upon single treatment, with indications of thicker LDP layers when adding MAI to the solution.

Recapping the main findings, treated CsMAFA PSCs demonstrate enhancements in V_{OC} of around 30 mV, plotted in Fig. 5.1a, thus confirming the efficacy of PEA-based surface treatments. However, FF and J_{SC} are hindered, probably due to inferior charge extraction, as shown in the CELIV results. The same strategies are slightly more effective with the CsFA composition, possibly due to the absence of Br in the 3D bulk. Voltage gains of 35 to 48 mV are achieved by various surface modification treatments, displayed in Fig. 5.1b. CsFA PSCs treated with either MAI or FAI, acting as additives in the solution, are equally improved, despite the fact that the underlying 3D perovskite does not contain the MA cation. This proves the wide application field of such surface modification methods, leaving open the possibility for experimentation on numerous perovskite stoichiometries.

Overall, this thesis constitutes additional evidence supporting the efficacy of surface modification strategies based on PEA salts, especially when combined with perovskite precursors. Real performance, measured with MPPT tests, can be slightly enhanced by introducing a thin 2D perovskite layer before the ETL deposition, limiting Shockley-Read-Hall recombination speed. The developed procedures demonstrate significant voltage

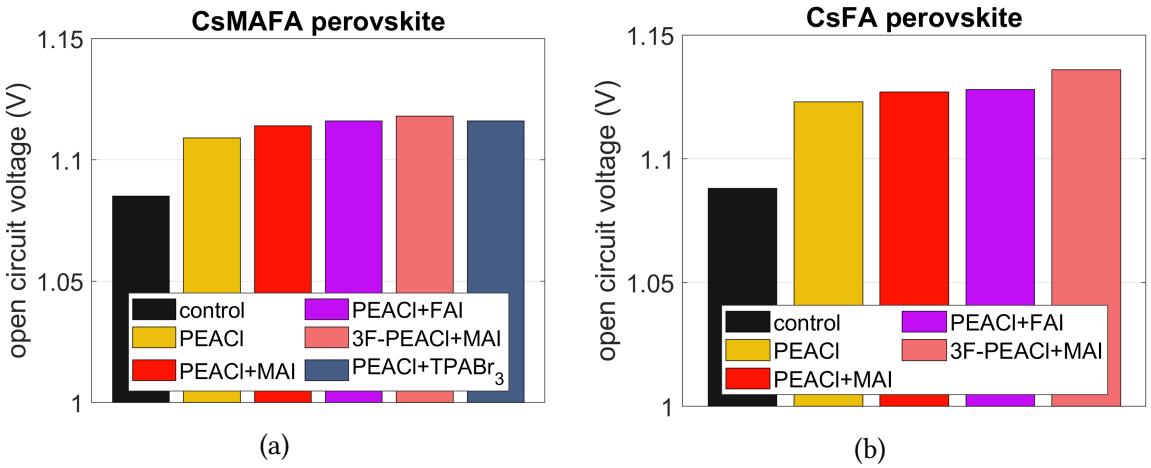

Figure 5.1.: Open circuit voltages of CsMAFA (a) and CsFA (b) devices treated with various solutions against references. All treatments present optimized values, i.e. 10 and 6.7 mM concentrations of 2D ligand for single and dual treatments; 2:1 molar ratios for solutions containing methylammonium iodide (MAI) or formamidinium iodide (FAI); 6:1 molar ratios for solutions containing trimethylphenylammonium tribromide ($TPABr_3$). Data obtained after one minute of light soaking time; a shadow mask was used for CsMAFA measurements.

gains in comparison to control devices, although this comes with small J_{SC} deficits in CsMAFA PSCs. The reduced charge extraction, supported by CELIV characterization of CsMAFA PSCs, can be attributed to the particular perovskite composition, since the same effect is not detected in CsFA devices. Ion movement enhancement or suppression, due to the presence of either MA or Br, could affect charge carrier mobility and thus the extraction efficiency [29, 95, 96]. More extensive investigation on the impacts of LDPs in charge carrier extraction is required to advance the research. Extending the application to perovskite/$CuInSe_2$ tandem solar cells, the current reduction of CsMAFA PSCs constitutes a smaller issue, since the monolithic devices are limited by the photogenerated current of the bottom $CuInSe_2$ subcell.

Looking at future developments in this field, more can be done to identify the optimal surface modification treatment, first by scanning a wider range of materials and secondly by adjusting the bulk composition of the studied PSC. Excess PbI_2 is possibly playing an important role in LDP formation, influencing the composition and thickness n of such phases. Charge extraction analysis and other techniques are extremely useful to study LDPs and the influence of their properties on PV performance. Moreover, surface engineering can be coupled with bulk additives, PEA-based or other large cation salts, to further reduce Shockley-Read-Hall recombination at the grain boundaries inside the absorber, limiting voltage losses of p-i-n PSCs. More extensive characterization of treated devices, involving a thorough investigation of 2D perovskites chemical and optoelectronic properties, is needed to further advance the research.

List of symbols

λ	Light wavelength
μ	Charge carrier mobility
ν	Light frequency
π	Pi
Φ_{abs}	Absorbed photon flux
Φ_{bb}	Black body photon flux
Φ_{em}	Emitted photon flux
Φ_{ph}	Incident photon flux
A	Solar cell active area
A_{mask}	Mask aperture area
d	Absorber thickness
E_g	Bandgap energy
E_{ph}	Photon energy
G_c	Generation rate
h	Planck constant
I	Electric current
J	Electric current density
$J_{0,rad}$	Radiative dark recombination current density
$J_{non-rad}$	Non-radiative recombination current density
J_{rad}	Radiative recombination current density
J_{SC}	Short circuit current density

k	Recombination constant
k_B	Boltzmann constant
N_{extr}	Extracted charge carrier density
n_c	Charge carrier density
n_{id}	Ideality factor
P	Radiative power
q	Electron charge
R_c	Recombination rate
R_S	Series resistance
R_{SH}	Shunt resistance
T	Absolute temperature
t	Time
t_G	Goldschmidt's tolerance factor
V	Electric voltage
V_{OC}	Open circuit voltage
$V_{OC,imp}$	Implied open circuit voltage
$V_{OC,rad}$	Radiative open circuit voltage

Bibliography

[1] *State of the Climate: Monthly Global Climate Report for Annual 2021*. NOAA National Centers for Environmental Information, Jan. 2022. URL: https://www.ncei.noaa.gov/access/monitoring/monthly-report/global/202113.

[2] NASA. *The Effects of Climate Change*. URL: https://climate.nasa.gov/effects/.

[3] NASA. *Scientific Consensus: Earth's Climate Is Warming*. URL: https://climate.nasa.gov/scientific-consensus/.

[4] Intergovernmental Panel on Climate Change. *Climate change 2021: Technical Summary*. 2021. DOI: 10.1017/9781009157896.002.

[5] International Energy Agency. *World Energy Outlook 2021*. 2021. URL: https://www.iea.org/reports/world-energy-outlook-2021.

[6] International Energy Agency. *Global Energy Review: CO2 Emissions in 2021 Global emissions rebound sharply to highest ever level*. 2021. URL: https://www.iea.org/reports/global-energy-review-co2-emissions-in-2021-2.

[7] International Energy Agency. *World Energy Outlook 2022*. 2022. URL: https://www.iea.org/reports/world-energy-outlook-2022.

[8] British Petroleum. *bp Energy Outlook 2022*. URL: https://www.bp.com/en/global/corporate/energy-economics.html.

[9] International Renewable Energy Agency, International Energy Agency, and REN21. *Renewable Energy Policies in a Time of Transition Heating and Cooling*. 2020. URL: https://www.ren21.net/heating-and-cooling-2020/.

[10] International Energy Agency. *Solar PV*. 2022. URL: https://www.iea.org/reports/solar-pv.

[11] Fraunhofer Ise and Pse Projects GmbH. *Photovoltaics Report*. URL: www.ise.fraunhofer.de.

[12] Martin A. Green et al. "Solar cell efficiency tables (Version 60)". In: *Progress in Photovoltaics: Research and Applications* (June 2022). ISSN: 1062-7995. DOI: 10.1002/pip.3595. URL: https://onlinelibrary.wiley.com/doi/10.1002/pip.3595.

[13] Lucio C. Andreani et al. "Silicon solar cells: Toward the efficiency limits". In: *Advances in Physics: X* 4 (1 Jan. 2019). ISSN: 23746149. DOI: 10.1080/23746149.2018.1548305.

[14] National Renewable Energy Laboratory. *Best Research-Cell Efficiency Chart*. URL: https://www.nrel.gov/pv/cell-efficiency.html.

[15] Jinsong Huang et al. "Understanding the physical properties of hybrid perovskites for photovoltaic applications". In: *Nature Reviews Materials* 2 (July 2017). ISSN: 20588437. DOI: 10.1038/natrevmats.2017.42.

[16] Rui Wang et al. "A Review of Perovskites Solar Cell Stability". In: *Advanced Functional Materials* 29 (47 Nov. 2019). ISSN: 16163028. DOI: 10.1002/adfm.201808843.

[17] Daiyu Li et al. "A Review on Scaling Up Perovskite Solar Cells". In: *Advanced Functional Materials* 31 (12 Mar. 2021). ISSN: 16163028. DOI: 10.1002/adfm.202008621.

[18] Alessandro Martulli et al. "Towards market commercialization: Lifecycle economic and environmental evaluation of scalable perovskite solar cells". In: *Progress in Photovoltaics: Research and Applications* (Sept. 2022). ISSN: 1062-7995. DOI: 10.1002/pip.3623. URL: https://onlinelibrary.wiley.com/doi/10.1002/pip.3623.

[19] Hui Li and Wei Zhang. "Perovskite Tandem Solar Cells: From Fundamentals to Commercial Deployment". In: *Chemical Reviews* 120 (18 Sept. 2020), pp. 9835–9950. ISSN: 15206890. DOI: 10.1021/acs.chemrev.9b00780.

[20] Martin Stolterfoht et al. "Visualization and suppression of interfacial recombination for high-efficiency large-area pin perovskite solar cells". In: *Nature Energy* 3 (10 Oct. 2018), pp. 847–854. ISSN: 20587546. DOI: 10.1038/s41560-018-0219-8.

[21] Eline M. Hutter et al. "Charge Transfer from Methylammonium Lead Iodide Perovskite to Organic Transport Materials: Efficiencies, Transfer Rates, and Interfacial Recombination". In: *Advanced Energy Materials* 7 (13 July 2017). ISSN: 16146840. DOI: 10.1002/aenm.201602349.

[22] Amran Al-Ashouri et al. "Conformal monolayer contacts with lossless interfaces for perovskite single junction and monolithic tandem solar cells". In: *Energy and Environmental Science* 12 (11 Nov. 2019), pp. 3356–3369. ISSN: 17545706. DOI: 10.1039/c9ee02268f.

[23] Rui Wang et al. "Constructive molecular configurations for surface-defect passivation of perovskite photovoltaics". In: *Science* (2019), p. 2022. URL: https://www.science.org.

[24] Saba Gharibzadeh et al. "Two birds with one stone: Dual grain-boundary and interface passivation enables >22% efficient inverted methylammonium-free perovskite solar cells". In: *Energy and Environmental Science* 14 (11 Nov. 2021), pp. 5875–5893. ISSN: 17545706. DOI: 10.1039/d1ee01508g.

[25] Hao Chen et al. "Quantum-size-tuned heterostructures enable efficient and stable inverted perovskite solar cells". In: *Nature Photonics* 16 (5 May 2022), pp. 352–358. ISSN: 17494893. DOI: 10.1038/s41566-022-00985-1.

[26] Long Zhou et al. "Highly Efficient and Stable Planar Perovskite Solar Cells with Modulated Diffusion Passivation Toward High Power Conversion Efficiency and Ultrahigh Fill Factor". In: *Solar RRL* 3 (11 Nov. 2019). ISSN: 2367198X. DOI: 10.1002/solr.201900293.

[27] Hong Zhang et al. "Multimodal host–guest complexation for efficient and stable perovskite photovoltaics". In: *Nature Communications* 12 (1 Dec. 2021). ISSN: 20411723. DOI: 10.1038/s41467-021-23566-2.

[28] Tzu Sen Su et al. “Crown Ether Modulation Enables over 23% Efficient Formamidinium-Based Perovskite Solar Cells”. In: *Journal of the American Chemical Society* 142 (47 Nov. 2020), pp. 19980–19991. ISSN: 15205126. DOI: 10.1021/jacs.0c08592.

[29] Jiangzhao Chen and Nam Gyu Park. “Materials and Methods for Interface Engineering toward Stable and Efficient Perovskite Solar Cells”. In: *ACS Energy Letters* 5 (8 Aug. 2020), pp. 2742–2786. ISSN: 23808195. DOI: 10.1021/acsenergylett.0c01240.

[30] Matthew T. Boyd et al. “Evaluation and validation of equivalent circuit photovoltaic solar cell performance models”. In: *Journal of Solar Energy Engineering, Transactions of the ASME* 133 (2 2011). ISSN: 01996231. DOI: 10.1115/1.4003584.

[31] Wolfgang Tress et al. “Interpretation and evolution of open-circuit voltage, recombination, ideality factor and subgap defect states during reversible light-soaking and irreversible degradation of perovskite solar cells”. In: *Energy and Environmental Science* 11 (1 Jan. 2018), pp. 151–165. ISSN: 17545706. DOI: 10.1039/c7ee02415k.

[32] William Shockley and Hans J. Queisser. “Detailed balance limit of efficiency of p-n junction solar cells”. In: *Journal of Applied Physics* 32 (3 1961), pp. 510–519. ISSN: 00218979. DOI: 10.1063/1.1736034.

[33] Alexis De Vos. “Detailed balance limit of the efficiency of tandem solar cells”. In: *Journal of Physics D: Applied Physics To* 13 (1980), p. 839.

[34] Chuang Marcus. *Shockley Queisser limit: calculation and visualization tools for theoretical solar cell efficiencies based on the Shockley Queisser limit with options to change temperature, light intensity, and radiative efficiency.* URL: https://github.com/marcus-cmc/Shockley-Queisser-limit.

[35] National Renewable Energy Laboratory. *Reference Air Mass 1.5 Spectra.* URL: https://www.nrel.gov/grid/solar-resource/spectra-am1.5.html.

[36] Uwe Rau. “Reciprocity relation between photovoltaic quantum efficiency and electroluminescent emission of solar cells”. In: *Physical Review B - Condensed Matter and Materials Physics* 76 (8 Aug. 2007). ISSN: 10980121. DOI: 10.1103/PhysRevB.76.085303.

[37] Wolfgang Tress et al. “Predicting the open-circuit voltage of CH3NH3PbI3 perovskite solar cells using electroluminescence and photovoltaic quantum efficiency spectra: The role of radiative and non-radiative recombination”. In: *Advanced Energy Materials* 5 (3 Feb. 2015). ISSN: 16146840. DOI: 10.1002/aenm.201400812.

[38] Kristofer Tvingstedt et al. “Radiative efficiency of lead iodide based perovskite solar cells”. In: *Scientific Reports* 4 (Aug. 2014). ISSN: 20452322. DOI: 10.1038/srep06071.

[39] Martin Stolterfoht et al. “The impact of energy alignment and interfacial recombination on the internal and external open-circuit voltage of perovskite solar cells”. In: *Energy and Environmental Science* 12 (9 Sept. 2019), pp. 2778–2788. ISSN: 17545706. DOI: 10.1039/c9ee02020a.

[40] Akihiro Kojima et al. “Organometal halide perovskites as visible-light sensitizers for photovoltaic cells”. In: *Journal of the American Chemical Society* 131 (17 May 2009), pp. 6050–6051. ISSN: 00027863. DOI: 10.1021/ja809598r.

[41] Niraj N. Lal et al. "Perovskite Tandem Solar Cells". In: *Advanced Energy Materials* 7 (18 Sept. 2017). ISSN: 16146840. DOI: 10.1002/aenm.201602761.

[42] Anita W. Y. Ho-Baillie et al. "Recent progress and future prospects of perovskite tandem solar cells". In: *Applied Physics Reviews* 8 (4 Dec. 2021). ISSN: 19319401. DOI: 10.1063/5.0061483.

[43] Giulia Grancini and Mohammad K. Nazeeruddin. "Dimensional tailoring of hybrid perovskites for photovoltaics". In: *Nature Reviews Materials* 4 (1 Jan. 2019), pp. 4–22. ISSN: 20588437. DOI: 10.1038/s41578-018-0065-0.

[44] Victor M. Goldschmidt. "Die Gesetze der Krystallochemie". In: (1926). DOI: 10.1007/BF01507527.

[45] Ab L. Wani, Anjum Ara, and Jawed Ahmad Usmani. "Lead toxicity: A review". In: *Interdisciplinary Toxicology* 8 (2 June 2015), pp. 55–64. ISSN: 13379569. DOI: 10.1515/intox-2015-0009.

[46] Michael Saliba et al. "Cesium-containing triple cation perovskite solar cells: Improved stability, reproducibility and high efficiency". In: *Energy and Environmental Science* 9 (6 June 2016), pp. 1989–1997. ISSN: 17545706. DOI: 10.1039/c5ee03874j.

[47] Jixian Xu et al. "Triple-halide wide-band gap perovskites with suppressed phase segregation for efficient tandems". In: *Science* 367 (2020), pp. 1097–1104. URL: https://www.science.org.

[48] Hyosung Choi et al. "Cesium-doped methylammonium lead iodide perovskite light absorber for hybrid solar cells". In: *Nano Energy* 7 (2014), pp. 80–85. ISSN: 22112855. DOI: 10.1016/j.nanoen.2014.04.017.

[49] Tomas Leijtens et al. "Tin-lead halide perovskites with improved thermal and air stability for efficient all-perovskite tandem solar cells". In: *Sustainable Energy and Fuels* 2 (11 2018), pp. 2450–2459. ISSN: 23984902. DOI: 10.1039/c8se00314a.

[50] Qi Jiang et al. "Surface passivation of perovskite film for efficient solar cells". In: *Nature Photonics* 13 (7 July 2019), pp. 460–466. ISSN: 17494893. DOI: 10.1038/s41566-019-0398-2.

[51] Saba Gharibzadeh et al. "2D/3D Heterostructure for Semitransparent Perovskite Solar Cells with Engineered Bandgap Enables Efficiencies Exceeding 25% in Four-Terminal Tandems with Silicon and CIGS". In: *Advanced Functional Materials* 30 (19 May 2020). ISSN: 16163028. DOI: 10.1002/adfm.201909919.

[52] Eui Hyuk Jung et al. "Efficient, stable and scalable perovskite solar cells using poly(3-hexylthiophene)". In: *Nature* 567 (7749 Mar. 2019), pp. 511–515. ISSN: 14764687. DOI: 10.1038/s41586-019-1036-3.

[53] Jiang Liu et al. "Efficient and stable perovskite-silicon tandem solar cells through contact displacement by MgF_x". In: (2022). URL: https://www.science.org.

[54] Guang Yang et al. "Defect engineering in wide-bandgap perovskites for efficient perovskite–silicon tandem solar cells". In: *Nature Photonics* 16 (8 Aug. 2022), pp. 588–594. ISSN: 1749-4885. DOI: 10.1038/s41566-022-01033-8. URL: https://www.nature.com/articles/s41566-022-01033-8.

[55] Zhaosheng Hu et al. “A Review on Energy Band-Gap Engineering for Perovskite Photovoltaics”. In: *Solar RRL* 3 (12 Dec. 2019). ISSN: 2367198X. DOI: 10.1002/solr.201900304.

[56] A. Poglitsch and D. Weber. “Dynamic disorder in methylammoniumtrihalogenoplumbates (II) observed by millimeter-wave spectroscopy”. In: *The Journal of Chemical Physics* 87 (11 1987), pp. 6373–6378. ISSN: 00219606. DOI: 10.1063/1.453467.

[57] Andreas Binek et al. “Stabilization of the trigonal high-temperature phase of formamidinium lead iodide”. In: *Journal of Physical Chemistry Letters* 6 (7 Apr. 2015), pp. 1249–1253. ISSN: 19487185. DOI: 10.1021/acs.jpclett.5b00380.

[58] Wan Jian Yin et al. “Halide perovskite materials for solar cells: A theoretical review”. In: *Journal of Materials Chemistry A* 3 (17 May 2015), pp. 8926–8942. ISSN: 20507496. DOI: 10.1039/c4ta05033a.

[59] Nam G. Park. “Perovskite solar cells: An emerging photovoltaic technology”. In: *Materials Today* 18 (2 Mar. 2015), pp. 65–72. ISSN: 18734103. DOI: 10.1016/j.mattod.2014.07.007.

[60] Xuesong Lin et al. “Efficiency progress of inverted perovskite solar cells”. In: *Energy and Environmental Science* 13 (11 Nov. 2020), pp. 3823–3847. ISSN: 17545706. DOI: 10.1039/d0ee02017f.

[61] *ITRPV 2022*. Verband Deutscher Maschinen- und Anlagenbau, 2022.

[62] Samuel D. Stranks et al. “Electron-Hole Diffusion Lengths Exceeding 1 Micrometer in an Organometal Trihalide Perovskite Absorber”. In: *www.sciencemag.org SCIENCE* 342 (2013). URL: https://www.science.org.

[63] Dong H. Kang and Nam G. Park. “On the Current–Voltage Hysteresis in Perovskite Solar Cells: Dependence on Perovskite Composition and Methods to Remove Hysteresis”. In: *Advanced Materials* 31 (34 Aug. 2019). ISSN: 15214095. DOI: 10.1002/adma.201805214.

[64] Dane W. Dequilettes et al. “Charge-Carrier Recombination in Halide Perovskites”. In: *Chemical Reviews* 119 (20 Oct. 2019), pp. 11007–11019. ISSN: 15206890. DOI: 10.1021/acs.chemrev.9b00169.

[65] Yiliang Wu et al. “On the Origin of Hysteresis in Perovskite Solar Cells”. In: *Advanced Functional Materials* 26 (37 Oct. 2016), pp. 6807–6813. ISSN: 16163028. DOI: 10.1002/adfm.201602231.

[66] S. N. Ruddlesden and P. Popper. “New compounds of the K_2NiF_4 type”. In: *538 SHORT COMMUNICATIONS Acta Cryst* 10 (1957), p. 538. DOI: 10.1107/S0365110X57001929.

[67] Constantinos C. Stoumpos et al. “Ruddlesden-Popper Hybrid Lead Iodide Perovskite 2D Homologous Semiconductors”. In: *Chemistry of Materials* 28 (8 May 2016), pp. 2852–2867. ISSN: 15205002. DOI: 10.1021/acs.chemmater.6b00847.

[68] Hsinhan Tsai et al. “High-efficiency two-dimensional ruddlesden-popper perovskite solar cells”. In: *Nature* 536 (7616 July 2016), pp. 312–317. ISSN: 14764687. DOI: 10.1038/nature18306.

[69] Alexander Z. Chen et al. "Origin of vertical orientation in two-dimensional metal halide perovskites and its effect on photovoltaic performance". In: *Nature Communications* 9 (1 Dec. 2018). ISSN: 20411723. DOI: 10.1038/s41467-018-03757-0.

[70] Ian C. Smith et al. "A Layered Hybrid Perovskite Solar-Cell Absorber with Enhanced Moisture Stability". In: *Angewandte Chemie - International Edition* 53 (42 Oct. 2014), pp. 11232–11235. ISSN: 15213773. DOI: 10.1002/anie.201406466.

[71] Giulia Grancini et al. "One-Year stable perovskite solar cells by 2D/3D interface engineering". In: *Nature Communications* 8 (June 2017). ISSN: 20411723. DOI: 10.1038/ncomms15684.

[72] Jason J. Yoo et al. "An interface stabilized perovskite solar cell with high stabilized efficiency and low voltage loss". In: *Energy and Environmental Science* 12 (7 July 2019), pp. 2192–2199. ISSN: 17545706. DOI: 10.1039/c9ee00751b.

[73] Yuhang Liu et al. *Ultrahydrophobic 3D/2D fluoroarene bilayer-based water-resistant perovskite solar cells with efficiencies exceeding 22%*. 2019. URL: https://www.science.org.

[74] Hong Zhang, Mohammad K. Nazeeruddin, and Wallace C.H. Choy. "Perovskite Photovoltaics: The Significant Role of Ligands in Film Formation, Passivation, and Stability". In: *Advanced Materials* 31 (8 Feb. 2019). ISSN: 15214095. DOI: 10.1002/adma.201805702.

[75] Amran Al-Ashouri et al. "Monolithic perovskite/silicon tandem solar cell with >29% efficiency by enhanced hole extraction". In: *Science* (Dec. 2020). URL: https://www.science.org.

[76] Xiaopeng Zheng et al. "Managing grains and interfaces via ligand anchoring enables 22.3%-efficiency inverted perovskite solar cells". In: *Nature Energy* 5 (2 Feb. 2020), pp. 131–140. ISSN: 20587546. DOI: 10.1038/s41560-019-0538-4.

[77] Mahdi Malekshahi Byranvand et al. "Chemical vapor deposited polymer layer for efficient passivation of planar perovskite solar cells". In: *Journal of Materials Chemistry A* 8 (38 Oct. 2020), pp. 20122–20132. ISSN: 20507496. DOI: 10.1039/d0ta06646j.

[78] Zhen Li et al. "Organometallic-functionalized interfaces for highly efficient inverted perovskite solar cells". In: *Science* 376.6591 (2022), pp. 416–420. DOI: 10.1126/science.abm8566. URL: https://www.science.org/doi/abs/10.1126/science.abm8566.

[79] Janardan Dagar et al. "Compositional and Interfacial Engineering Yield High-Performance and Stable p-i-n Perovskite Solar Cells and Mini-Modules". In: *ACS Applied Materials and Interfaces* 13 (11 Mar. 2021), pp. 13022–13033. ISSN: 19448252. DOI: 10.1021/acsami.0c17893.

[80] Francisco Penã-Camargo et al. "Halide Segregation versus Interfacial Recombination in Bromide-Rich Wide-Gap Perovskite Solar Cells". In: *ACS Energy Letters* 5 (8 Aug. 2020), pp. 2728–2736. ISSN: 23808195. DOI: 10.1021/acsenergylett.0c01104.

[81] Chuanliang Chen et al. “Effect of BCP buffer layer on eliminating charge accumulation for high performance of inverted perovskite solar cells”. In: *RSC Advances* 7 (57 2017), pp. 35819–35826. ISSN: 20462069. DOI: 10.1039/c7ra06365b.

[82] Yanbo Wang et al. “Reliable Measurement of Perovskite Solar Cells”. In: *Advanced Materials* 31 (47 Nov. 2019). ISSN: 15214095. DOI: 10.1002/adma.201803231.

[83] Jeffrey A. Christians, Joseph S. Manser, and Prashant V. Kamat. “Best practices in perovskite solar cell efficiency measurements. Avoiding the error of Making Bad Cells Look Good”. In: *Journal of Physical Chemistry Letters* 6 (5 Mar. 2015), pp. 852–857. ISSN: 19487185. DOI: 10.1021/acs.jpclett.5b00289.

[84] Mark V. Khenkin et al. “Consensus statement for stability assessment and reporting for perovskite photovoltaics based on ISOS procedures”. In: *Nature Energy* 5 (1 Jan. 2020), pp. 35–49. ISSN: 20587546. DOI: 10.1038/s41560-019-0529-5.

[85] Lisa Krückemeier et al. “How to Report Record Open-Circuit Voltages in Lead-Halide Perovskite Solar Cells”. In: *Advanced Energy Materials* 10 (1 Jan. 2020). ISSN: 16146840. DOI: 10.1002/aenm.201902573.

[86] John C. De Mello, H. Felix Wittmann, and Richard H. Friend. “An improved experimental determination of external photoluminescence quantum efficiency”. In: *Advanced Materials* 9 (3 1997), pp. 230–232. ISSN: 09359648. DOI: 10.1002/adma.19970090308.

[87] David Kiermasch et al. “Effects of Masking on Open-Circuit Voltage and Fill Factor in Solar Cells”. In: *Joule* 3 (1 Jan. 2019), pp. 16–26. ISSN: 25424351. DOI: 10.1016/j.joule.2018.10.016.

[88] Gytis Juška et al. “Extraction Current Transients: New Method of Study of Charge Transport in Microcrystalline Silicon”. In: (2000). DOI: 10.1103/84.4946.

[89] Martin T. Neukom et al. “Transient photocurrent response of organic bulk heterojunction solar cells”. In: *Organic Photonics IV* 7722 (Apr. 2010), p. 77220V. ISSN: 0277786X. DOI: 10.1117/12.854668.

[90] Gytis Juška et al. “Hole drift mobility in μc-Si:H”. In: *Journal of Applied Physics* 89 (9 May 2001), pp. 4971–4974. ISSN: 00218979. DOI: 10.1063/1.1359436.

[91] Martin T. Neukom, N. A. Reinke, and B. Ruhstaller. “Charge extraction with linearly increasing voltage: A numerical model for parameter extraction”. In: *Solar Energy* 85 (6 June 2011), pp. 1250–1256. ISSN: 0038092X. DOI: 10.1016/j.solener.2011.02.028.

[92] *X-ray crystallography*. URL: https://en.wikipedia.org/wiki/X-ray_crystallography.

[93] Jun Hu et al. “Synthetic control over orientational degeneracy of spacer cations enhances solar cell efficiency in two-dimensional perovskites”. In: *Nature Communications* 10 (1 Dec. 2019). ISSN: 20411723. DOI: 10.1038/s41467-019-08980-x.

[94] Marco A. Ruiz-Preciado et al. “Monolithic Two-Terminal Perovskite/CIS Tandem Solar Cells with Efficiency Approaching 25%”. In: *ACS Energy Letters* (June 2022), pp. 2273–2281. ISSN: 2380-8195. DOI: 10.1021/acsenergylett.2c00707. URL: https://pubs.acs.org/doi/10.1021/acsenergylett.2c00707.

[95] Handong Jin et al. “It’s a trap! on the nature of localised states and charge trapping in lead halide perovskites”. In: *Materials Horizons* 7 (2 Feb. 2020), pp. 397–410. ISSN: 20516355. DOI: 10.1039/c9mh00500e.

[96] Aron Walsh and Samuel D. Stranks. “Taking Control of Ion Transport in Halide Perovskite Solar Cells”. In: *ACS Energy Letters* 3 (8 Aug. 2018), pp. 1983–1990. ISSN: 23808195. DOI: 10.1021/acsenergylett.8b00764.

A. Appendix

A.1. Phenethylammonium salt concentrations

The influence of large cation salt concentration in single strategies was part of the preliminary analysis for this thesis. The experiment was conducted with PEABr diluted in IPA in three different amounts: 5, 10, and 15 mM concentrations were selected. Current-voltage curves of fabricated PSCs were evaluated to determine the most successful option, but MPPT testing was not undertaken. Statistical data, summarized in Fig. A.1, points out evident trends of descending FF and J_{SC} for greater PEABr amounts. The highest PEABr quantity was deemed excessive, due to significantly lower PCE, whereas the middle and lowest concentration groups were considered worthy of further investigation.

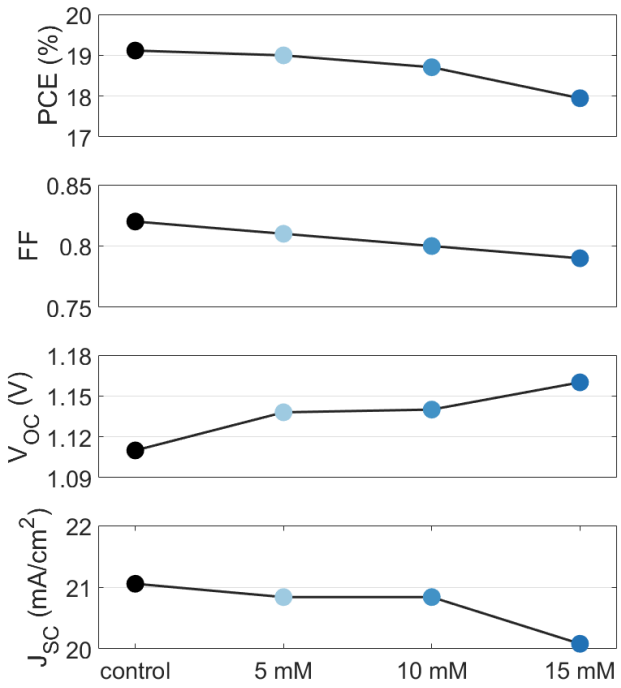

Figure A.1.: Photovoltaic parameters of PSCs treated with PEABr in concentrations of 5, 10, and 15 mM compared against the control group. The abbreviations stand for power conversion efficiency (PCE), fill factor (FF), open-circuit voltage (V_{OC}), and short-circuit current density (J_{SC})

A.2. Dual treatment concentration dependence

As mentioned in the main text, optimization of the dual treatment concentration was executed to shine more light on the impacts of PEACl quantity when coupled with MAI. The quantities chosen are the following: 70, 100, 150, and 200% of initial amounts, which added up to 6.7 and 3.3 mM for 2D ligand and MAI, respectively. Current-voltage characterization was performed following a one minute illumination time, as explained previously. The outcome, plotted in Fig. A.2, displays the expected trends, namely the V_{OC} was positively correlated with solution concentration, whereas FF and J_{SC} drop. Importantly, no further V_{OC} gain was observed between the two intermediate concentrations, discouraging the use of the 150% solution in other experiments. On the other hand, the short circuit current deficit was uniform for treatments up to 150% of normal amounts, underlining the small impact of the 2D ligand on charge extraction when combined with MAI. In a possible explanation this effect could be attributed to the higher conductivity of LDP layers produced by dual strategies, compared with LDPs present in single-treated PSCs.

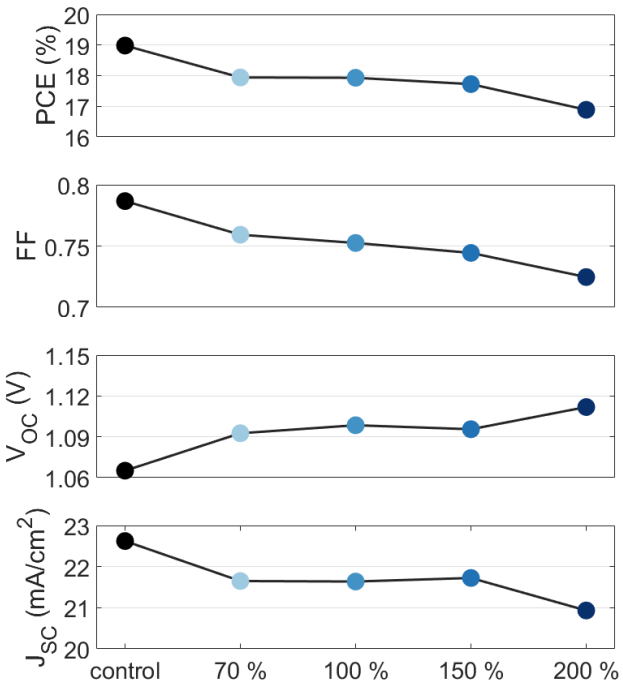

Figure A.2.: Photovoltaic parameters of PSCs treated with PEACl and methylammonium iodide (MAI) in 2:1 molar ratio and with concentrations ranging from 70% to 200% of the original value. Data obtained using a shadow mask and after one minute of light soaking time. The abbreviations stand for power conversion efficiency (PCE), fill factor (FF), open-circuit voltage (V_{OC}), and short-circuit current density (J_{SC}).

As highlighted before, light soaking undermines J-V scans credibility, eliciting MPPT measurements of champion devices. Unfortunately, this set of PSCs displayed inferior PCE stability, as proved by the time evolutions reproduced in Fig. A.3a. The cause of this result remains unknown, precluding a clear interpretation of the collected data. It could be concluded that the optimal quantity was not very dissimilar to the reference used for this experiment (100% group), although identification of the very best concentration was not possible.

As an addition, integrated J_{SC} is reported in Fig. A.3b, further supporting the claim that greater 2D ligand amounts limit more substantially charge extraction, due to the additional LDP layer. In particular, the reduced short circuit current was attributed to the larger amounts of PEACl.

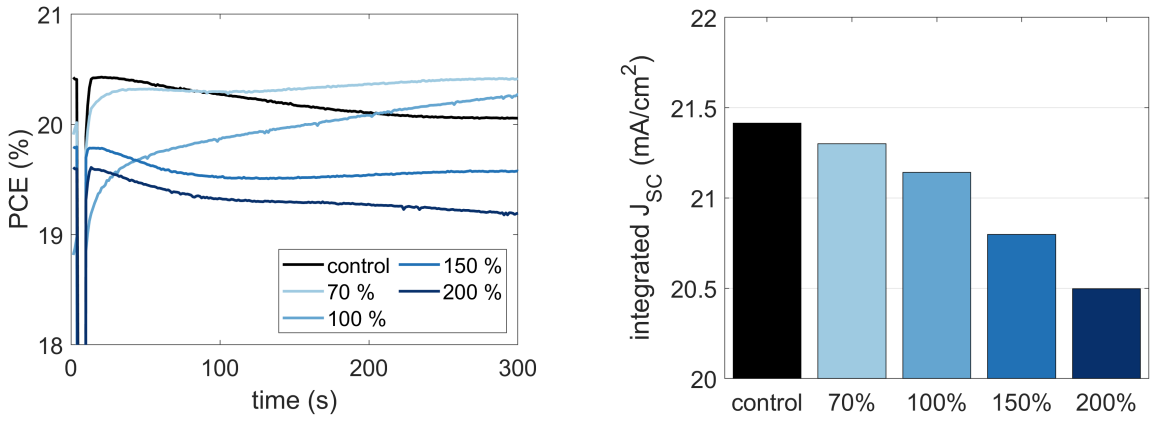

(a) (b)

Figure A.3.: (a) Maximum power point tracking test of devices treated with PEACl and methylammonium iodide (MAI) in 2:1 molar ratio and with concentrations of 70, 100, 150, and 200% of original values. Data obtained using a shadow mask. The abbreviation PCE stands for power conversion efficiency. (b) Integrated short circuit current density (J_{SC}) obtained from external quantum efficiency curves of control and treated devices.

A.3. Stability measurements

To substantiate the results exposed in Section 4.1.3, statistical data of successful long term stability tests, in terms of final PCE, are reported in Fig. A.4a. Reference samples consistently outperformed treated PSCs, with the champion device retaining an impressive 20.8% PCE at the end of the 100 h tracking time, demonstrating the excellent research starting point. Strategies based on PEACl and $TPABr_3$ turned out to be ineffective in enhancing stability under illumination, in contrast to what observed after 300 s of tracking.

As an addition, the spectral irradiance of the LED lamp of the setup used for this test, a *WAVELABS* LS-2, is represented in Fig. A.4b, compared with the standard AM1.5 spectrum.

Regarding the MPPT tests of treated CsFA PSCs, results of the champion device treated with the simple 10 mM PEACl are plotted in Fig. A.5. As explained in the main text, J-V

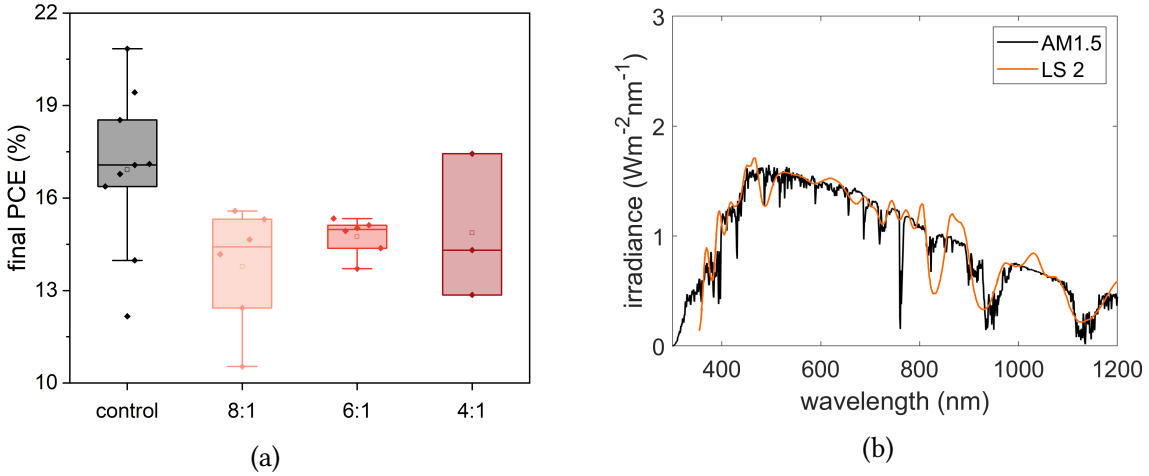

Figure A.4.: (a) Statistical data of power conversion efficiencies (PCEs) at the end of long term stability tests. Measurements for control devices and samples treated with solutions containing PEACl and $TPABr_3$ in molar ratios of 8:1, 6:1, and 4:1. (b) Spectral irradiance the *WAVELABS* LS-2 solar simulator compared to the AM1.5 reference signal.

scans after one minute of light soaking time provided very good indications on MPPT performance of treated as well as control devices. Current-voltage curves in reverse and forward scan directions indicated PCE of 21.4 and 20.2% respectively, whereas MPPT performance was very stable at 21.1%, demonstrating excellent PV performance. Overall, the single PEACl treatment displayed outstanding results, far exceeding what could be achieved with the CsMAFA perovskite.

Comparing the present outcome, measured right after device fabrication, to the PCE time evolution in Fig. 4.14, the efficiency degradation is evident, indicating sub-optimal shelf stability in nitrogen atmosphere.

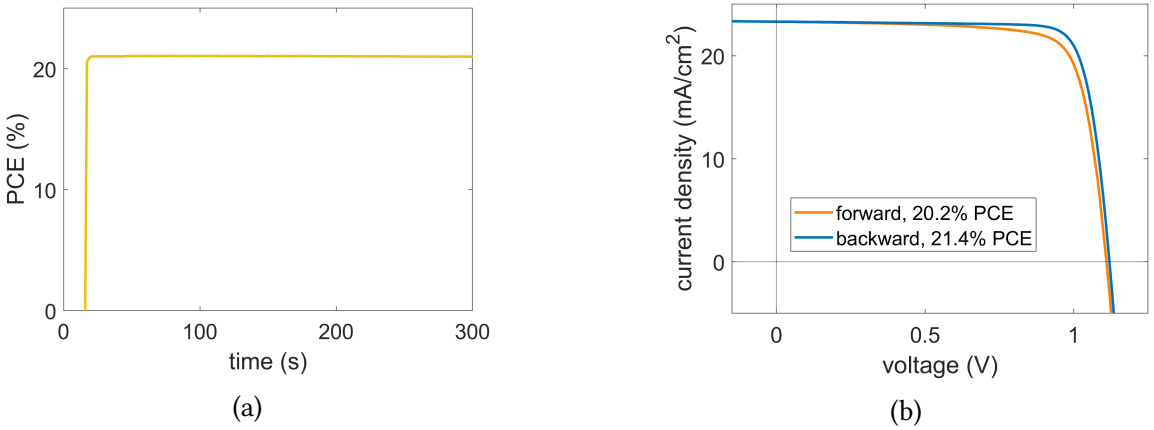

Figure A.5.: (a) Maximum power point tracking test of the CsFA champion device treated with PEACl. (b) Respective current-voltage scans with indication of power conversion efficiencies (PCEs).

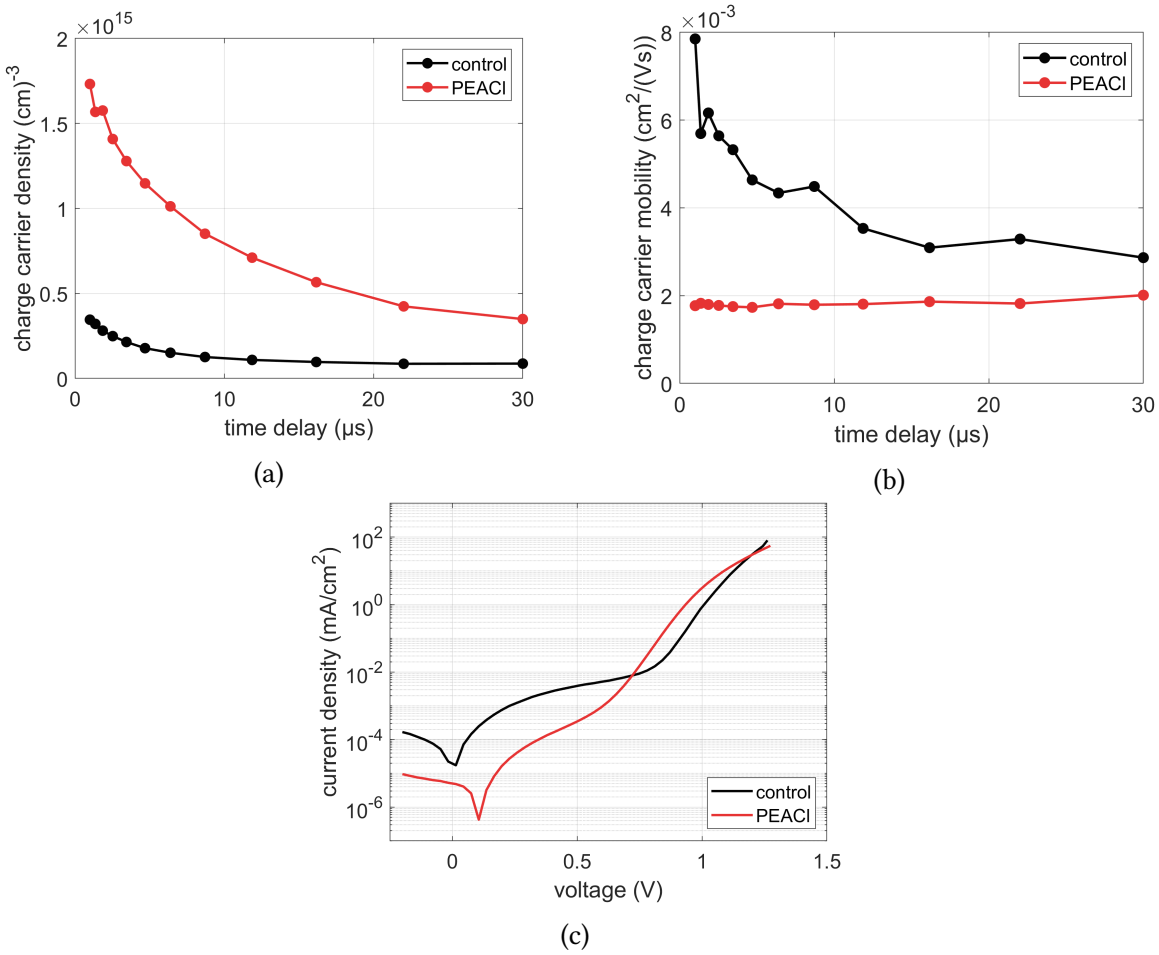

Figure A.6.: Results extracted from photo- charge extraction with linearly increasing voltage (CELIV) for CsMAFA devices treated with a 10 mM PEACl solution against control. (a) Extracted charge carrier density as a function of time delay. (b) Majority charge carrier mobility as a function of time delay. (c) Dark current-voltage curve.

A.4. Charge carrier extraction

Charge extraction with linearly increasing voltage (CELIV) measurements have been conducted for the 10 mM PEACl strategy to highlight the differences introduced by the addition of MAI in dual treatments of CsMAFA PSCs. The obtained results, graphed in Fig. A.6, prove the largely similar impacts of the two approaches, indicating that most effects could be attributed to the presence of the PEA salt. The extracted charge carrier trend was found to closely resemble what obtained with dual methods, though the values are higher in the present case, indicating less pronounced SRH recombination due to the greater amount of PEACl (10 vs 6.7 mM). Carrier mobility, instead, was the lowest recorded amongst all tested PSCs, demonstrating the beneficial presence of MAI in promoting LDP layers with larger perovskite thickness n, enhancing electric conductivity. This explanation is in line with what discussed by Chen et al. [25], which attributed the enhanced charge

extraction efficiency to $n \geq 3$ LDPs. Moreover, the saturation current curve indicated, as previously noted for similar treatments, increased V_{OC} caused by reduced defect density.

List of Figures

2.1. Circuit model of a solar cell and current-voltage curve 5
2.2. Shockley-Queisser limit efficiency and spectral uses 8
2.3. Schematics of the cubic perovskite structure 11
2.4. Schematics of 2D and 3D perovskites 13

3.1. Cell stack and energy band diagram 16
3.2. Cell fabrication process steps 19
3.3. Spectral irradiance of the solar simulators and current-voltage scan displaying hysteretic behavior 21
3.4. External quantum efficiency spectrum and black body spectral photon flux. 24
3.5. Photo- and dark-CELIV schematics for applied voltage, illumination, and extracted current 25
3.6. Photo-CELIV current profiles and extracted results 26
3.7. Current-voltage curve in dark conditions 27
3.8. X-ray diffraction analysis 28

4.1. Photovoltaic parameters of CsFA PSCs treated with a 10 mM PEACl solution against control 30
4.2. Photovoltaic parameters of CsMAFA PSCs treated with different phenethylammonium salt concentrations 31
4.3. Integrated short circuit current density for simple PEA salt treatments . 32
4.4. Photovoltaic parameters of CsMAFA PSCs treated with PEACl solutions modifying spin coating method and annealing time 33
4.5. Photovoltaic parameters of CsMAFA PSCs treated with PEACl and MAI in a 2:1 molar ratio comparing different DMF contents 34
4.6. Photovoltaic parameters of CsMAFA PSCs treated with PEACl and MAI in molar ratios of 4:1, 2:1, and 1:1 35
4.7. Photovoltaic parameters of CsMAFA PSCs treated with PEACl, PEAI, and PEABr in combination with MAI or FAI in 2:1 molar ratio 36
4.8. MPPT of CsMAFA PSCs treated with PEACl, PEAI, and PEABr combined with either MAI or FAI 37
4.9. Photovoltaic parameters of CsMAFA PSCs treated with fluorinated PEA salts and MAI in molar ratio of 2:1 38
4.10. MPPT of CsMAFA PSCs treated with fluorinated PEACl, PEAI, and PEABr combined with MAI 39
4.11. Photovoltaic parameters of CsMAFA PSCs treated with PEACl and $TPABr_3$ in multiple molar ratios 40

4.12. MPPT of CsMAFA PSCs treated with PEACl and $TPABr_3$ in multiple molar ratios . . . 41
4.13. Photovoltaic parameters of CsFA PSCs treated with single and dual strategies 42
4.14. MPPT of CsFA PSCs treated with single and dual strategies . . . 43
4.15. Photovoltaic parameters of CsFA PSCs treated with dual strategies based on fluorinated PEA salts . . . 44
4.16. MPPT of CsFA PSCs treated with dual strategies based on fluorinated compounds . . . 45
4.17. Statistics of implied open circuit voltage for dual strategies . . . 46
4.18. Implied open circuit voltages for single and dual treatment strategies based on PEACl . . . 47
4.19. CELIV extracted results for CsMAFA PSCs treated with PEACl and MAI 48
4.20. CELIV extracted results for CsMAFA PSCs treated with PEACl and $TPABr_3$ 49
4.21. X-ray diffraction pattern of reference and treated CsMAFA films . . . 50

5.1. Open circuit voltages of CsMAFA and CsFA devices treated with various solutions against references . . . 55

A.1. Median photovoltaic parameters of PSCs treated with PEABr in different concentrations . . . 69
A.2. Median photovoltaic parameters of PSCs treated with PEACl and MAI in 2:1 molar ratio and with different concentrations . . . 70
A.3. MPPT and EQE tests of devices treated with PEACl and MAI in 2:1 molar ratio and with different concentrations . . . 71
A.4. Statistical data and lamp spectrum of long term stability measurements. . 72
A.5. MPPT and current-voltage measurements of CsFA PSCs treated with PEACl. 72
A.6. CELIV extracted results for CsMAFA devices treated with PEACl . . . 73